Title
Novel 3D Imaging Algorithms and Applications

Author
Pryor, Alan Persons

Publication Date
2018

Peer reviewed|Thesis/dissertation

UNIVERSITY OF CALIFORNIA
Los Angeles

Novel 3D Imaging Algorithms and Applications

A dissertation submitted in partial satisfaction
of the requirements for the degree
Doctor of Philosophy in Physics

by

Alan Persons Pryor, Jr

2018

ABSTRACT OF THE DISSERTATION

Novel 3D Imaging Algorithms and Applications

by

Alan Persons Pryor, Jr
Doctor of Philosophy in Physics
University of California, Los Angeles, 2018
Professor Jianwei Miao, Chair

Three-dimensional image reconstruction is a scientific undertaking of fundamental importance spanning numerous fields including molecular biology, physical chemistry, materials science, physics, and medicine across length scales ranging from the astronomical to the atomic. Despite the broad-reaching nature of this topic, the underlying mechanics and core mathematics are shared, with the ultimate objective being achieving an interpretable representation of some 3D structure from a series of 2D measurements, and, at the time of this writing, at least three Nobel prizes have been awarded for quantitative 3D imaging applications. Although enormous strides have been made over the past several decades in instrumentation, sample preparation, and experimental methodology, comparatively few improvements have been made to tomgraphic reconstruction algorithms. With the ever-increasing availability of high-performance computing resources, a more compelling argument than ever before can be made for the value of developing novel algorithms and the pursuit of accessible scientific software.

In this work, a set of such developments are reported along with several applications. A new tomographic reconstruction algorithm, termed Generalized Fourier Iterative Reconstruction (GENFIRE), is described in detail. By combining powerful, general constraints in both real and reciprocal space, GENFIRE is shown to produce superior reconstructions compared to existing techniques and provides

additional benefits including freedom from single-tilt axis restrictions, denoising through a novel Fourier technique termed resolution extension/suppression, and cross-validation through an adapted version of crystallographic R_{free}. In subsequent chapters, GENFIRE is applied in a diverse range of experiments including X-ray ptychographic imaging of cells, cryo-electron tomography of bacteria, correlative X-ray fluorescence imaging of algae, and scanning transmission electron microscopy (STEM) of bimetallic nanoparticles at atomic resolution. GENFIRE is fully open-source with a graphical user interface and is freely-available online.

In the appendices, two additional parallel algorithms are described. The first is an optimized graphics processing unit (GPU) implementation of traditional multislice simulation for simulation of STEM image formation as well as the new Plane Wave Reciprocal-space Interpolated Scattering Matrix (PRISM) algorithm that is capable of reducing computation times of routine calculations from several weeks to a few minutes, and the second is a parallel framework for large-scale 3D phase retrieval of symmetric nanostructures from single diffraction patterns.

The dissertation of Alan Persons Pryor, Jr is approved.

Alexander Levine

David Eisenberg

Dolores Bozovic

Jianwei Miao, Committee Chair

University of California, Los Angeles

2018

This work is dedicated to my loving wife, Anna-Grace,

my daughter, Madelyn,

and to my other children whom I have not yet had the pleasure of meeting.

I love you all so very much.

Table of Contents

List of Figures

List of Tables

Acknowledgments

I would like to express my extreme gratitude towards my advisor, Professor Jianwei (John) Miao, for his mentorship, support, and guidance over the five years of my graduate work, without which this work would not have been possible. I am also grateful to remainder of my committee for their consideration of this dissertation.

Chapter 2 is an adapted and partially modified version, including figures, of the article "*GENFIRE*: A generalized Fourier iterative reconstruction algorithm for high-resolution 3D imaging". I thank and acknowledge the coauthors for their contributions: Y. Yang, A. Rana, M. Gallagher-Jones, J. Zhou, Y. H. Lo, G. Melinte, W. Chiu, J. A. Rodriguez, and J. Miao.

Chapter 3 is an adapted and partially modified version, including figures, of the article "Correlative cellular ptychography with functionalized nanoparticles at the Fe L-edge". I thank and acknowledge the coauthors for their contributions: M. Gallagher-Jones, C. S. Baraldi Dias, K. Bouchmella, L. Zhao, Y. H. Lo, M. Borba Cardoso, D. Shapiro, J. A. Rodriguez and J. Miao.

Chapter 4 is an adapted and partially modified version, including figures, of the article "Correlative 3D X-ray fluorescence and ptychographic tomography of un-labeled frozen hydrated green alga". I thank and acknowledge the coauthors for their contributions: J. Deng, Y. H. Lo, M. Gallagher-Jones, S. Chen, Q. Jin, Y. Hong, S. Vogt, J. Miao, and C. Jacobsen.

Chapter 5 is an adapted and partially modified version, including figures, of the article "Deciphering chemical order/disorder and material properties at the single-atom level". I thank and acknowledge the coauthors for their contributions: Y. Yang, C. C. Chen, M. C. Scott, C. Ophus, R. Xu, L. Wu, F. Sun, W. Theis, J. Zhou, M. Eisenbach, P. R. C. Kent, R. Sabirianov, H. Zeng, P. Ercius, and J.

Miao.

Appendix A is an adapted and partially modified version, including figures, of the article "A streaming multi-GPU implementation of image simulation algorithms for scanning transmission electron microscopy". I thank and acknowledge the coauthors for their contributions: C. Ophus and J. Miao.

Appendix B is an adapted and partially modified version, including figures, of the article "Single-Shot 3D Diffractive Imaging of Core-Shell Nanoparticles with Elemental Specificity". I thank and acknowledge the coauthors for their contributions: A. Rana, R. Xu, J. A. Rodriguez, Y. Yang, M. Gallagher-Jones, H. Jiang, J. Park, S. Kim, S. Kim, D. Nam, Y. Yue, J. Fan, Z. Sun, B. Zhang, D. F. Gardner, C. S. Baraldi Dias, Y. Joti, T. Hatsui, T. Kameshima, Y. Inubushi, K. Tono, J. Y. Lee, M. Yabashi, C. Song, T. Ishikawa, H. Kapteyn, M. Murnane, and J. Miao.

I acknowledge support by STROBE: A National Science Foundation Science & Technology Center under Grant No. DMR 1548924 and the Office of Basic Energy Sciences of the US DOE (DE-SC0010378).

This dissertation work was partially supported by the Holmes-Peccei Fellowship.

Vita

2013	H. Fukuyo Memorial Scholarship Award for Excellence in Physics
2013	B.S. Physics with Highest Honors. *Georgia Institute of Technology* Atlanta, Georgia
2013-2017	Graduate Teaching Assistant Department of Physics and Astronomy *University of California, Los Angeles* Los Angeles, California
2014-2018	Graduate Student Researcher Coherent Imaging Group Department of Physics and Astronomy *University of California, Los Angeles* Los Angeles, California
2015	M.S. Physics. *University of California, Los Angeles* Los Angeles, California
2017	Microscopy Society of America Student Scholar
2018	Holmes-Peccei Dissertation-Year Fellow

Publications

J. A. Rodriguez, R. Xu, C. C. Chen, Z. Huang, H. Jiang, A. L. Chen, K. S. Raines, **A. Pryor Jr.**, D. Nam, L. Wiegart, C. Song, A. Madsen, Y. Chushkin, F. Zontone, P. J. Bradley, and J. Miaob. Three-dimensional coherent X-ray diffractive imaging of whole frozen-hydrated cells. *IUCrJ* **2**, 575583 (2015)

Y. Yang*, C. C. Chen*, M. C. Scott*, C. Ophus*, R. Xu, **A. Pryor Jr.**, L. Wu, F. Sun, W. Theis, J. Zhou, M. Eisenbach, P. R. C. Kent, R. F. Sabirianov, H. Zeng, P. Ercius and J. Miao. Deciphering chemical order/disorder and material properties at the single-atom level. *Nature* **542**, 7579 (2017)

M. Gallagher-Jones*, C. S. B. Dias*, **A. Pryor Jr.***, K. Bouchmella, L. Zhao, Y. H. Lo, M. B. Cardoso, D. Shapiro, J. A. Rodriguez and J. Miao. Correlative cellular ptychography with functionalized nanoparticles at the Fe L-edge. *Scientific Reports* **7**, (2017)

A. Pryor Jr.*, Y. Yang*, A. Rana, M. Gallagher-Jones, J. Zhou, Y. H. Lo, G. Melinte, W. Chiu, J. A. Rodriguez and J. Miao. GENFIRE: A generalized Fourier iterative reconstruction algorithm for high-resolution 3D imaging. *Scientific Reports* **7**, (2017)

A. Pryor Jr., C. Ophus, and J. Miao. A streaming multi-GPU implementation of image simulation algorithms for scanning transmission electron microscopy. *Advanced Structural and Chemical Imaging* **3**, (2017)

A. Pryor Jr. et al. Single-shot 3D coherent diffractive imaging of core-shell nanoparticles with elemental specificity. *submitted* (2017)

** denotes equal contribution*

CHAPTER 1

Introduction to Tomography

Introduction

Tomography is the process of producing a 3D image from a series of 2D projection images and to a general audience is most recognizable in the form of the computed tomography (CT) scan. In addition to diagnostic medical imaging, tomography has widespread quantitative applications including identification of atomic coordinates and defects in nanoparticles, determination of protein and virus structure, visualization of biological interactions, *in-situ* studies of materials such as batteries, and many more [1–15].

1.1 Fundamental Principles

1.1.1 Projection-Slice Theorem

Arguably the most important mathematical formulation in tomography is the Projection-slice theorem, also known as the Fourier slice theorem, which provides a direct connection between a linear 2D projection image and the original 3D object. Stated plainly, the theorem states that the Fourier transform of an object's 2D projection is equivalent to a central slice of the 3D Fourier transform of the same object at the orientation with normal vector parallel to the direction of projection. Starting from a 3D density, $\rho(x, y, z)$, one first defines the 2D linear

projection along the z-axis, $P(x, y)$, as

$$P(x, y) = \int_{-\infty}^{\infty} \rho(x, y, z) dz \tag{1.1}$$

on a parallel front, consider the 3D Fourier transform of $\rho(x, y, z)$, $F(u, v, w)$

$$F(u, v, w) = \int_{-\infty}^{\infty} \int_{-\infty}^{\infty} \int_{-\infty}^{\infty} \rho(x, y, z) e^{-2\pi i(ux+vy+wz)} dx dy dz \tag{1.2}$$

For a projection along the z-direction, the central slice of Fourier space corresponds simply to $w = 0$

$$F(u, v, 0) = \int_{-\infty}^{\infty} \int_{-\infty}^{\infty} \int_{-\infty}^{\infty} \rho(x, y, z) e^{-2\pi i(ux+vy)} dx dy dz \tag{1.3}$$

or, rearranging

$$F(u, v, 0) = \int_{-\infty}^{\infty} \int_{-\infty}^{\infty} [\int_{-\infty}^{\infty} \rho(x, y, z) dz] e^{-2\pi i(ux+vy)} dx dy \tag{1.4}$$

which upon substituting the above equation for $P(x, y)$ yields

$$F(u, v, 0) = \int_{-\infty}^{\infty} \int_{-\infty}^{\infty} P(x, y) e^{-2\pi i(ux+vy)} dx dy \tag{1.5}$$

The right hand side is the 2D Fourier transform of $P(x, y)$. *Q.E.D.*

Thus, a 2D measurement provides a partial sampling of data in the 3D Fourier space corresponding to $\rho(x, y, z)$. If similar data can be obtained for multiple orientations, for example by tilting the sample and acquiring multiple exposures, a more complete sampling of the 3D Fourier space can be obtained. Achieving complete sampling of all points in Fourier space would allow for determination of $\rho(x, y, z)$ through a simple inverse Fourier transform; however, in practice this is an impossible task for several reasons that are described in the following sections.

1.1.2 Gridding

$\rho(x, y, z)$ is sampled on a Cartesian grid, but the measured 2D Fourier slices extend radially from the origin and do not, in general, overlap with the desired grid locations. This can be visualized by rotating a straight-edge around the center of a chessboard and observing that achieving exact intersection with the center of each grid point is not possible except for a few special cases such as 0° and multiples of 90°. To convert from the polar representation to a Cartesian one, some form of convolution-based interpolation scheme or alternative mathematical formulation, such as the pseudopolar Fourier transform used by the Equally Sloped Tomography (EST), another Fourier based reconstruction algorithm that is in many ways the predecessor of GENFIRE and is described shortly, is required [16, 17]. Conceptually, gridding is achieved by convolving the continuous measurement with a suitable choice of kernel and sampling this result at the location of the desired grid points. The convolution theorem, which states that the Fourier transform of a convolution of two functions is equal to the product of their individual Fourier transforms, implies that this type of convolution gridding procedure introduces a direct product in real space of the true density $\rho(x, y, z)$ with the inverse Fourier transform of the convolution kernel. Thus, a gridding correction is demanded [18].

1.1.3 Missing Wedge

Experimentally, the accessible tilt range for tomographic acquisition is almost always limited due either to geometric constraints of the tilt stages or to thickness requirements demanded to produce linear projection images [19, 20]. The result is an unmeasured region of reciprocal space that introduces elongation artifacts to the reconstruction with maximal degradation in the plane defined by the so-called missing-wedge direction, which is the orientation vector at the center of the unmeasurable region. For example, with common tilt limits of ±70° the

missing-wedge direction corresponds to the 90° tilt. This forms the missing wedge problem [19–21].

1.1.4 Projection Alignment

An important subtlety of the projection-slice theorem in the context of tomography is that $\rho(x, y, z)$ must be consistent across all acquisitions. Rotation of the sample can be described by application of a suitable rotation matrix R the coordinates (x, y, z), resulting in new coordinates (x', y', z'). In an ideal experiment, the rotation axis would coincide with the center-of-mass of the sample; however, inanimate objects are notoriously uncooperative in this regard. The result of a separation between the target sample and the geometric rotation axis of the instrument is that the sample will translate as it rotates. This can be seen by letting $x \rightarrow x - d_{rot}$ for a rotation about an axis displaced d_{rot} from the sample. This translation by itself is not a violation of the projection-slice theorem, as one could reconstruct the sample along with the surrounding area encompassed by its "orbit", but it has the undesirable effect of increasing the necessary field-of-view, and, therefore, increasing computation times. Furthermore, instrument inaccuracy, drift, and vibration will introduce additional translational jitter to the projection images. The net effect of these inaccuracies is to introduce phase shifts in Fourier space to the measured data points, which can be seen by $(x, y, z) \rightarrow (x - d_x, y - d_y, z - d_z)$ in (Eq. 1.2). To obtain a high-quality reconstruction, the projections must be aligned to correct these translational shifts. Methods for doing so include aligning to the center-of-mass [1–3, 22], cross-correlation [19], usage of fiducial markers [23], or Bayesian methods [24, 25].

In addition to translational inaccuracies, errors may also exist in the angular orientation of the projections. Methods for correction generally involve some sort of refinement loop where a preliminary reconstruction is used to update orientation parameters for the input projections [24, 26–28].

A few comments on these methods follow. The center-of-mass method aligns the projections to a fixed point using conservation of mass and is very effective if the signal-to-noise ratio is strong and, most importantly, the sample is well isolated. If the sample is not isolated, as the stages are tilted additional density will enter the edges of the field of view and violate conservation of mass. For scanning transmission electron microscopy (STEM) imaging of nanoparticles, such as in the field of atomic electron tomography (AET) [29], this is generally not a problem as the signal-to-noise ratio is very high and the sample can be supported on a very thin substrate or suspended using a needle-tip geometry [1,30]. However, in transmission electron microscopy with cryo-preserved samples (cryo-TEM) this is almost impossible to achieve due to the presence of an ice layer.

Cross-correlation aligns each projection to the following one by making the assumption that the 2D projection of the sample density does not change much for subsequent tilts. This assumption is very sample-dependent, depends on the angular step-size between tilts, and, in general, lacks a solid mathematical basis. It is fast and is suitable for rough alignment, but should not be used for a publication-ready reconstruction.

Fiducial alignment methods require that the sample be seeded with high-contrast markers such as gold nanoparticles. These markers then serve as multiple fixed reference points, and an alignment model can then be fit after semi-automated selection [31, 32]. This type of alignment is robust as long as the data contains a single tilt axis that lies fully within the plane of the projections and the density of fiducial markers is sufficiently high.

Bayesian methods have become the *de facto* standard in the growing field of single-particle cryo-EM and some examples also exist of applications to X-ray techniques [24, 33, 34]. These methods use prior information to optimize some form of scoring function based upon posterior probability. This type of alignment is very powerful, works with very low signal-to-noise ratios, and generally pro-

duces the best final result of any of the methods listed here. The computational complexity is high, however, as multiple 3D reconstructions must be produced and each projection refined multiple times until refinement converges. Although suitable for datasets with projection sizes on the order of 500 x 500, for large fields of view this type of refinement becomes computationally infeasible with existing hardware.

1.1.5 Radiation Dose

X-rays and electron imaging techniques are extremely violent and have the potential to significantly damage or otherwise alter the sample during acquisition, and great care must be taken to limit the total radiation dose to within tolerable limits [8, 35–40]. This is of particular concern with biological samples such as cells, proteins, and viruses as these "squishy" materials are composed primarily of elements with low atomic numbers which are less robust to radiation than heavier metals [40–44]. Frustratingly, increasing the radiation dose is the most straightforward way to increase signal-to-noise ratio. The conflicting goals of achieving high resolution while also maintaining reconstruction fidelity present an enormous challenge and are the source of significant ongoing research [9, 45–49]. Developing algorithms that are capable of producing quality reconstruction from a limited number of high-quality pojections are one way to alleviate this problem, and this observation represents one of the primary original motivating factors for the development of GENFIRE.

1.2 Comments on Equally Sloped Tomography

Consideration of the problems described in previous sections provides strong motivation for an algorithm that is capable of producing quality reconstructions from a limited number of measured projections. Equally sloped tomography (EST) pre-

sented the first case of a Fourier-based iterative algorithm for achieving this [17]. By iterating between real and reciprocal space through use of the pseudopolar fast Fourier transform (PPFFT) [16] and applying positivity and support constraints in real space and replacement of measured projection data in reciprocal space, EST is capable of recovering missing data both in the missing wedge and between measurements. EST is, in many ways, the predecessor of GENFIRE and has been successfully used to produce atomic-resolution reconstructions in AET [1, 2, 22].

GENFIRE, described in detail in Chapter 2, builds upon the core concepts of EST and provides a number of additional advantages. By generalizing the orientation parameterization of the projections using Euler angles (ϕ, θ, ψ), GENFIRE is not limited to a single tilt-axis and does not require that the tilt angles be equally-sloped [17]. Although single tilt-axis datasets are common, instrumentation misalignment and vibration can result in a rotation axis that is not fully confined to the plane of the projections. This effect cannot be accounted for with an algorithm that assumes a single tilt-axis, and the correction of which can significantly improve the reconstruction [3]. Additionally, this Euler representation allows for generalized tomography of any projection acquisition method such as multi-particle methods, dual-tilt tomography, or usage of symmetry.

The iteration process for GENFIRE is based on the Fast Fourier Transform (FFT), which is computationally less complex than the PPFFT used by EST. The result is that GENFIRE is typically 3-5x faster than an equivalent EST reconstruction.

GENFIRE implements a novel way of enforcing the Fourier constraint termed resolution extension/suppression that has been shown to improve reconstruction quality in the presence of noise (Chapter 2). This works by dynamically adjusting the resolution of the replaced projection data such that low resolution data with less noise is initially enforced and high resolution data progressively introduced (extension). This process is then reversed during final iterations, forming the

suppression step, the motivation being to partially decouple the true signal, which is correlated, from the uncorrelated noise components.

A cross-validation procedure for reconstruction validation is implemented using an adapted version of R_{free} from X-ray crystallography [50]. A small percentage of the complex-valued Fourier data is withheld from reconstruction, and the reconstructed values are compared with the measured ones, providing a method of determining that the reconstruction is not overfit.

1.3 Conclusion

The subject of tomographic reconstruction is complex. Here we have described the basic mathematics and several of the experimental challenges. EST was first introduced to address these issues, and GENFIRE subsequently builds upon this to create a more robust and generalized tomographic reconstruction algorithm. In subsequent chapters, GENFIRE is described in more detail and a number of applications across multiple imaging modalities with a diversity of sample types will be explored.

CHAPTER 2

GENFIRE: A generalized Fourier iterative reconstruction algorithm for high-resolution 3D imaging

Tomography has made a radical impact on diverse fields ranging from the study of 3D atomic arrangements in matter to the study of human health in medicine. The core problem of tomography is that a mathematical method must be implement to reconstruct the 3D structure of an object from a number of 2D projections. In many scientific applications, however, the number of projections that can be measured is limited due to geometric constraints, tolerable radiation dose and/or acquisition speed. Thus it becomes an important problem to obtain the best possible reconstruction from a limited number of projections. Here, we present the mathematical implementation of a tomographic algorithm, termed GENeralized Fourier Iterative Reconstruction (GENFIRE). By iterating between real and reciprocal space, GENFIRE searches for a global solution that is consistent with both the measured data and general physical constraints. The algorithm requires minimal human intervention and also incorporates angular refinement to reduce the tilt angle error. We demonstrate that GENFIRE can produce superior results relative to several other popular tomographic reconstruction techniques by numerical simulations, and experimentally by reconstructing the 3D structure of a porous material and a frozen-hydrated marine cyanobacterium. Equipped with a graphical user interface, GENFIRE is freely available (www.genfire-em.com) and

is expected to find applications across many disciplines.

Introduction

Tomography has found widespread applications in the physical, biological and medical sciences [19, 29, 51–55]. Electron tomography, for example, is experiencing a revolution in high-resolution 3D imaging of physical and biological samples. In the physical sciences, the development of atomic electron tomography (AET) has allowed for determination of 3D atomic structure of crystal defects such as grain boundaries, anti-phase boundaries, stacking faults, dislocations, chemical order/disorder and point defects, and to precisely localize the 3D coordinates of individual atoms in materials without assuming crystallinity [1, 2, 22, 29, 56, 57]. The atomic coordinates measured by AET have been used as direct input to density functional theory calculations to correlate crystal defects and chemical order/disorder with material properties at the single atomic level [3]. In the biological sciences, single-particle cryo-electron microscopy (EM) has been applied to achieve near atomic resolution of purified protein complexes [4, 19, 55, 58, 59], and cryo-electron tomography allows for 3D imaging of pleomorphic samples such as viral infection mechanisms of cells with resolutions on the order of a few nanometers [5,6,37]. These advances are not limited to electron tomography. Tomographic implementation of synchrotron X-ray absorption and phase contrast imaging has found interdisciplinary applications [7–9, 60–63]. Using the brilliance of advanced X-ray sources, coherent diffractive imaging (CDI) methods [64] have been combined with tomographic reconstruction for 3D quantitative imaging of thick samples with resolutions in the tens of nanometers [65–71].

Presently, a popular tomographic reconstruction method is filtered back projection (FBP) [19, 51, 52]. FBP works well when there are a large number of projections with no missing data. However, when the data is inadequately sam-

pled due to the radiation dose and geometric constraints, it suffers from artifacts, potentially clouding interpretability of the final reconstruction. This difficulty can be partially alleviated by real-space iterative algorithms such as the algebraic reconstruction technique (ART) [72], simultaneous ART (SART) [73] and simultaneous iterative reconstruction technique (SIRT) [74], but these algorithms do not fully exploit the correlated information among all the projections as the iteration process is implemented using localized information in real space [73, 74]. In contrast, Fourier-based iterative algorithms use information in both real and Fourier space as part of the iterative process [3, 17, 75]. A major advantage of these algorithms is that changes made in one space affect the other space globally. equally-sloped tomography (EST) [17], an example of such an algorithm, has been successfully applied in AET to reconstruct the 3D arrangement of crystal defects in materials, including recovery of Bragg peaks in the missing wedge direction [1, 2, 22, 29]. Additionally, EST was shown to produce reconstructions comparable to modern medical CT techniques but using significantly lower radiation dose [8, 9, 37]. However, the drawback of EST is the requirement that the tilt angles must follow equally-sloped increments along a single tilt axis, which limits its broader applications

Recently, a generalized Fourier iterative reconstruction (GENFIRE) has been successfully demonstrated for high-resolution 3D imaging with a limited number of 2D projections [3]. GENFIRE first pads zeros to each 2D projection and calculates its oversampled Fourier slice [76, 77]. The oversampled Fourier slices are used to accurately compute a small fraction of points on a 3D Cartesian grid based on gridding interpolation [78, 79]. The remaining grid points that cannot be determined with sufficient accuracy are defined as unknown. The algorithm then iterates between real and reciprocal space and enforces constraints in each space. In real space, the negative valued voxels and the voxels in the zero-padding region are set to zero. In reciprocal space, the small fraction of the known grid points

are enforced in each iteration, while the unknown grid points are recovered by the iterative process. After several hundred iterations, the algorithm converges to a structure that is concurrently consistent with the measured data and the physical constraints. Furthermore, GENFIRE implements an angular refinement routine to reduce the tilt angle error and can be adapted to any tomographic data acquisition geometry. In this article, we present the mathematical implementation of the GENFIRE algorithm. Using both physical and biological samples, we demonstrate that GENFIRE produces superior 3D reconstructions relative to several other tomographic reconstruction algorithms.

2.1 Methods

2.1.1 Assembling a 3D Fourier grid with oversampling

GENFIRE first assembles a rectangular 3D Fourier grid from a set of measured 2D projections. According to the Fourier slice theorem, the Fourier transform of each 2D projection represents a plane slicing through the origin of the Fourier transform of a 3D object [51, 52]. Care should be taken that the Fourier slice theorem requires each 2D image to be a linear projection of the 3D object at a given angle. This requirement may not be satisfied in some experimental cases due to the presence of nonlinear effects, which will be discussed in later sections. To obtain a Fourier grid point, $F_{obs}(\vec{k})$, we compute its perpendicular distance to the Fourier plane, where D_j represents the perpendicular distance and (u_j, v_j) the foot of the perpendicular line to the j^{th} projection. Since (u_j, v_j) are not integer coordinates, we use the discrete Fourier transform (DFT) to compute the value of (u_j, v_j). The use of the DFT to explicitly compute the (u_j, v_j) value is more accurate than interpolating from the set of 2D FFTs of each projection at the cost of being computationally slower. A faster, but less accurate, FFT gridding method is also provided as an option in the GENFIRE package. After calculating

the (u_j, v_j) values for all the projections, we determine the value of the Fourier grid point by

$$F_{obs}(\vec{k}) = \sum_{\{j|D_j<D_{th}\}} \frac{D_j^{-1}}{\sum_{\{j|D_j<D_{th}\}} D_j^{-1}} \sum_{x=-\frac{N}{2}}^{x=\frac{N}{2}-1} \sum_{y=-\frac{N}{2}}^{y=\frac{N}{2}-1} f_{obs}^{j}(x,y) e^{\frac{-2\pi i(xu_j+yv_j)}{NO}} \tag{2.1}$$

where D_{th} is a predefined threshold, $f_{obs}^{j}(x,y)$ is the j^{th} 2D projection with a size of N x N pixels and O is the linear oversmapling ratio [70, 76]. By properly choosing D_{th} and O, we accurately determine a small fraction of the Fourier grid points, while the remaining grid points are defined as unknown. In the GENFIRE package, the default value for D_{th} and O is 0.5 and 3, respectively.

2.1.2 The Fourier based iterative algorithm

Due to radiation dose and/or geometric constraints, it is desirable in many tomography applications to achieve high-resolution 3D imaging from a limited number of projections. As a result, a significant amount of the assembled Fourier grid points remain unknown after the gridding process. To recover the unknown grid points, GENFIRE iterates between real and reciprocal space with general constraints enforced in each space (Fig. 2.1). For the 1^{st} iteration, the values of the unknown grid points are assigned to be zero, though in practice the output of the algorithm is not very sensitive to the initial choice of values for the unknowns. The j^{th} GENFIRE iteration consists of following five steps Fig. 2.1.

(i) Apply the inverse FFT to $F_i(\vec{k})$ and obtain the i^{th} image, $\rho_i(\vec{r})$.

(ii) Modify the image by applying the following constraints

$$p_i^{'}(\vec{r}) = \begin{cases} 0 & (\vec{r} \not\subset S) \cup (\rho_i(\vec{r}) < 0) \\ \rho_i(\vec{r}) & \text{otherwise} \end{cases} \tag{2.2}$$

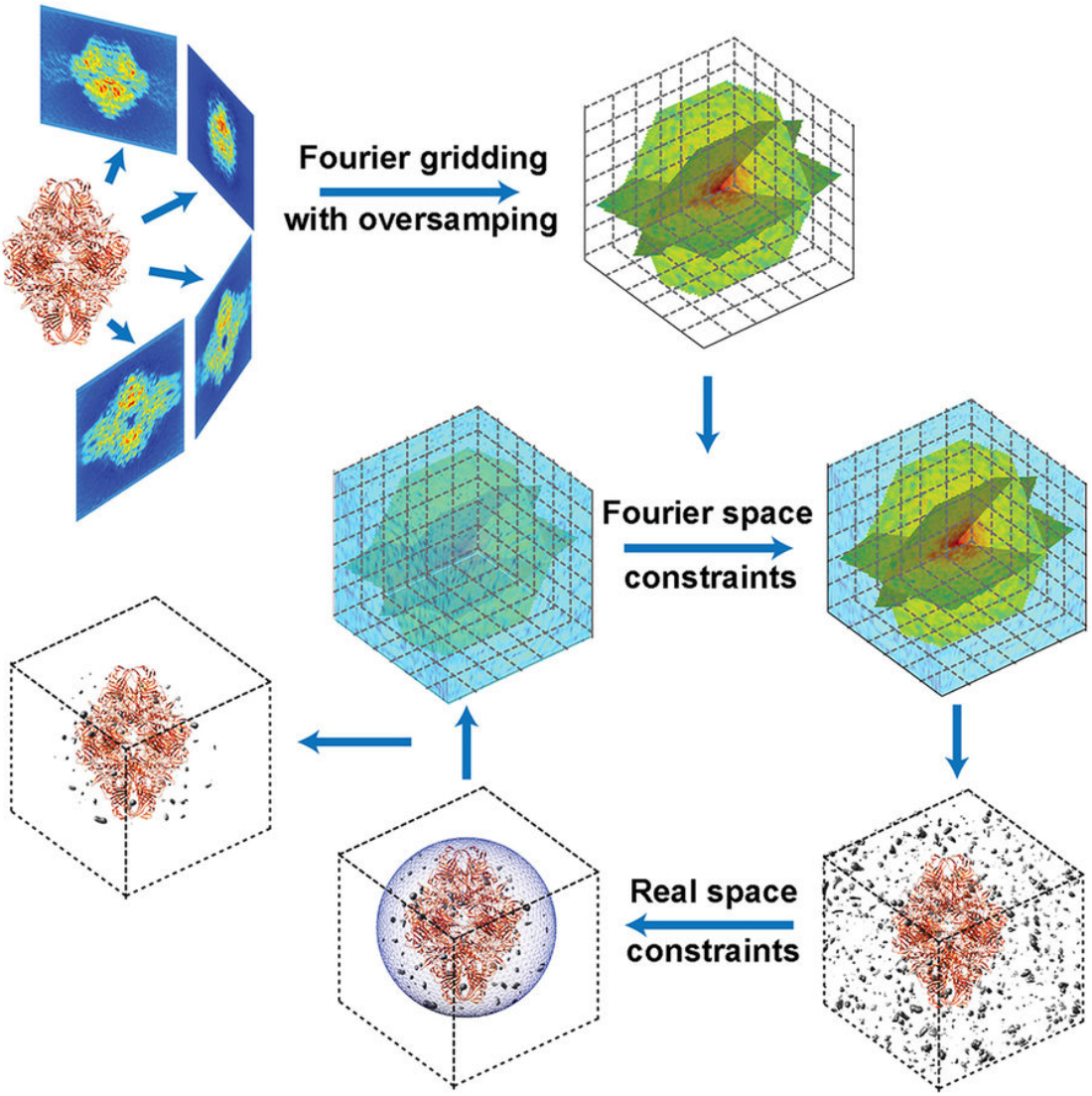

Figure 2.1: The GENFIRE algorithm. GENFIRE first computes oversampled Fourier slices from a tilt series of 2D projections. The oversampled Fourier slices are used to accurately calculate a small fraction of points on a 3D Cartesian grid based on gridding interpolation. The algorithm then iterates between real and reciprocal space. The support and positivity constraints are enforced in real space, while the small fraction of grid points corresponding to the measured data are enforced in reciprocal space. Error metrics are used to monitor the convergence of the iterative process. After several hundred iterations, the algorithm converges to a 3D structure that is concurrently consistent with the measured data in reciprocal space and the physical constraints in real space. (*Figure reprinted from [28]*)

Where S represents a support, separating the zero-padding region from the sample structure. The zero-padding region is due to oversampling. This step sets the voxels outside the support or negative valued voxels inside the support to zero, while retaining the values of the other voxels.

(iii) Apply the FFT to $p_i^{'}\vec{(r)}$ to obtain $F_i^{'}\vec{(r)}$.

(iv) Compute $F_{i+1}^{'}\vec{(r)}$ by enforcing the Fourier space constraint

$$F_{i+1}\vec{(r)} = \begin{cases} F_{obs}(\vec{k}) & \text{Known Voxels} \\ F_i\vec{(r)} & \text{Unknown Voxels} \end{cases} \tag{2.3}$$

$F_{i+1}\vec{(r)}$ is used for the $(j+1)^{th}$ iteration.

(v) Calculate two R-factors, R_k and R_{free}

$$R_k = \frac{\sum_{\vec{k}_{known}} |F_{obs}(\vec{k}) - F_i(\vec{k})}{\sum_{\vec{k}_{known}} |F_{obs}(\vec{k})|} \tag{2.4}$$

$$R_k = \frac{\sum_{\vec{k}_{withheld}} |F_{obs}(\vec{k}) - F_i(\vec{k})}{\sum_{\vec{k}_{withheld}} |F_{obs}(\vec{k})|} \tag{2.5}$$

where $\vec{k}_{known}$ represents the known voxels and $\vec{k}_{withheld}$ is a small number of randomly selected known voxels that are not used in the reconstruction. R_k is an error metric to monitor the convergence of the iterative process, while R_{free} is an unbiased free parameter to evaluate the reconstruction, which is used in crystallography [50]. R_{free} is always larger than R_k, but for a good reconstruction the two R-factors should be consistent, and significant deviation could indicate overfitting. The algorithm is reliable and usually converges within several hundred iterations. In the GENFIRE package, there is also an option to use resolution extension/suppression. For experimental data, the signal to noise ratio decreases with the increase of the spatial frequency. To compensate the high noise level at the high spatial frequency, we implement a resolution extension/suppression

technique capable of partially decoupling signal and noise through a simple modification of the way the Fourier constraint is applied. For the first iteration, only the lowest spatial frequency information is enforced. As iterations progress, higher spatial frequency data is gradually applied. This continues, forming the extension step, until half of the total number of iterations has been completed, at which point all measured data is enforced. The process is then reversed for the second half of the reconstruction, and the spatial resolution of the enforced data is gradually reduced to form the suppression step until the final iteration when only the lowest frequency information is constrained once again. While resolution extension has been implemented before [80, 81], to our knowledge, resolution extension/suppression has not been previously reported. We have performed extensive numerical simulations and observed that this technique can consistently improve the 3D reconstruction with noisy data (Fig. 2.7). See later sections for a more detailed analysis.

2.1.3 Angular refinement

The experimentally measured tilt angles may not always coincide with the true orientations of the projections. This could be the result of many causes including instrument misalignment, slipping, beam-induced motion, vibration, thermal effects, or software error. To achieve high-resolution 3D reconstruction, we implement an angular refinement procedure to reduce the tilt angle error, which consists the following four steps.

(i) An initial 3D reconstruction is computed using the experimentally measured tilt angles.

(ii) For the j^{th} projection, a series of 2D projections are calculated from the 3D reconstruction by varying the three Euler angles: $\phi \subset [\phi_j - \delta\phi, \phi_j + \delta\phi]$, $\phi \subset [\theta_j - \delta\theta, \theta_j + \delta\theta]$, $\psi \subset [\psi_j - \delta\psi, \psi_j + \delta\psi]$, where $(\phi_j, \theta_j, \psi_j)$ are the current

best fit for the Euler angles of the j^{th} projection and $(\delta\phi, \delta\theta, \delta\psi)$ are the user-defined values for the angular search ranges. Each calculated 2D projection is then compared with the corresponding measured projection, $f^j_{obs}(x, y)$, and a quality-of-fit metric is computed. The quality-of-fit metric can be implemented by either the normalized cross-correlation or the real space R-factor. For the latter, additional translational alignment between two projections have to be performed, whereas using cross correlation the translational search is performed simultaneously. The three Euler angles with either the largest cross correlation or smallest R-factor are recorded as the refined angles for the j^{th} projection.

(iii) Repeat step (ii) for all the projections and a series of the refined angles are obtained.

(iv) Obtain a new 3D reconstruction with the refined angles for all the projections.

(v) Repeat steps (ii) (iv) until no further improvement can be made.

In practice, each projection is refined in parallel, and the calculation of 2D projections from the 3D reconstruction represents the bulk of the computation. This calculation is expedited by applying the FFT to obtain an oversampled Fourier transform from the 3D reconstruction. Central slices are computed from the 3D Fourier transform using the C++ library splinterp for multithreaded linear interpolation. The inverse FFT is used to invert the central slices to the corresponding 2D projections. Care should be taken that while GENFIRE's reconstruction can find a global minimum, the current angular refinement approach may be trapped into local minima. Further developments are needed to search for a global minimum for angular refinement.

2.2 Results

2.2.1 Numerical simulations on the reconstruction of a biological vesicle

Numerical simulations on the 3D reconstruction of a 64x64x64 voxel vesicle model (Figs. 2.2a-c) were performed using GENFIRE, EST, FBP and SIRT. Simulated projections were obtained by first calculating 2D Fourier slices of the 3D model for given angles. The corresponding real-space projections was then computed by applying the inverse FFT to the Fourier slices. This code is also included in the GENFIRE package and can be accessed graphically using the *Projection Calculator*. To evaluate the performance of various reconstruction algorithms with noise, we calculated 71 projections with the tilt angle ranging -70.1° to +70.1°. Noise was added to the projections at levels similar to that observed in cryo-EM images of large biological samples. Each set of projections was reconstructed using GENFIRE, EST, FBP and SIRT. The EST and GENFIRE reconstructions were performed using a loose support, the positivity constraint and 250 iterations. The SIRT reconstruction was achieved with the positivity constraint, long-object compensation and 125 iterations.

Figures 2.2d, g, j and m show a 10-voxel-thick central slice of the 3D reconstructions in the XY plane using GENFIRE, EST, FBP and SIRT, respectively, where the z-axis is the missing wedge direction. Because there is no missing data in this direction, the reconstructions from all methods exhibit good agreement with the model (Fig. 2.2a). However, when viewed such that part of the reconstruction lies along the missing wedge direction, both GENFIRE and EST reconstructions (Figs. 2.2e, f, h and i) appear to be more isotropic and contain more fine features than FBP and SIRT (Figs. 2.2k, l, n and o). The Fourier shell correlation (FSC) between the reconstructions and the model further confirms that the GENFIRE resconstruction is superior at all spatial frequencies than other

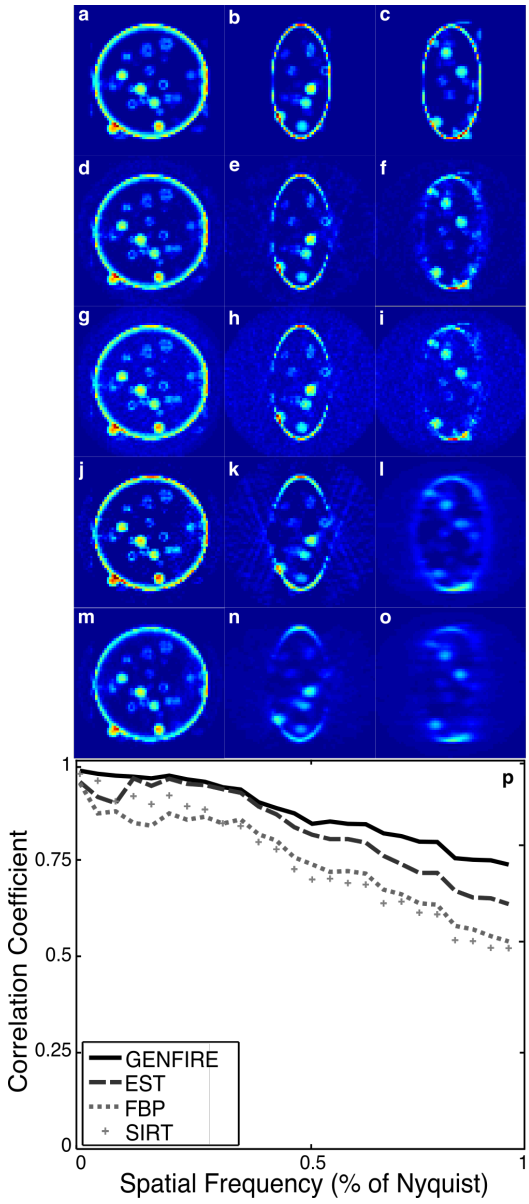

Figure 2.2: Numerical simulations on the 3D reconstruction of a biological vesicle from 71 noisy projections using GENFIRE, EST, FBP and SIRT. **(a-c)**, Three 10-voxel-thick central slices of the vesicle model in the XY, ZX and ZY planes, respectively. The corresponding three reconstructed slices with GENFIRE **(d-f)**, EST **(g-i)**, FBP **(j-l)**, and SIRT **(m-o)**, where the missing wedge axis is along the z-axis. **(p)**. The FSC between the reconstructions and the model, showing that GENFIRE produces a more faithful reconstruction than other algorithms at all spatial frequencies. (*Figure reprinted from [28]*)

algorithms. This simulation was also performed with no noise and higher noise (Figs. 2.11 and 2.12). In the case of noiseless data with equally-sloped angles, EST produces slightly better results than GENFIRE as no interpolation is needed in EST (Fig. 2.11). However, in practice this idealized scenario does not occur, and our results show that for even moderate noise levels GENFIRE produces better results. SIRT introduces a form of regularization to the reconstruction, which reduces missing wedge artifacts but also appears to compromise the resolution. By accurately assembling a small fraction of the Fourier grid points and using an iterative algorithm with resolution extension/suppression, GENFIRE is able to simultaneously reduce the effect of noise and retain higher resolution information. This capability will be important as scientists continue to solve important problems by pushing imaging systems to their limits.

2.2.2 Numerical simulations on atomic electron tomography

To quantify the GENFIRE reconstruction of 3D nanostructures at atomic resolution with noise and a missing wedge, we generated a 3D atomic model consisting of a 4.3 nm $FePt_3$ nanoparticle with a chemically ordered face-centered cubic ($L1_2$) phase. Using this model, 27 annular dark field (ADF) projections were computed with multislice simulation [82] (Energy: 300 keV, probe size: 0.5 Å, C3: 0 mm, C5: 5 mm, probe convergence semi-angle: 30 mrad, and the inner and outer detector angles: 48 mrad and 251 mrad). The angular tilt range was $\pm$ 70.1° and the pixel size was 0.4 Å. For each tilt angle, a total of 10 frozen phonon configurations were averaged. To simulate the convolution effect resulting from finite probe size and other incoherent effects, each image was convolved with a 2D Gaussian function with $\sigma = 0.51$Å. Poisson-Gaussian noise was then added to the ADF scanning transmission electron microscopy (STEM) projections.

After denoising was applied to the projections [83], this tilt series was reconstructed with GENFIRE, EST, SIRT and FBP, and the results are shown in

Fig. 2.3. Visually, GENFIRE, EST, and SIRT all demonstrate reduction of reconstruction artifacts, though the difference appears more substantial for GENFIRE and EST (Figs. 2.3a-h). Both SIRT and FBP suffer from aliasing artifacts that produce what appear to be atoms, but are not actually present in the model, outside of the true boundary of the particle (Figs. 2.3c, d, g and h). These phantom atoms would prove problematic for atom tracing and refinement in AET. The iterative methods have also successfully recovered missing information as indicated by the presence of Bragg peaks in the missing wedge (magenta arrows in Figs. 2.3i-l). Determination of 3D atomic coordinates is most accurate when the reconstruction is isotropic, thus it is important for the reconstruction algorithm to be robust to noise and the missing wedge problem. Among the four algorithms, GENFIRE produces the best reconstruction of the 3D atomic structure.

2.2.3 Angular refinement simulations

To demonstrate the improvement made by angular refinement, a simulation was performed using the same 27 ADF-STEM projections from Fig. 2.3. The orientation angle of each projection was randomly shifted by $\pm$ 2°, and a random translational shift of $\pm$1 pixel was applied along the x and y-axes. A preliminary GENFIRE reconstruction was performed and used as input to the refinement loop which was run for a total of 5 iterations with an angular search range of $\pm$ 3° with 0.2° steps and normalized cross-correlation as the error metric. The results of this simulation are shown in Fig. 2.4. The initial and refined angles were compared with the true ones using a normalized angular distance [84] (Fig. 2.4a.), resulting in an improvement from an initial average angular error of 2.1° to a refined value of 1.3°. The reconstruction is improved after angular refinement, shown in the lower right in Figs. 2.4b and c. The boundary of the nanoparticle is also better defined, with fewer artifacts around the periphery.

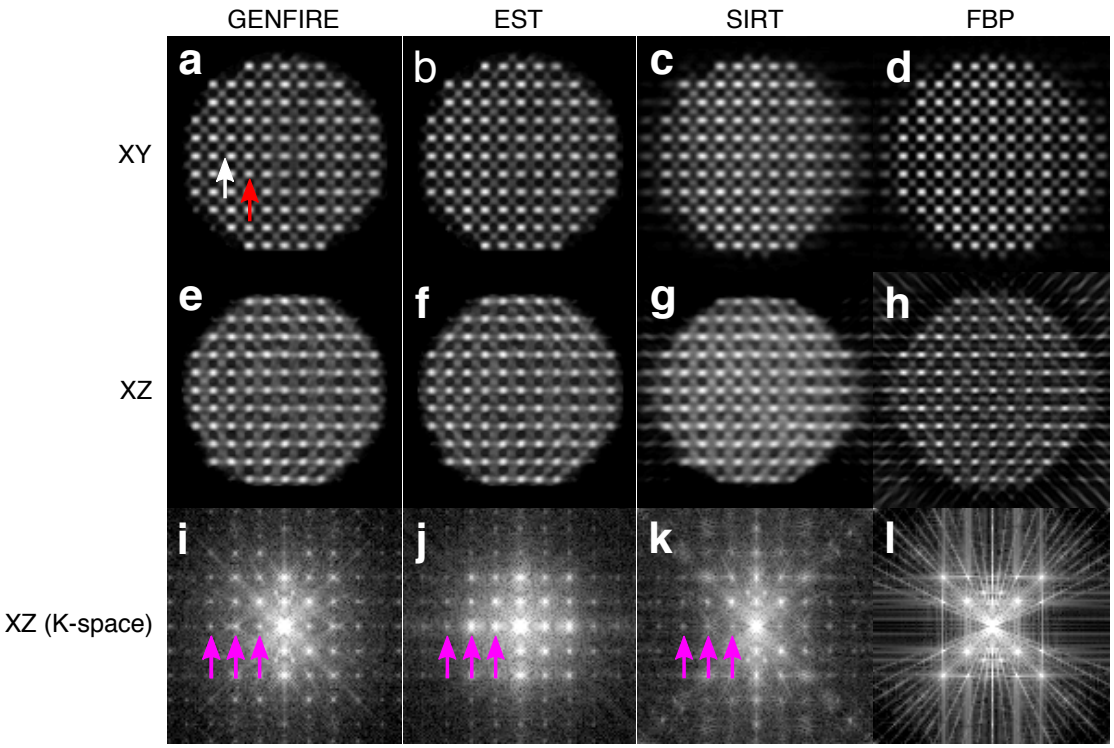

Figure 2.3: Numerical simulations on atomic electron tomography. 1.2 Å-thick central slices of a $L1_0$ phase FePt nanoparticle in the XY and ZX planes, reconstructed from 27 noisy multislice STEM projections with GENFIRE **(a, e)**, EST **(b, f)**, SIRT **(c, g)**, and FBP **(d, h)**, where the z-axis is the missing wedge direction. The red arrow indicates a Pt atom and the white arrow an Fe atom. A central slice in the ZX plane after applying the Fourier transform to the 3D reconstruction obtained by GENFIRE **(i)**, EST **(j)**, SIRT **(k)**, and FBP **(l)**, showing recovery of the Bragg peaks in the missing wedge direction for GENFIRE, EST and SIRT (magenta arrows). Artifacts due to missing wedge effects such as ghost atoms are visible in SIRT and FBP (**c, d, g,** and **h**), but are not present in EST and GENFIRE (**a, b, e** and **f**). (*Figure reprinted from [28]*)

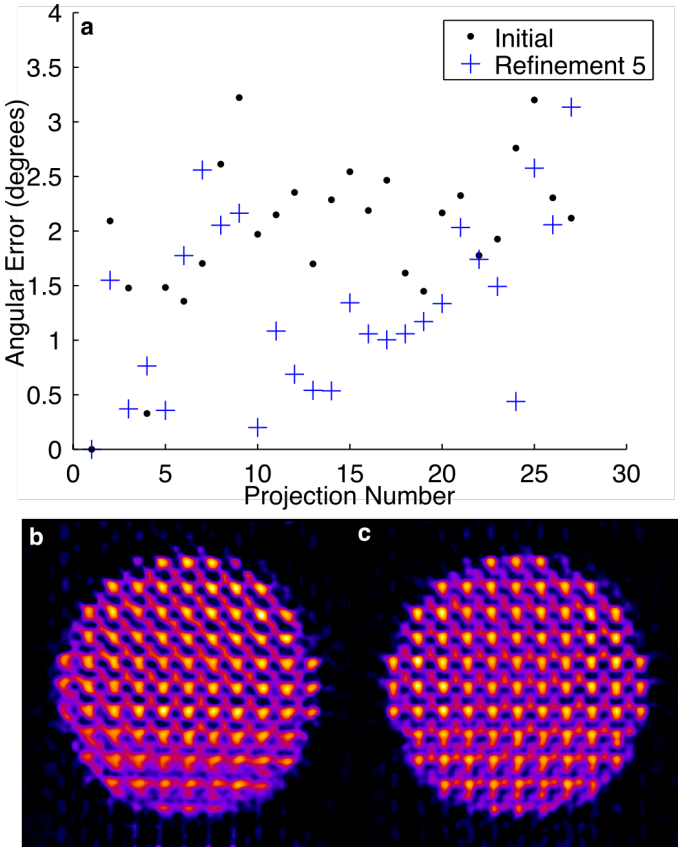

Figure 2.4: Angular refinement simulations for the GENFIRE reconstruction of the 27 multislice STEM projections used in Fig. 2.3. **(a)**. The angular difference between the initial angles and the refined ones after 5 refinement iterations, improving an average angular error from 2.1° to 1.3°. **(b)**, **(c)**. 1.2 Å-thick central slices before and after angular refinement, showing some Fe atoms in the lower left region are better resolved and the boundary of the nanoparticle is also better defined. (*Figure reprinted from [28]*)

2.2.4 GENFIRE reconstruction on experimental data of a porous material

To perform a quantitative comparison between GENFIRE and other iterative algorithms on experimental data, we acquired a tomographic tilt series of a Mo_3Si alloy annealed at 1100° C. Mo-Si and Mo-Si-B alloys are resistant to oxidation and creep and are among potential candidates with high melting temperatures to replace currently widely used Ni-based superalloys in jet engines and other high-temperature environments [85, 86]. The experiment was conducted on an FEI TitanX 60-300 in STEM mode equipped with a Gatan high-angle annular dark field detector. The microscope was operated at 200 keV with electron beam current 40 pA, a convergence semi-angle of 10 mrad, and a camera length of 91 mm. A total of 129 projections were collected with a tilt range from -58° and +70° in 1° increments. After background subtraction, the projections were aligned along the tilt axis direction by cross-correlation and along the perpendicular direction using the center-of-mass method [2, 22]. Reconstructions were performed with GENFIRE and SIRT. The SIRT reconstruction was computed using Tomo3D [87]

Figures 2.5a and b show the 13.6-nm-thick central slice of the GENFIRE and SIRT reconstruction of a fragment of the sample, revealing a complex 3D porous structure. Along the 0° direction, both GENFIRE and SIRT produce good reconstructions, although fine features are better resolved by GENFIRE (Figs. 2.5a and b). However, in the missing wedge direction, GENFIRE exhibits significant improvement over SIRT with sharper boundaries and more distinctive 3D pore structures (Figs. 2.5c and d). Figures 2.5e and f show isosurface renderings of the reconstructions, where elongation artifacts due to the missing wedge are clearly visible in the SIRT reconstruction, but are reduced by GENFIRE.

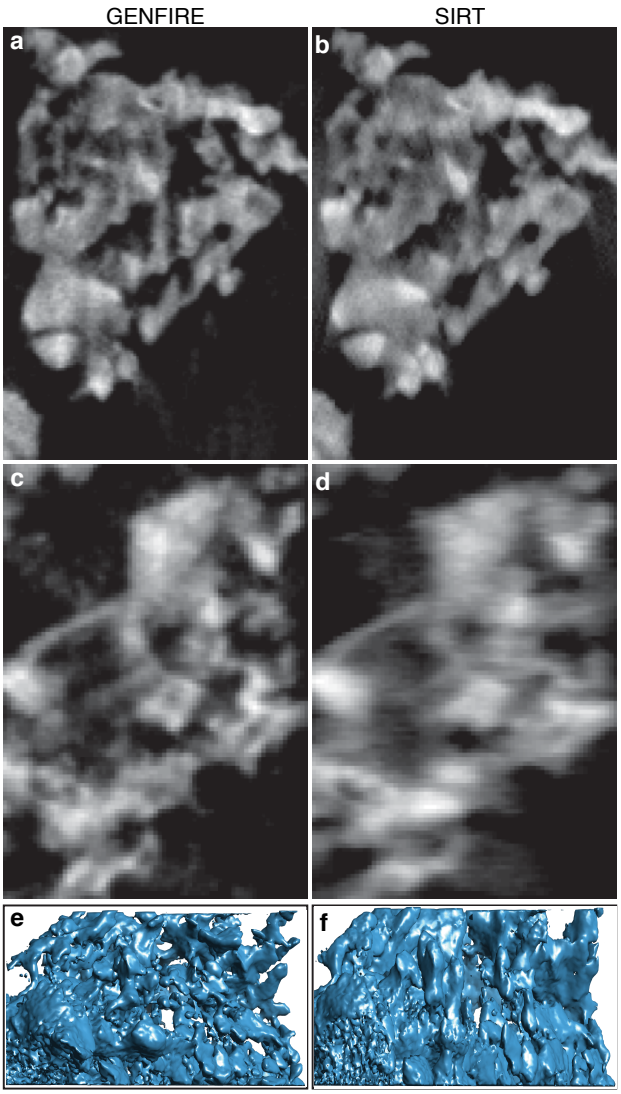

Figure 2.5: Comparison of GENFIRE and SIRT reconstructions of a fragment of porous Mo_3Si alloy, annealed at 1100° C. **(a)**, **(b)**, 13.6-nm-thick central slices along 0° direction reconstructed by GENFIRE and SIRT, respectively, where fine features are better resolved in the GENFIRE reconstruction. **(c)**, **(d)**. 13.6-nm-thick central slices of the GENFIRE and SIRT reconstructions along the missing wedge direction, where GENFIRE shows significant improvement over SIRT with sharper boundaries and more distinctive 3D pore structures. **(e)**, **(f)**. Isosurface renderings of GENFIRE and SIRT reconstructions, where elongation artifacts due to the missing wedge are visible in the SIRT reconstruction, but are reduced by GENFIRE. (*Figure reprinted from [28]*)

2.2.5 GENFIRE reconstruction of a frozen hydrated cell

GENFIRE was also used to reconstruct the 3D structure of a frozen-hydrated marine cyanobacterium in a late stage of infection by cyanophages [12]. A tilt series of 42 projections ranging from -58° to +65° were acquired on a JEM2200FS electron microscope equipped with a Zernike phase plate and recorded on a 4k x 4k Gatan CCD. The projections were binned by 4 x 4 pixels, resulting in images with approximately 1.8 x 1.8 nm^2 per pixel. The background was carefully removed from each projection based on the average value in a flat region outside of the cell. A marine cyanobacterium was then cropped out from the surrounding regions by smoothing and thresholding each projection to produce a soft-edged mask. Finally, each projection was aligned and normalized to have the same total sum as the integrated density should be conserved. The tilt series was separately reconstructed with GENFIRE and FBP (Fig. 2.6). The GENFIRE reconstruction consists with 100 iterations and a loose cubic support, while the FBP reconstruction was performed using IMOD. Several low-contrast features are visible in the GENFIRE reconstruction that are difficult, if not impossible, to identify with FBP. Of particular interest in this dataset was the interactions between the marine cyanobacterium and cyanophages. Fig. 2.6 shows a slice through the reconstructed volumes capturing the penetration of a cyanophage into the cell membrane during the infection process. This interaction has caused a local depression in the cell membrane, and the shown cross section passes through this depression as well as the viral capsid and appendage (Figs. 2.6c-j). Based on this geometry the cell membrane should be visible on both sides of the interaction, similar to taking a horizontal cross-section through a U-shape (Figs. 2.6c and d). Although the top side of the membrane is visible in both reconstructions (magenta arrows), the bottom side is only visible in the GENFIRE reconstruction (yellow arrow). Figures 2.6i and j show isosurface renderings of the penetration of the cyanophage into the cell membrane, where GENFIRE exhibits higher contrast, less peripheral

noise, more easily detectable cell boundaries than FBP.

2.2.6 Measured data enforcement via resolution extension/suppression

Most imaging methods are affected by noise to some extent, and, in many cases, noise is a serious limiting factor in final reconstruction quality. For example, single-particle cryo-electron microscopy often reports signal-to-noise ratios (SNRs) as low as 0.1. The image noise is usually modeled as a combination of Poisson (shot) noise and white Gaussian noise. Generally, the signal from the sample will decrease with spatial frequency due to effects including sample drift, thermal vibrations, energy spread of the electron beam, and lens transfer functions. Therefore, in general the signal-to-noise ratio (SNR) decreases as a function of spatial frequency. Maximization of resolution in the final reconstruction is desirable, but one must be careful to avoid overfitting of the model to noise which can lead to artificially enhanced resolution estimates and difficult density interpretation. Most modern methods of avoiding this problem rely on accurate determination of various metrics of the data such as spectral signal-to-noise ratio to determine ideal low-pass filtering for noise suppression. However, these filters suppress both the noise and the signal of the sample at high resolutions. Here we present a novel idea that is capable of partially decoupling signal and noise and high resolutions through a simple modification of the way the Fourier constraint is applied that we have called resolution extension/suppression. To understand how this can be achieved, consider the following model for the assembled frequency space

$$M(\vec{k}) = F(\vec{k}) + \epsilon(\vec{k}) \tag{2.6}$$

where $F(\vec{k})$ is the Fourier component of the sample at frequency $\vec{k}$ and $\epsilon(\vec{k})$ is an error component due to a combination of noise, projection misalignment, and interpolation error. The key concept behind resolution extension/suppression is that all frequency components $F(\vec{k})$ are correlated as they correspond to the same

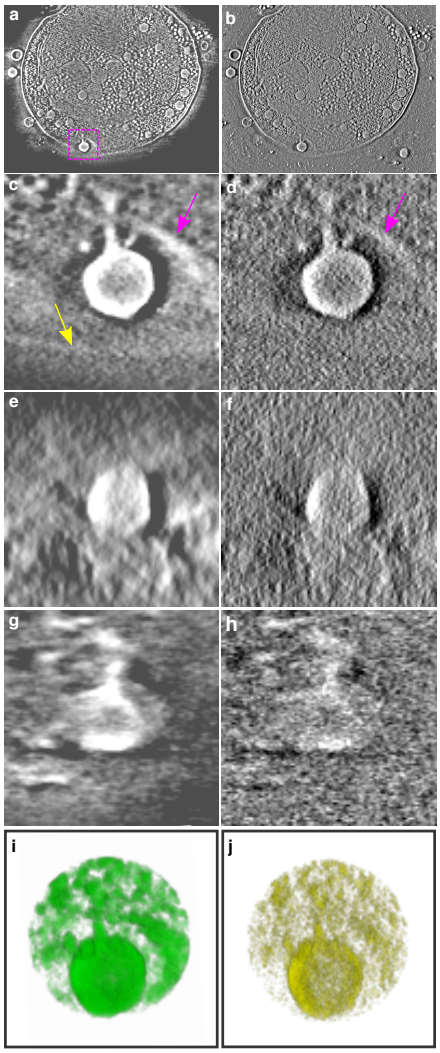

Figure 2.6: 3D structure of a frozen-hydrated marine cyanobacterium, capturing the penetration of a cyanophage into the cell membrane. a, b, 5.43nm-thick slices of the cell in the XY plane reconstructed by GENFIRE and FBP, respectively. Magnified views of the penetration of a cyanophage for the GENFIRE and FBP reconstructions in the XY **(c, d)**, XZ **(e, f)**, and ZY **(g, h)** planes, respectively. The top side of the membrane is visible in both reconstructions (magenta arrows), but the bottom side is only visible with GENFIRE (yellow arrow). **(i, j)**. Isosurface renderings of the penetration of the cyanophage to the cell membrane. Overall, GENFIRE exhibits higher contrast, less peripheral noise, more easily detectable cell boundaries than FBP. (*Figure reprinted from [28]*)

object, whereas the $\epsilon(\vec{k})$ are uncorrelated. For the true structure, $\rho(\vec{x})$, all of the $F(\vec{k})$ can exist simultaneously and satisfy the appropriate real space constraints. The presence of the error component $\epsilon(\vec{k})$ changes this. For example, noisy high-resolution datapoints can introduce spurious density known as "dust" throughout the reconstruction which may disagree with the overall boundary of the sample determined by the low resolution information, which is less noisy. However, this high frequency data also contains true high-resolution signal, which is entirely compatible with the low-frequency data from the sample, and may be partially extracted by exploiting this disparity in the following way. For the first few iterations, only the lowest frequency information is enforced in Fourier space. This low-resolution recovery period establishes an initial sample boundary with as little corruption from noise as possible. The resolution cutoff for enforcement is then extended outward periodically until the full set of $M(\vec{k})$ are being enforced. At this point the reconstruction contains both signal at all resolutions and noise. The process is then reversed for the resolution suppression step until for the final iterations only the lowest resolution information is being enforced once again. Mathematically, we use Q_k to represent the set of measured points that lie within the k^{th} resolution cutoff. By reconstructing in this way, priority is given to the less-noisy, low resolution data wherever a conflict arises as previously described, diminishing the higher frequency $\epsilon(\vec{k})$ while partially preserving the corresponding $F(\vec{k})$ yielding a stronger SNR at high spatial frequencies. This decoupling is not perfect as it is possible that some high frequency $F(\vec{k})$ components are perturbed by changes made to intermediate $F(\vec{k})$ components during the resolution suppression process; however, our results indicate the improvement made by this technique at all resolutions is substantial for noisy data.

A comparison of GENFIRE's performance with and without the use of resolution extension/suppression is shown in Figs 2.7 and 2.8. The projection data for this simulation is the same as from Fig. 2.2. A notable difference is that al-

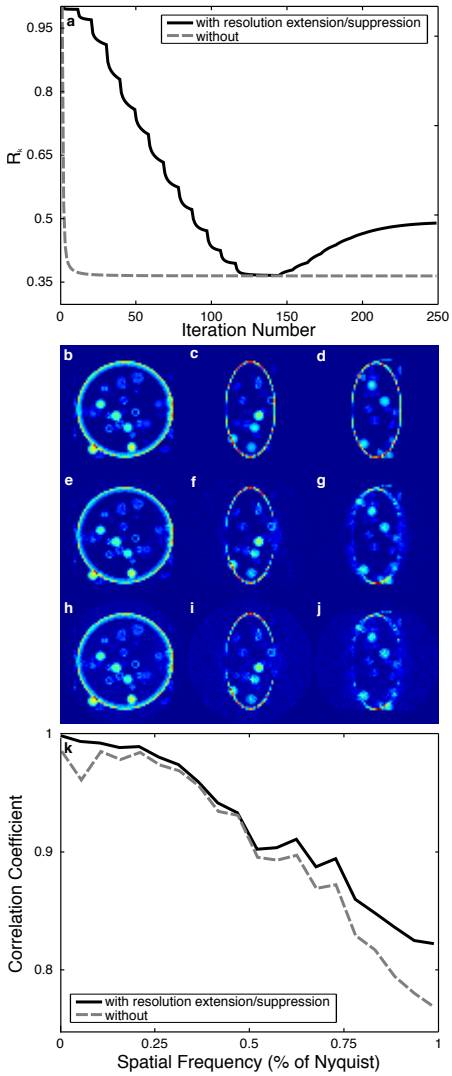

Figure 2.7: **(a)**. Reciprocal-space error vs iteration number for GENFIRE with and without the use of the resolution extension/suppression technique. The abrupt dips in error over the first half of iterations correspond to events where the Fourier constraint is expanded. **(b–d)** Projections of the model vesicle are shown along the three principle axes, with corresponding views for GENFIRE reconstructions with resolution extension/suppression **(e–g)** and without **(h–j)**. **(k)** Fourier shell correlation between each reconstruction and the model indicating that GENFIRE with resolution extension produces a better reconstruction at all spatial frequencies despite the larger reciprocal error. This claim is supported by the visual quality of the reconstruction depicted in **(b–j)**. (*Figure reprinted from [28]*)

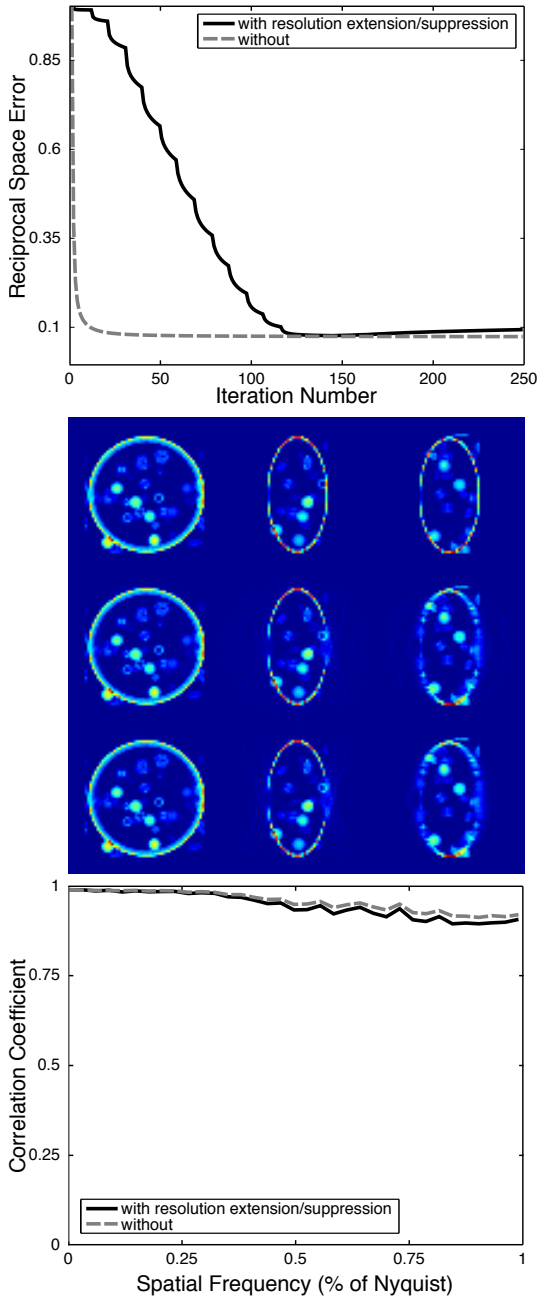

Figure 2.8: Similar to Fig. 2.7 but with no noise. (*Figure reprinted from [28]*)

though the reconstruction is better across all spatial frequencies with resolution extension/suppression, as indicated by the Fourier Shell Correlation (FSC), the reciprocal error is higher. The small dips every few iterations correspond to each increase in the resolution cutoff for the constraint set. The minimum error is achieved at the end of the extension step, and then begins to rise again during suppression. The reason for the increased error is that the true structure does not match the values of the (noisy) measurements. By enforcing only the less noisy low resolution values for the latter iterations, the structure is changed in a way that improves the quality of the reconstruction with respect to the model but not to the measurements. Therefore, although the reciprocal space error serves as a sign of convergence, its value is not necessarily a measure of quality of reconstruction. The same simulation for the noiseless case is shown in Fig. 2.8. Here the result produced with resolution extension/suppression is slightly worse than without. This is likely due to the previously mentioned phenomena of high frequency components being perturbed during the suppression step. Although the technique of resolution extension/suppression does not appear to be universally superior, it is worth noting that the improvement for the noisy data is substantially larger than the decrease in quality for the no-noise case. Some datasets may benefit more than others from this method, and it may easily be turned on/off in the GUI. Such a technique could find applications as a method of structure refinement in fields where projection data is noisy, such as single-particle cryo-EM.

2.2.7 Complex free R factor

In crystallography it is common practice to prevent overfitting of the data during refinement by using a free R factor where a small percentage, usually 5%, of the data is withheld from refinement, and the refined values are compared to the withheld ones. If the value of R_{free} is too large, it is a good indicator that the data has been overfit. Following similar logic, we note that avoiding overfitting

of noise during an iterative reconstruction algorithm is an analogous problem, and we introduce the slightly modified version in this manuscript. Whereas only Fourier magnitudes are measured directly in crystallography, real-space imaging methods detect phase information. In a real experiment the true structure is never exactly known, so for GENFIRE R_{free} serves as a cross-validation metric for the self-consistency of the data by monitoring its ability to reconstruct itself. If fault exists with either the reconstruction method used or the data, be it due to noise, misalignment, or otherwise, then it would be difficult to faithfully recover withheld data points. Therefore, reasonably low values of R_{free} should be a strong indicator that the reconstruction has not been overfit and the data quality is good. Generally accepted limiting values for R_{free} for magnitudes in crystallography are around 0.4 in the highest shell, so one should expect a higher value for complex R_{free} at equivalent levels of reconstruction quality.

Fig. 2.9 summarizes the results of R_{free} when applied to the simulation in Fig. 2.2 above. For low-noise data the mean value of R_{free} should mirror the trend in the reciprocal error and be slightly higher. The value of R_{free} vs. spatial frequency generally trends upwards, as the low frequency information is easiest to retrieve. In this simulation the value of R_{free} is low at all spatial frequencies and is indicative of a reconstruction that is not overfit.

2.2.8 Comparison of gridding with DFT and FFT

GENFIRE provides two variations of the gridding routine. The first method is the most accurate, but is computationally slower. This method uses the Discrete Fourier Transform (DFT) to calculate the value of the Fourier Transform at the exact frequency corresponding to the nearest point-to-plane distance from the grid point to the plane of the measured projection. Practically this is accomplished in the following way. First, a unit-normal vector is defined along the z-axis for each projection. These vectors are rotated by the corresponding Euler angles to form a

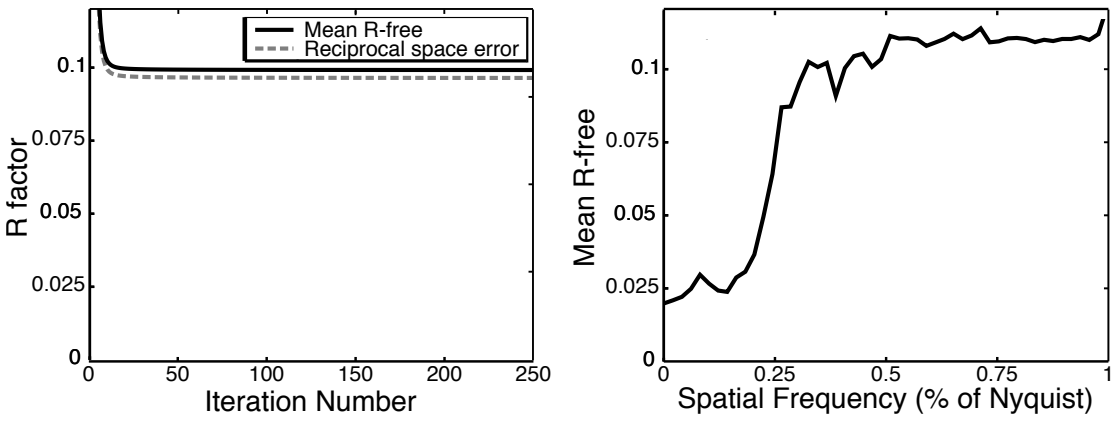

Figure 2.9: **(left)** A comparison of R_{free} and R_k vs iteration number. R_{free} is highly correlated with, but slightly higher than, R_k and is indicative of a good reconstruction. Divergence between the two indicates overfitting. **(right)** average R_{free} vs spatial frequency, indicating higher resolution features are more difficult to recover. (*Figure reprinted from [28]*)

set of rotated vectors that define a series of continuous planes in 3D. Next, for each grid point in the 3D Fourier space to be assembled, the scalar distance is computed to each plane by a geometric projection of the vector location of the grid point onto the corresponding rotated normal vector. For the subset of point-to-plane distance pairs that lie within the chosen interpolation radius, the vector location of the nearest point is determined, and a corresponding measured value $F(\vec{k_i})$ is obtained through evaluation of the DFT. The final gridded value $M(\vec{k})$ is determined from this set of $F(\vec{k_i})$ using the averaging scheme described previously. The second method accelerates the gridding through use of the Fast Fourier Transform (FFT). First, the 2D FFT of each projection is calculated to obtain a set of evenly spaced Fourier components. The spatial frequency coordinates for each of these values are rotated by the corresponding Euler angles to form a set of measurements in 3D. For each grid point, the Euclidean distance is computed to each measured grid point, and the subset of points that lie within the interpolation kernel are used to evaluate $M(\vec{k})$ in the same way as described previously. A comparison

of these gridding methods is shown in Fig. 2.10. The DFT method produces a reconstruction that is better across all spatial frequencies and converges to a slightly lower reciprocal error value. The advantage of the DFT method is the freedom to calculate the Fourier component at any frequency $\vec{k_i}$. Therefore the set of $F(\vec{k_i})$ produced with the DFT method will have interpolation distances that are strictly less than or equal to those of the FFT method, producing a more faithful representation of the true Fourier space. The FFT method, conversely, produces a set of Fourier values arranged on a predefined grid from which the 3D Fourier space is assembled. The advantage of this method is one of speed. The use of the DFT means the first method has complexity $O(n^2)$, while the second has $O(nlog(n))$ complexity. The DFT method should always produce better reconstructions, but for large array sizes becomes time-consuming. Thus, a normal workflow can consist of preliminary reconstructions performed quickly with FFT gridding with the potential for a final result from the DFT method. The gridding process also could be accelerated with GPUs in future versions.

2.2.9 Comparison of reconstruction methods for additional noise levels

Additional simulations were performed following the same procedure used in Fig. 2.2 with no noise (Fig. 2.11) and high noise (Fig. 2.12). The same equally-sloped tilt angles and reconstruction parameters were used for each method. For the no-noise case, EST slightly outperforms GENFIRE. This is because GENFIRE uses a gridding routine, whereas the pseudopolar FFT used by EST is mathematically exact. However, the difference is quite small, indicating that the oversampled interpolation routine used by GENFIRE is quite accurate. Both methods provide a significant improvement over SIRT and FBP. SIRT produces a reconstruction that is better than FBP at low resolution, but has the lowest FSC at higher spatial frequencies, which is likely because the SIRT algorithm acts as a form of regularization. With higher noise, both Fourier-based iterative methods still produce the

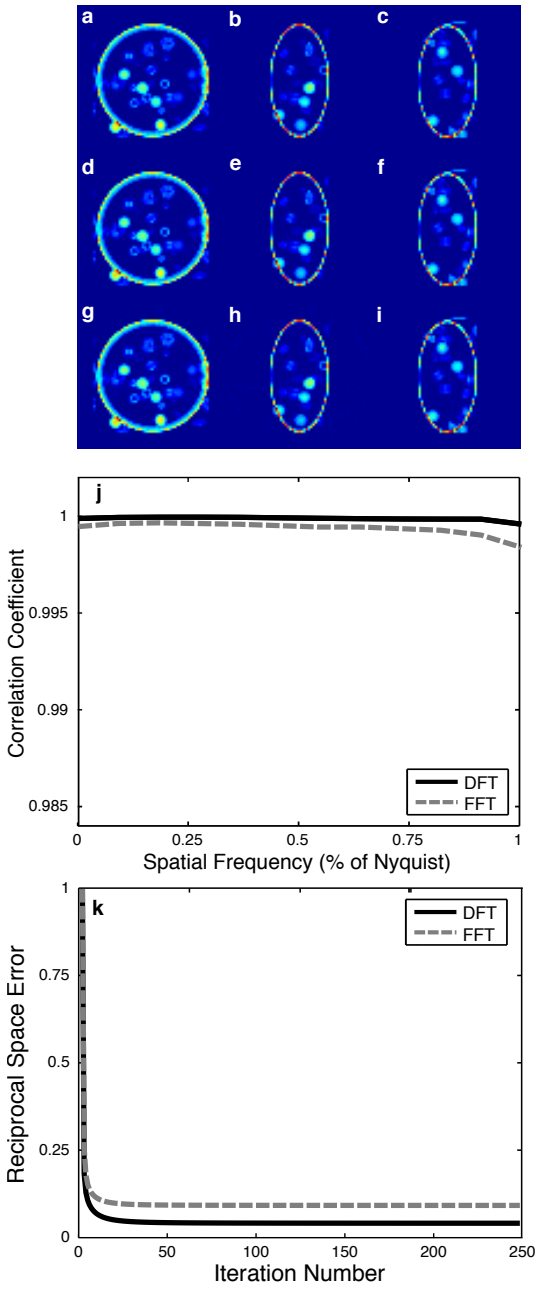

Figure 2.10: Comparison of FFT/DFT gridding methods available in GENFIRE. Central slices in xy, yz, and xz planes are displayed for **(a-c)** the model, **(d-f)** GENFIRE with DFT gridding, and **(g-i)** GENFIRE with FFT gridding. **(j)**. Fourier Shell Correlation curve between the model and reconstructions, indicating the DFT method produces superior reconstructions at all spatial frequencies. **(k)** Reciprocal space error vs iteration with a deeper minimum found for the DFT gridding method. (*Figure reprinted from [28]*)

best reconstructions, but the improvement of GENFIRE over EST is enhanced. This is due to the use of resolution extension/suppression for enforcement of the Fourier constraint as well as the capability of GENFIRE to combine multiple noisy measurements into a single, less noisy grid point. SIRT performs better under this circumstances relative to the other methods, and for the highest noise level used here is actually slightly better than EST at high resolution. This is indicative that the EST reconstruction has suffered from some degree of overfitting in the presence of heavy noise. This issue can be alleviated by introducing regularization methods like non-local total variation minimization or other denoising techniques. However, these can limit resolution. The new techniques introduced by GENFIRE appear to reduce the effect of the noise while preserving more of the high resolution information, providing necessary tools for creating powerful reconstruction algorithms for application towards solving difficult scientific problems.

2.2.10 Focused ion beam milling and denoising of frozen samples

Focused ion beam (FIB) milling is a technique traditionally used in materials science with increasing applications to studies of biological samples in cryo-EM [88–90]. Frozen samples naturally suffer reduced contrast due to the surrounding ice, and this is a particular problem for tomography as an embedded sample is not truly isolated, resulting in density moving into and out of the field of view as the sample is tilted. One potential method for alleviating this problem is to use a FIB to remove ice surrounding a frozen sample, forming a bridge parallel to the tilt axis. If the ice layer is thin enough and the field of view large enough to capture the full rotation of the milled sample as it rotates, the sample becomes isolated and a 3D reconstruction can be obtained with improved contrast and greater fidelity.

To demonstrate this, the following simulation was performed using an electron density map of the human ribosome at 3.4 Å resolution (EMBD 4214). The

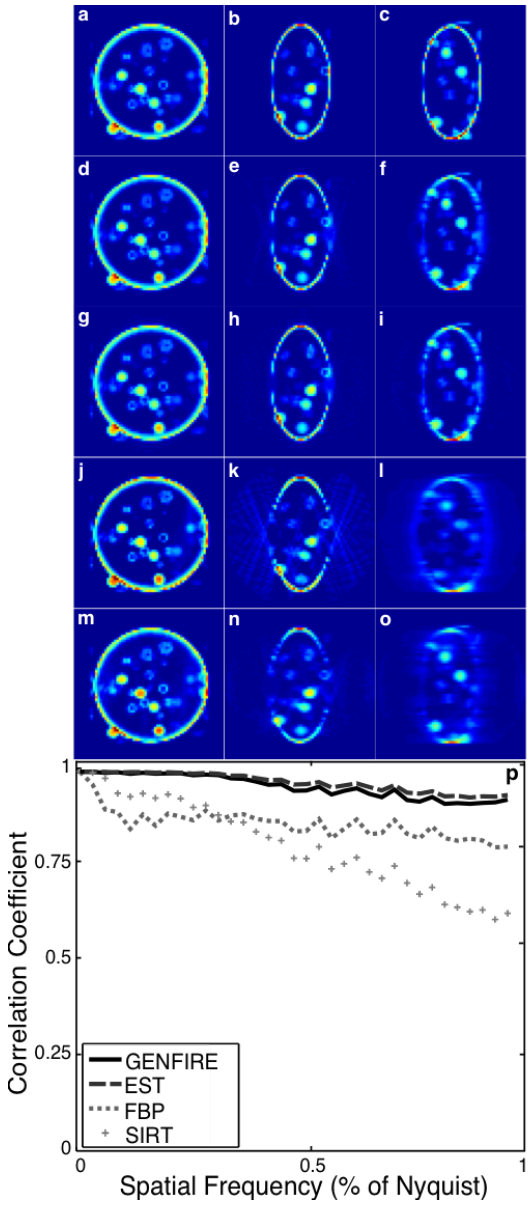

Figure 2.11: Numerical simulations on the 3D reconstruction of a biological vesicle from 71 noise-free projections using GENFIRE, EST, FBP and SIRT. **(a-c)**. Three 10-voxel-thick central slices of the vesicle model in the XY, ZX and ZY planes, respectively. The corresponding three reconstructed slices with GENFIRE **(d-f)**, EST **(g-i)**, FBP **(j-l)**, and SIRT **(m-o)**, where the missing wedge axis is along the z-axis. p, The FSC between the reconstructions and the model, showing that GENFIRE produces a more faithful reconstruction than other algorithms at all spatial frequencies. (*Figure reprinted from [28]*)

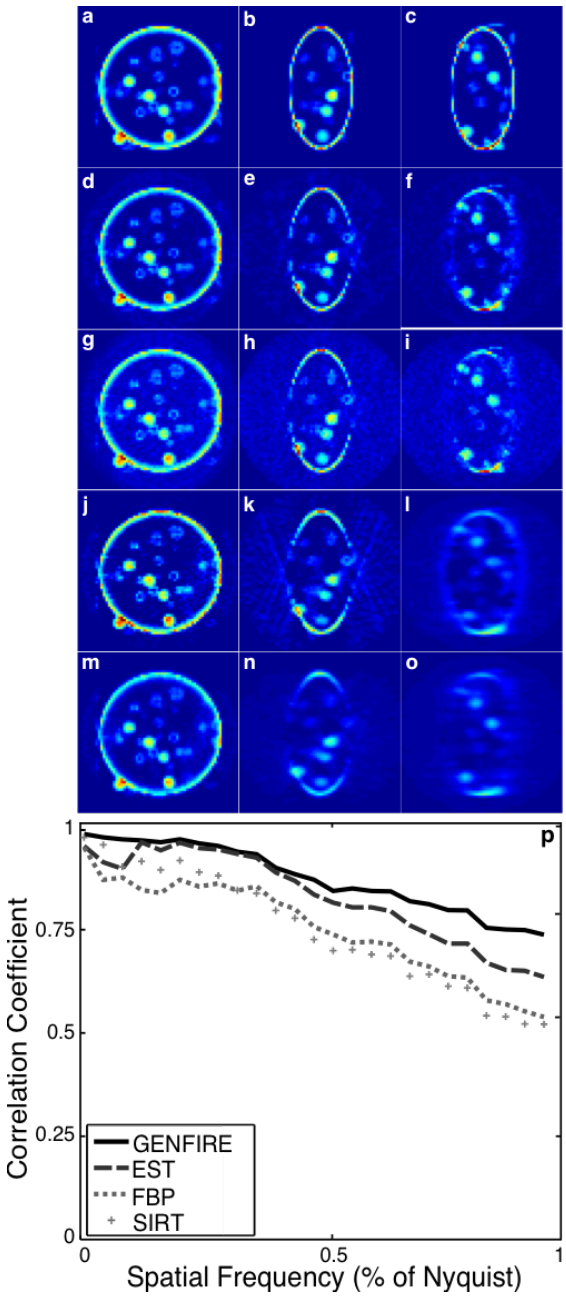

Figure 2.12: Similar to Fig. 2.11, but with high levels of noise. (*Figure reprinted from [28]*)

model was binned 2 x 2 and embedded in vitreous ice approximately 100nm thick. Projections were then calculated with 29 evenly spaced tilt angles between ± 70°. A second model was then created by applying a mask to simulate the effect of FIB milling, and a similar set of projections was produced. Poisson noise was added to both sets of projections to levels comparable to experimental levels. A third set of projections was produced by applying a modified version of the BM3D algorithm intended to tolerate amorphous samples such as biological soft tissue [83]. These datasets were reconstructed using FBP and GENFIRE, and the results are summarized in 2.13.

A representative projection at 45° visually demonstrates the increased density at higher tilts due to the presence of ice outside of the original field of view (Fig. 2.13a) as well as the positive effect of FIB milling (Fig. 2.13b). Denoising significantly improves the quality of the projection (Fig. 2.13c). A comparison of the Fourier shell correlation between the reconstructions and the model (Fig. 2.13d) indicates significant reconstruction improvement as a result of applying GENFIRE, FIB, and the BM3D denoising technique. Even with the use of a more primitive reconstruction algorithm like FBP the effect of FIB milling alone improves reconstruction fidelity. Ultimately the resolution improved in this simulation from using FBP on the original dataset to using GENFIRE with FIB and BM3D from approximately 11.1Å to 6.8Å. We note that this denoising technique is experimental, and for this simulation the noise model was well-defined; however, the technique shows great promise and should be explored in future works.

2.3 Discussion

In this article, we present the mathematical implementation of GENFIRE for 3D reconstruction from a limited number of projections with a missing wedge. Both numerical simulation and experimental results of materials science and biological

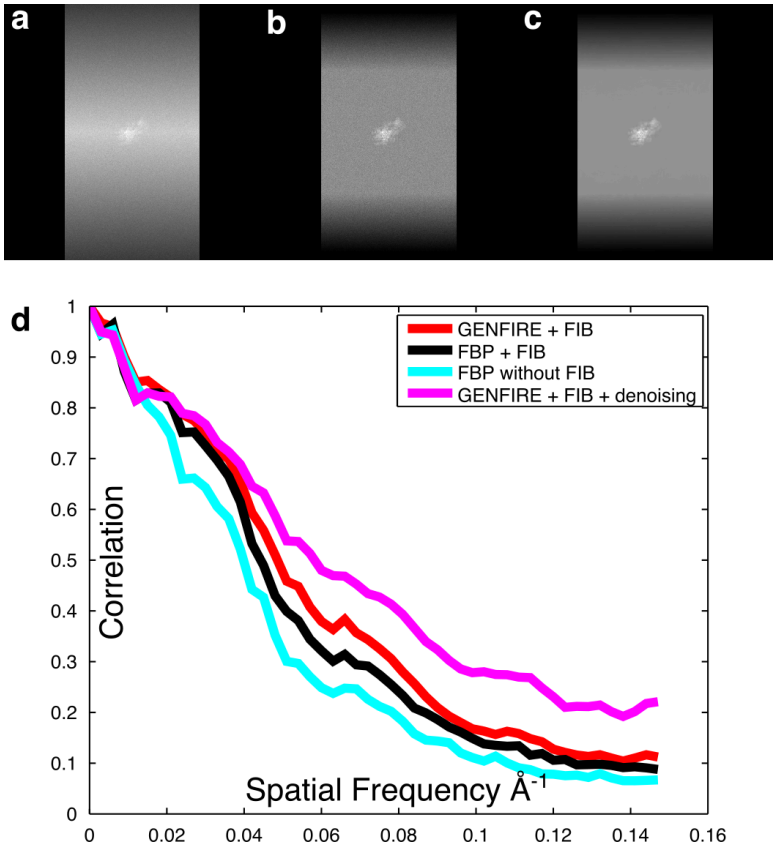

Figure 2.13: Application of GENFIRE in combination with focused ion beam milling and BM3D denoising. 45° projection of ribosome **(a)** embedded in virteous ice with noise, **(b)** with surrounding ice removed by FIB milling, and **(c)** with denoising applied to the projection in **(b)**. **(d)** Fourier shell correlation between reconstructions and the known model, indicating that significant resolution improvement may be obtained through the combination of these methods.

specimens indicate that GENFIRE produces superior 3D reconstruction to several other tomographic algorithms. As a Fourier-based iterative method, GENFIRE first computes a small fraction of Cartesian grid points with high precision from 2D projections using Fourier gridding and oversampling. It then iterates between real and reciprocal space using the FFT and its inversion. Positivity and support are enforced in real space, while the grid points calculated from the measured data are applied in reciprocal space. As the Fourier data, positivity and support are all convex constraint sets, GENFIRE belongs to the method of projections onto convex sets, whose convergence has been mathematically proven [91, 92]. This allows GENFIRE to search for a global solution that is concurrently consistent with the measured data and physical constraints. One of the unique features of Fourier-based iterative algorithms such as GENFIRE is that any changes in real space globally affect all the points in reciprocal space and vice verse. This global correlation between real and reciprocal space makes GENFIRE robust to the missing data and missing wedge. In contrast, ART, SART and SIRT perform all the iterations in real space through local interpolation. When there is a missing wedge, the local interpolation in that region becomes less accurate. This explain why GENFIRE achieves better 3D reconstructions than several other tomographic algorithms. Furthermore, compared to EST that is only applicable to single tilt axis data, GENFIRE can not only work with any tomographic geometry, but also perfroms faster due to the use of the FFT and its inversion for iteration. It must be cautioned, however, that GENFIRE users must be aware of the physical implications of the conditions under which images are acquired with respect to the linearity of the projection. Although nonlinear effects such as dynamical scattering can be alleviated due to a rotational average in tomography [1], the exact extent to which such nonlinear effects degrade GENFIRE needs to be explored in future work.

Another class of tomographic reconstruction methods based on compressed

sensing is presently under rapid developmenet [93, 94]. Compressed sensing assumes that a physical meanful structure is sparse in some domain. If the sparse domain can be found, the 3D structure can in principle be reconstructed from a comparatively small measurement. Compressed sensing tomography typically incorpoartes mathematical regularization such as total variation minimization [95], which requires extensive manual tuning of parameters [96]. This is acceptable in applications such as medical magnetic resonance imaging, where the scope of reconstruction targets is limited enough to permit a specialized set of parameters. However, for a generalized tomographic reconstruction, it is not straightforward to optimize these parameters, especially with the presence of missing data and noise. For example, it would be very challenging, if not impossible, for compressed sensing tomography to reconstruct the 3D distribution of point defects in a crystalline specimen. Conversely, GENFIRE uses very general physical constraints and requires minimum manual tuning of parameters. It has recently been used to determine crystal defects such as grain boundaries, chemcial order/disorder, anti-phase boundaries and point defects with unprecendent 3D detail (Chapter 5) [1, 3]. Furthermore, GENFIRE can be easily adapted to incorporate mathematical regularization to reconstruct 3D sparse objects from a small number of projections. Looking forward, we expect GENFIRE can be applied to a plethora of imaging modalities to address a wide range of scientific problems.

2.4 Software Availability

The GENFIRE software package with a graphical user interface is freely available at www.genfire-em.com.

CHAPTER 3

Correlative cellular ptychography with functionalized nanoparticles at the Fe L-edge

Precise localization of nanoparticles within a cell is crucial to the understanding of cell-particle interactions and has broad applications in nanomedicine. Here, we report a proof-of-principle experiment for imaging individual functionalized nanoparticles within a mammalian cell by correlative microscopy. Using a chemically-fixed HeLa cell labeled with fluorescent core-shell nanoparticles as a model system, we implemented a graphene-oxide layer as a substrate to significantly reduce background scattering. We identified cellular features of interest by fluorescence microscopy, followed by scanning transmission X-ray tomography to localize the particles in 3D, and ptychographic coherent diffractive imaging of the fine features in the region at high resolution. By tuning the X-ray energy to the Fe L-edge, we demonstrated sensitive detection of nanoparticles composed of a 22 nm magnetic Fe_3O_4 core encased by a 25-nm-thick fluorescent silica (SiO_2) shell. These fluorescent core-shell nanoparticles act as landmarks and offer clarity in a cellular context. Our correlative microscopy results confirmed a subset of particles to be fully internalized, and high-contrast ptychographic images showed two oxidation states of individual nanoparticles with a resolution of ~16.5 nm. The ability to precisely localize individual fluorescent nanoparticles within mammalian cells will expand our understanding of the structure/function relationships for functionalized nanoparticles.

3.1 Introduction

Functionalized nanoparticles are used in a broad array of nanomedicine applications for their utility as labels and drug delivery systems [97–100]. The ability to localize individual nanoparticles within cells is critical as it allows interactions between the nanoparticles and their target cells to be characterized, informing of the biological effects imparted by the nanoparticles. One method ideally suited to probe individual nanoparticles inside cells is coherent diffractive imaging (CDI) as it can image thick specimens with high resolution and contrast [10, 38, 64, 66, 67, 101–113]. Since the first experimental demonstration in 1999 [64], various CDI methods have been developed [70] and a particularly powerful approach for imaging extended objects such as whole cells is ptychographic CDI (also known as ptychography) [114–129].

In ptychography, an extended sample is observed by illuminating with a coherent wave via a 2D raster scan. During such a 2D scan, diffraction patterns are recorded from overlapping fields of views with a pre-defined trajectory. The overlap between views can then be used as a strong constraint in phase retrieval algorithms [118], leading to a unique, robust reconstruction of the complex exit wave of the object and the illumination function [115, 117, 119–130]. Furthermore, by measuring diffraction intensity with a numerical aperture significantly higher than that of X-ray lenses, ptychography can reach spatial resolution far beyond those of conventional X-ray microscopy. However, this powerful capability is hampered in the case of weakly scattering objects such as biological specimens, because the background scattering of the substrate and parasitic scattering from X-ray optics can dominate the weak signals from a biological specimen [117, 119, 125, 128, 130]. Here we demonstrate a correlative ptychographic approach for high-resolution imaging of functionalized nanoparticles internalized within an unsectioned mammalian cell. To achieve high spatial resolution and

image contrast, we first adapt transparent graphene-oxide substrates [131] to support cells during the X-ray imaging process. Graphene and graphene-oxide films have previously been shown to be an excellent support for high resolution electron microscopy studies of cells and macromolecules, both frozen-hydrated [132] and in-situ [133–135]. Graphene-oxide in particular shows excellent biocompatibility promoting cellular adhesion [136–139] and growth. These substrates offer a significant reduction in background scattering for X-rays in the soft X-ray regime compared to conventional substrates. Next, we label HeLa cells with core-shell nanoparticles, functionalized by the addition of a fluorescent moiety and a superparamagnetic core, and identify a region of interest using a fluorescence microscope. Finally, we combine 3D localization of nanolabels within the cell, using scanning transmission X-ray microscopy (STXM) tomography, with correlative high-resolution ptychographic imaging, with enhanced contrast for the nanoparticles by tuning the X-ray energy to the Fe L-edge. This correlative cellular imaging method allows us to localize individual nanoparticles in a cellular context at multiple length-scales, ranging from tens of microns to the ten-nanometer level.

3.2 Results

3.2.1 Nano-labeling of HeLa cells with fluorescent nanoparticles on a graphene-oxide substrate

HeLa cells were first grown on a substrate specifically engineered for high contrast imaging, consisting of a commercially available gold TEM grid coated with lacey carbon (Ted Pella) on top of which we deposited a few layers of graphene-oxide (www.graphenesupermarket.com) using the drop casting method [131]. Graphene-oxide is biocompatible and allows for the adherent growth of HeLa cells while being effectively invisible to the soft X-ray probe (Fig. 3.3, Fig. 3.4). These grids provide significantly enhanced contrast when using the Nanosurveyor endstation in both

STXM and ptychography modes (Fig. 3.1). We attribute the improved stability and contrast to the atomically thin composition of the graphene layers and to the low density of graphene oxide relative to conventional silicon nitride-based supports. Graphene-oxide and silicon nitride have approximate densities of 1.9 g/cm^3 and 3.4 g/cm^3, respectively.

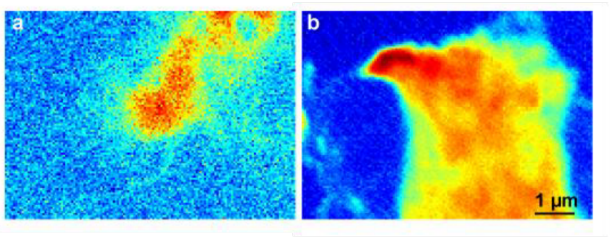

Figure 3.1: Comparison of STXM images on two different substrates. STXM images of the edge of a HeLa cell on **(a)** 50 nm thick Si_3N_4 with a 2 ms dwell time and **(b)** atomically thin graphene oxide with a 3 ms dwell time. The SNR, defined as the quotient of the average intensity inside the sample and the standard deviation of the surrounding region, is approximately 2.9 and 12.1, respectively, which is well beyond the effect of the difference in exposure time. The STXM probe was moved in 50 nm increments with a 100 nm focal spot size. (*Figure reprinted from [140]*)

We imaged cells treated with fluorescent, core-shell mesoporous silica particles with an iron oxide core (Fig. 3.2). Cells treated with nanoparticles were suspended in growth media for 30 minutes before gentle washing to remove excess nanoparticles, leaving mainly nanoparticles that had interacted with the cell surface or had been internalized. All samples were chemically fixed with paraformaldehyde, washed, and desiccated prior to imaging.

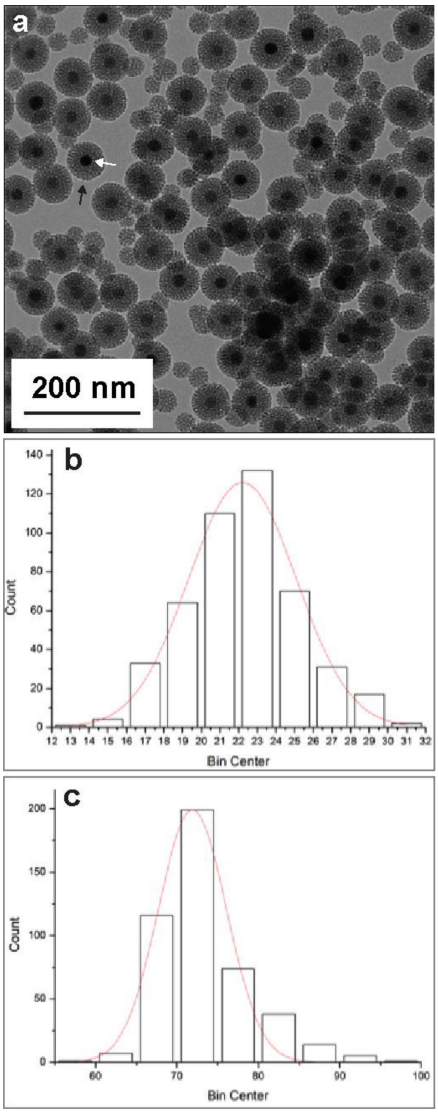

Figure 3.2: Structural analysis of Fe_3O_4/SiO_2 (core-shell) nanoparticles. **(a)** TEM image of core-shell nanoparticles; scale bar, 200 nm. White arrow points to Fe_3O_4 core, black arrow points to SiO_2 shell. **(b)** Quantitative analysis of distribution of Fe_3O_4 core sizes in a nanoparticle preparation; histogram shows a fit based on a normalized distribution with a mean of approximately 22 nm. **(c)** Quantitative analysis of core-shell nanoparticle sizes; histogram shows a fit with a normalized distribution with a mean of approximately 73 nm. In panels **(b)** and **(c)**, the y-axis shows counts and the x-axis bin centers represent the size in nanometers. (*Figure reprinted from [140]*)

3.2.2 STXM and Ptychography experiments

X-ray experiments were performed on the Nanosurveyor instrument at BL 5.3.2.1 of the Advanced Light Source [141]. The X-ray energy was fixed at approximately 710 eV, the Fe L-edge. Incident X-rays were focused using a Fresnel zone plate with an outer diameter of 100 nm to give a total coherent flux of ~$5x10^5$ coherent photons s^{-1} at the sample position. An order-sorting aperture was placed slightly upstream of the focal spot to remove all but the first order of the focused beam. To facilitate a full range of rotation without obstructing the order-sorting aperture, grids containing adhered cells and nano-labels were cut into strips thinner than 1mm using a zirconium nitride coated blade prior to transferring them to the Nanosurveyor instrument for X-ray experiments (Fig. 3.3). Thin sample strips allowed a greater range of accessible tilt angles for tomography experiments, which are normally restricted by the approximately 1 mm distance to the order-sorting aperture of the instrument (Fig. 3.3). We acquired a total of 58 STXM projections with a 3 ms exposure and 50 nm step, giving a full field of view of 10x5 μm, with tilt angles ranging between -59° and +40° (Fig. 3.5). Similarly, a total of 22 ptychography datasets, each consisting of 7,500 diffraction patterns, were collected using a compact Fast CCD [142]. Each ptychography pattern was measured with a dwell time of 200 ms and a step size of 60 nm, giving a full field of view of 9 x 3 μm with a pixel size of 5.5 nm (Figs. 3.6 and 3.7).

3.2.3 3D reconstruction of a HeLa cells leading edge by STXM tomography

STXM projections were aligned preliminarily by cross correlation. Background was subtracted from each projection by removing the average value in an empty region of the sample. The projections were normalized to have the same total sum, as the integrated 3D density of the sample should be constant. This tilt series, ac-

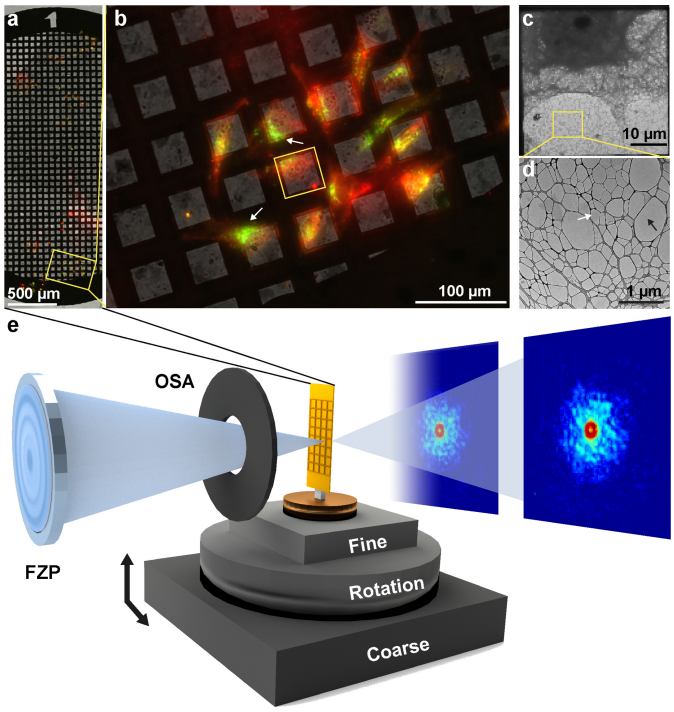

Figure 3.3: Experimental setup for correlative microscopy. **(a)** Composite fluorescent image of HeLa cells grown on graphene-oxide coated lacey carbon TEM grid. Cells were labeled with CMPTX (red) to facilitate tracking and treated with FITC labeled core-shell nanoparticles (green). **(b)** A magnified view of a region from this grid shows cells labeled with a tracking dye as well as fluorescent core-shell nanoparticles. White arrows point to cellular inclusions with clusters of fluorescent nanoparticles. **(c)** Electron micrograph of a portion of a HeLa cell covering an individual grid window, similar to the region highlighted in **(b)**. **(d)** Magnified view of the lacey carbon grid. The black arrow points to empty regions of the grid whilst the white arrow indicates thin layers of graphene-oxide. **(e)** Experimental setup at BL 5.3.2.1 used for STXM/ptychographic imaging with key components labeled. The X-ray beam is focused using a Fresnel zone-plate (FZP) with all but the first order blocked by an order-sorting aperture (OSA). The focused beam is rastered across the sample using high-precision stages under interferometric feedback and diffraction patterns are captured by a fast-CCD at each scan point. (*Figure reprinted from [140]*)

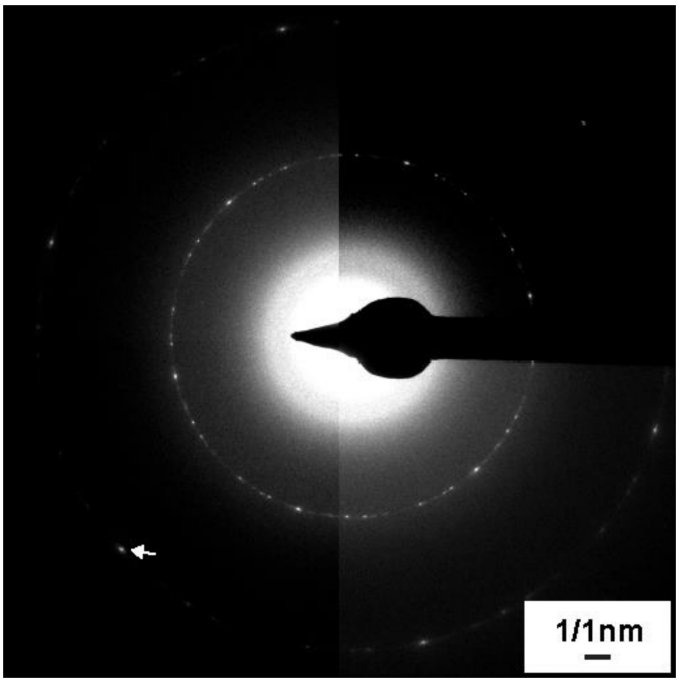

Figure 3.4: Electron diffraction from Au-Lacey graphene oxide grids. White arrows point to reflections produced by individual graphene crystals. The different contrast within the image is due to the differential gain of the 4 tiled detector. (*Figure reprinted from [140]*)

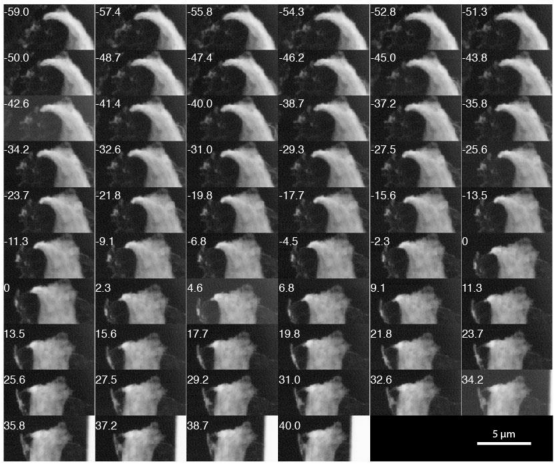

Figure 3.5: STXM tomographic tilt series ranging from -59° to +40° in equal slope increments. (*Figure reprinted from [140]*)

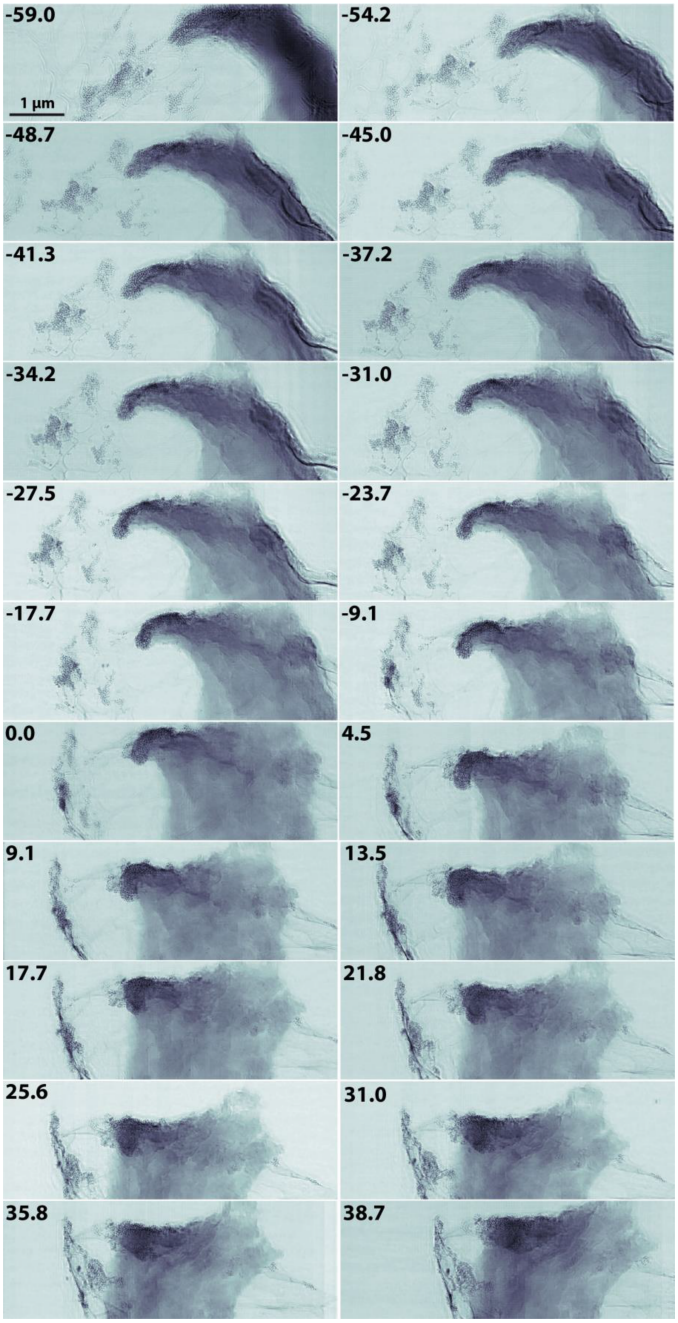

Figure 3.6: Magnitude images of the ptychographic tomography tilt series ranging from -59° to +38.7° in equal slope increments. (*Figure reprinted from [140]*)

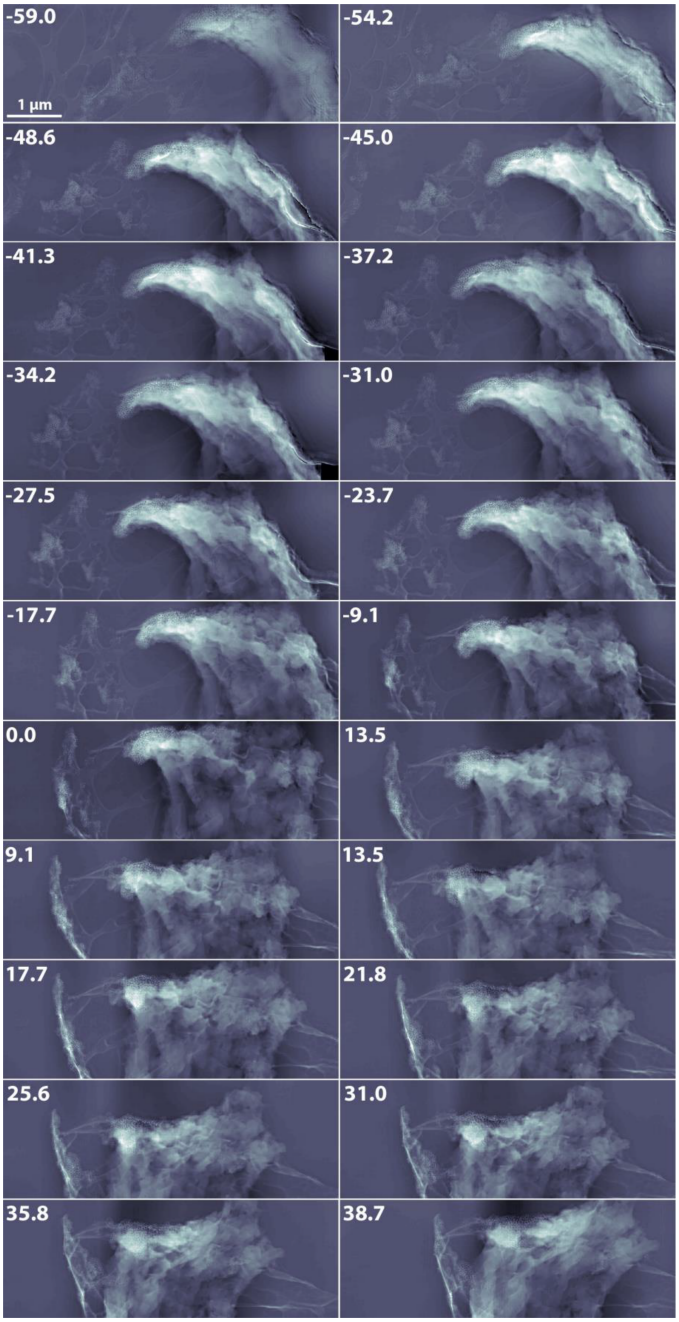

Figure 3.7: Phase images of the ptychographic tomography tilt series ranging from -59° to +38.7° in equal slope increments. (*Figure reprinted from [140]*)

quired from a section of an extended object, imposes a unique challenge for the tomographic reconstruction, as the sample is not isolated. The field of view can drift from one acquisition to the next, but the projection slice theorem, a fundamental assumption of tomographic reconstruction techniques, assumes that the projected density in each image results from the same 3D volume. Therefore, isolating the same density in each projection presents a challenge and was overcome in the following way. The preliminary angular alignment, translational center, cropping, and intensity normalization parameters were used to make an initial set of projections. The tomographic reconstruction was performed using (GENFIRE) [3, 28], originally developed for atomic electron tomography [29]. GENFIRE first pads zeros to each STXM projection and calculates an oversampled Fourier slice. The series of oversampled Fourier slices are interpolated to assemble a 3D Cartesian grid of the Fourier magnitudes and phases. The use of oversampling allows for accurate interpolation of grid points in the neighborhood of each Fourier slice [76], and the remaining Fourier grid points are set as undefined. The algorithm then iterates between reciprocal and real space using the fast Fourier transform (FFT) and its inversion. In reciprocal space, the measured grid points are enforced in each iteration, while undefined points are refined during the iterative process. In real space, the negative values and the electron density outside a pre-defined support are set to zero. An error metric, defined as the difference between the measured and calculated grid points, is used to monitor the convergence of the algorithm. The iterative process is then terminated when the error metric cannot be further reduced. From this preliminary 3D reconstruction, the alignment and cropping of each projection was optimized with another iterative refinement loop. For each experimentally acquired projection, the reconstructed 3D volume was back projected to a range of Euler angles about the current guess and aligned to the experimental projection by normalized cross correlation. The alignment with the maximum cross correlation yields updated values for the orientation and

center of the projection. Next, a mask was made by smoothing and thresholding the best-fitting back projection, and from this mask a new input projection was obtained from the corresponding raw STXM projections. The purpose of this remasking is to correct any inaccuracies in the initial cropping of the raw projections by utilizing the correlated information between the 3D reconstruction and each of its projections. After renormalization of the total intensity, an updated 3D reconstruction was computed from the new projections and orientation parameters. This loop was repeated until convergence of the alignment was obtained after 5 iterations. By using a Fourier based iterative process, GENFIRE produces better 3D reconstructions than other tomographic methods for a limited number of projections (Fig. 3.8). For a detailed comparison between GENFIRE and other 3D reconstruction methods see Chapter 2.

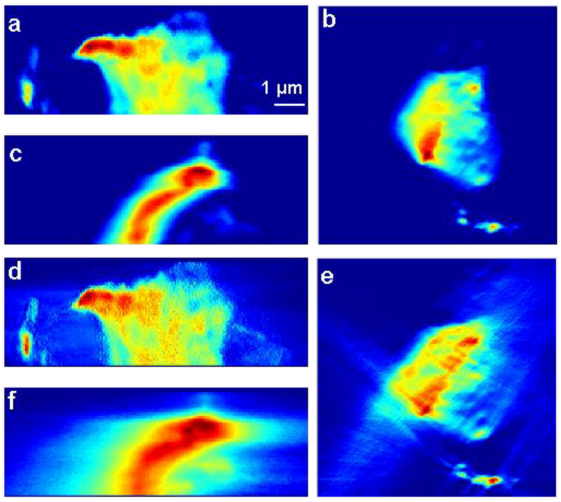

Figure 3.8: Comparison of tomographic reconstruction methods using STXM projections. Three orthogonal projections are shown for GENFIRE in **(a)**, **(b)**, and **(c)**, with corresponding views shown for filtered back projection in **(d)**, **(e)**, and **(f)**. (*Figure reprinted from [140]*)

3.2.4 High-resolution ptychographic reconstruction

To obtain the final ptychographic reconstructions, 7,500 raw diffraction patterns were first corrected for differences in offset and gain among the 192 CCD readout channels using software at BL 5.3.2.1. The corrected patterns were padded with zeros to give an image pixel size that, based on the scan step, would produce an integer number of pixels between scan positions to eliminate rounding errors. The diffraction patterns were then reduced in size by binning to 128 x 128 pixels. To remove bad frames caused by readout errors, the patterns were sorted by integrated intensity and frames with excessively high or low intensity removed. Finally, an intensity-based threshold was applied to the remaining patterns and used to provide an estimate of the incoherent background scattering. This average background was subtracted from the diffraction patterns and spuriously bright pixels were set to zero. Initial ptychographic reconstructions were performed during the experiment using the SHARP algorithm to monitor data quality [143]. Reconstructions were later refined using a strip wise probe relaxation to account for artifacts introduced in some scans by the interaction of the beam with the order-sorting aperture during data acquisition. This relaxation was implemented within a reconstruction scheme based on the extended ptychographic iterative engine (ePIE) [118]. The probe reconstructed via SHARP was used as an initial guess. The probe was updated at each scan position and monitored during the course of the reconstruction. After each macro cycle of ePIE, individual probes were averaged along the axis parallel to the tilt axis. Then a weighted average was performed between strips using a 1D Gaussian kernel to promote communication between different strips and to avoid striping artifacts (Fig. 3.9). For these reconstructions, a strip width of 5 pixels and Gaussian kernel of 1.5 times the strip width gave the best results.

Phase normalization of the reconstructed images is necessary before comparison of neighboring ptychographic projections. A misalignment of the diffraction

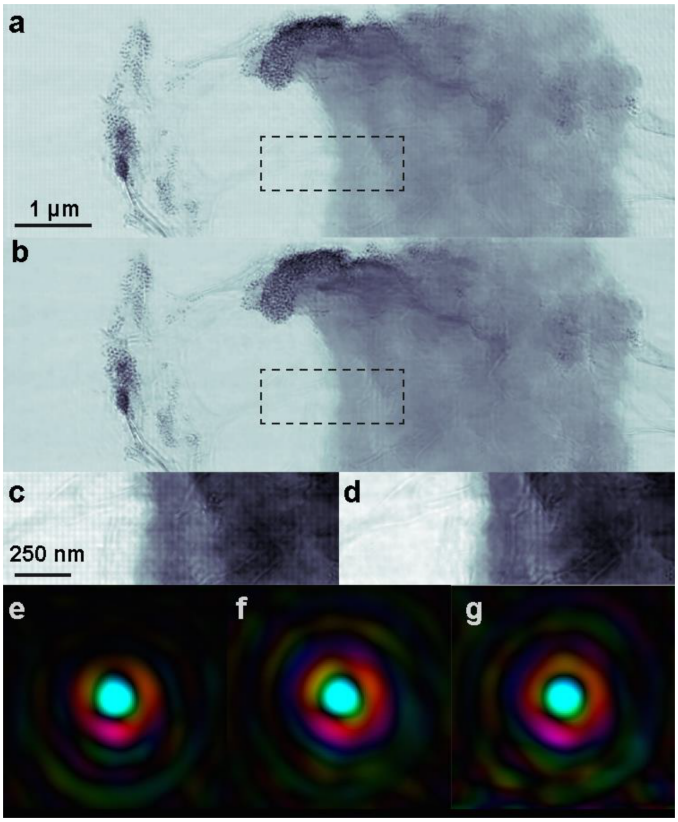

Figure 3.9: Removal of reconstruction artifacts by relaxation of probe uniformity. **(a)** Initial reconstruction with a single probe showing several artifacts due to the regular grid and the OSA interfering with the probe. **(b)** Reconstruction from the same dataset using multiple probes with a strip wise averaging kernel, most of the more obvious artifacts have been removed. **(c)** Zoom in of the region highlighted in **(a)** showing a clear grid pathology. **(d)** Corresponding region from **(b)** showing that the gridding pathology has largely been removed. **(e–g)** Probes from different regions of the reconstruction, Left to right: first strip, middle strip, last strip. (*Figure reprinted from [140]*)

pattern relative to its true center translates to a phase gradient in the reconstruction of the object in real space [144]. Such a gradient can exist in both the horizontal and vertical directions, and an additional constant phase shift can exist without affecting the quality of fit of the reconstruction to the data. To perform this normalization, a pair of empty regions on either side of the sample was selected. A phase gradient in both the x- and y-axes was fit such that the standard deviation in the phase within these two regions was minimized. The constant phase term was then adjusted until the mean phase was zero within these regions.

3.2.5 Correlative cellular imaging using fluorescent microscopy, STXM tomography and ptychography

We achieved high-resolution imaging of the leading edge of a HeLa cell treated with fluorescent core-shell Fe_3O_4-SiO_2 nanoparticles by correlative microscopy. Fig. 3.10a shows part of an individual cell containing fluorescent nanoparticles. This same region was imaged using a coarse STXM scan to identify a smaller region of interest (Fig. 3.10b). A fine STXM scan was then performed on the region of interest and a tilt series of 58 STXM projections were acquired from this region. These projections were reconstructed to produce a 3D volume using GENFIRE, shown in Figs. 3.11 a, b and c. A small section of the leading edge of the HeLa cell was reconstructed in its entirety. Several regions within the reconstructed 3D volume show high absorption. We attribute this high absorption to the concentrated uptake of nanoparticles into the cell.

The resolution of our 3D reconstruction is sufficient to observe membrane ruffles near the upper leading edge of the cell (Fig. 3.11a). Due to obstruction of our sample by the TEM grid bars during rotation, our data suffers from a large missing wedge of more than 80°. Despite this, features in our reconstruction of the sample along the missing wedge direction are still well defined, allowing for precise 3D localization of the nanoparticles. Traditional tomographic reconstruc-

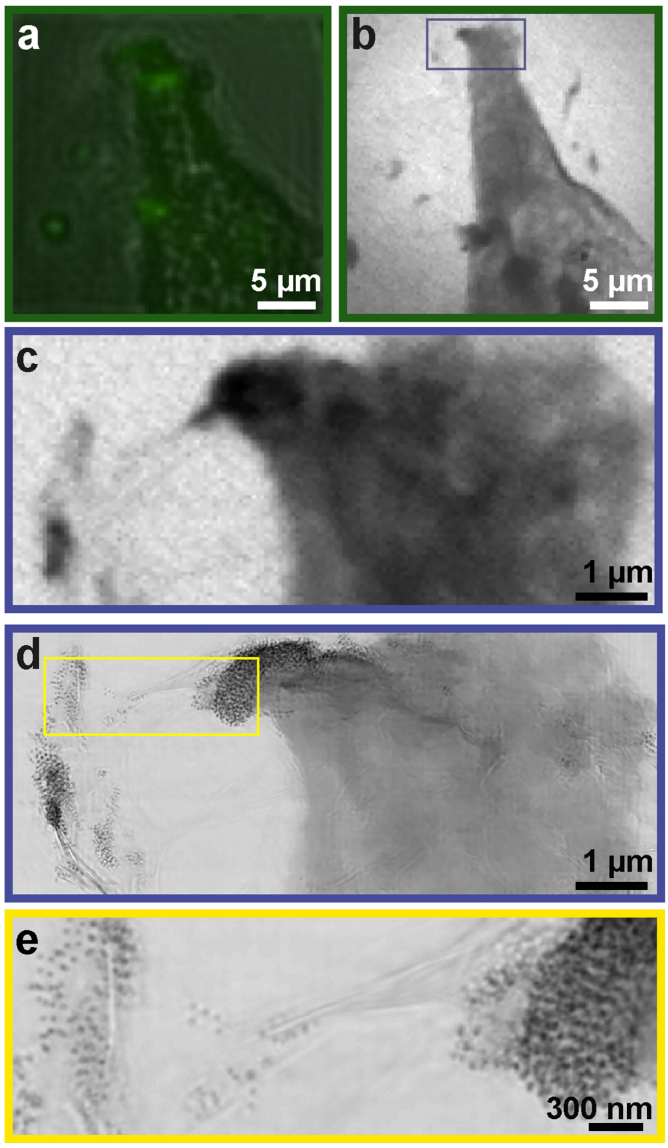

Figure 3.10: Localization of functionalized nanoparticles in a cellular context with correlative microscopy. **(a)** Part of a HeLa cell containing functionalized nanoparticles was first identified using fluorescent microscopy. **(b)** The same region imaged using a coarse STXM scan. **(c)** A fine STXM scan was then performed on a region of interest and a tomographic tilt series was acquired from this region. **(d)** Ptychographic imaging of the same region as **(c)** to obtain a higher resolution information. **(e)** Individual nanoparticles within and around the leading edge of the cell identified by the ptychographic reconstruction. (*Figure reprinted from [140]*)

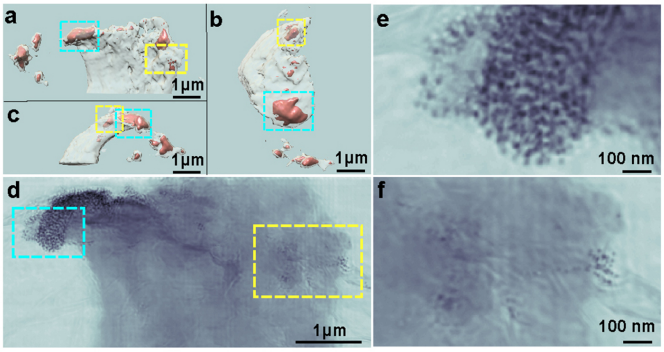

Figure 3.11: STXM tomography reconstruction of the leading edge of a HeLa cell. **(a–c)** Iso-renderings of the 3D reconstruction showing several high-density regions (orange) within the cell, viewed along the z-, minus y- and x-axes, respectively. **(d)** High-resolution ptychographic image confirming that the internalized high-density regions correspond to uptaken nanoparticles by the cell. **(e, f)** Magnified views of two regions in **(d)** labeled with cyan and yellow rectangles, respectively. (*Figure reprinted from [140]*)

tion techniques, such as filtered back projection, suffer greatly from elongation artifacts when viewed along angles corresponding to unmeasured projections due to the anisotropic resolution of reciprocal space along this direction (Fig. 3.8). The clarity of our results is attributed to our reconstruction algorithm, GENFIRE, which produces quality tomographic reconstruction from a limited number of measured projections. In this particular example, views along the missing wedge provide extended context that is critical for drawing biologically relevant conclusions regarding particle internalization.

To reveal the local distribution of fluorescent Fe_3O_4-SiO_2 nanolabels in or near the HeLa cell, we performed 2D ptychographic CDI on regions of interest identified from the 3D reconstruction using STXM tomography (Fig. 3.11a, b and c). Our ptychographic scans produced high-resolution images that allow visualization of individual nanolabels in a correlative manner (Fig. 3.11 d, e and f). The images also show, with high contrast, fine features such as membrane ruffles,

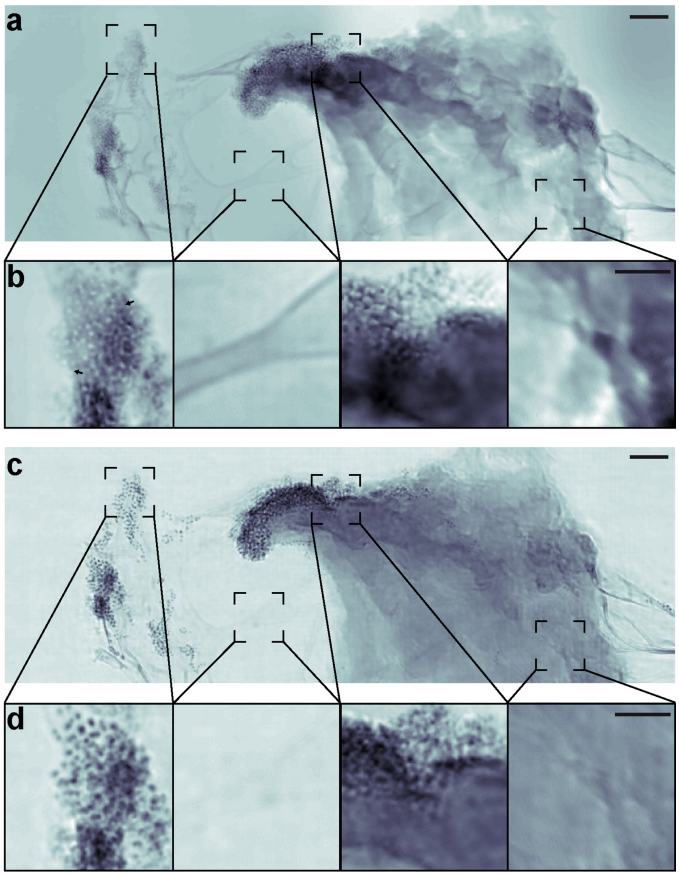

Figure 3.12: Phase and magnitude ptychographic images of cellular structure with functionalized nanoparticles. **(a)** Phase image of the ptychographic reconstruction of a HeLa cell labeled with core-shell nanoparticles showing high contrast for cellular features such as membrane ruffles and fillipodia. **(b)** Magnified views of the regions outlined by dashed boxes in **(a)**, including (left to right) nanoparticles alone, graphene-oxide coated lacey carbon, cell and nanoparticles, and cell alone. The magnified view of the nanoparticles also demonstrates the phases ability to discern the silica shell (light gray halo around cores indicated by black arrows) as well as the two different oxidation states (light and dark cores). A larger version of this can be seen in Fig. 3.17. **(c)** Magnitude image of the ptychographic reconstruction showing high contrast for the Fe_3O_4 cores of the nanoparticles. **(d)** Magnified views of the same regions shown in **(b)**, highlighting the different features that can be sharply resolved between the phase and magnitude images. Scale bars represent 500 nm (**a** and **c**) and 200 nm (**b** and **d**). (*Figure reprinted from [140]*)

filopodia, and the thin lacey carbon support (Fig. 3.12). The enhanced contrast in these images is facilitated by the transparency of the grapheneoxide substrate and the presence of Fe_3O_4-SiO_2 nanolabels. The scattering signal produced by regions of cellular material containing these nanolabels is stronger than that produced by cellular material alone. The total scattered intensity in the presence of nanolabels increases by almost an order of magnitude compared to cellular material alone or the substrate (Fig. 3.14). This increased image contrast and resolution facilitates localization of the nanolabels even when embedded within the cell. Fig. 3.12 shows the phase and magnitude of the high-resolution ptychographic images. The phase images show fine cellular features such as membrane ruffles [145] and filopodia [146] (Fig. 3.12a and b), while the magnitude images exhibit high contrast for the fluorescent Fe_3O_4-SiO_2 nanolabels. Further cellular detail, such as cytoskeletal components, are however obscured due to the limited resolution and poor contrast of subcellular structures in a background of other cellular components in 2D projection. This combination of the phase and magnitude images allows us to determine the accurate localization of the nanolabels near the cell periphery of, and inside the HeLa cell.

By imaging close to an absorption edge, we also made possible the distinction of multiple oxidation states based upon recovered phase and absorption contrast of the nanoparticles. Our magnitude images allow the precise localization of the core-shell nanoparticles (Fig. 3.12c and d). The phases of our ptychographic reconstructions show the presence of nanoparticle cores in two possible states, indicating potential differences due to oxidation (Fig. 3.12b and Fig. 3.13). This remains consistent across projections and is not an artifact of reconstruction (Fig. 3.15). Particles in the Fe^{3+} state, with an absorption resonance at 710 eV, will present zero phase shift relative to vacuum because of the value of the real part of the refractive index at the absorption resonance. Thus, those particles appear to have an annular structure in the phase images, which highlight the presence of the silica

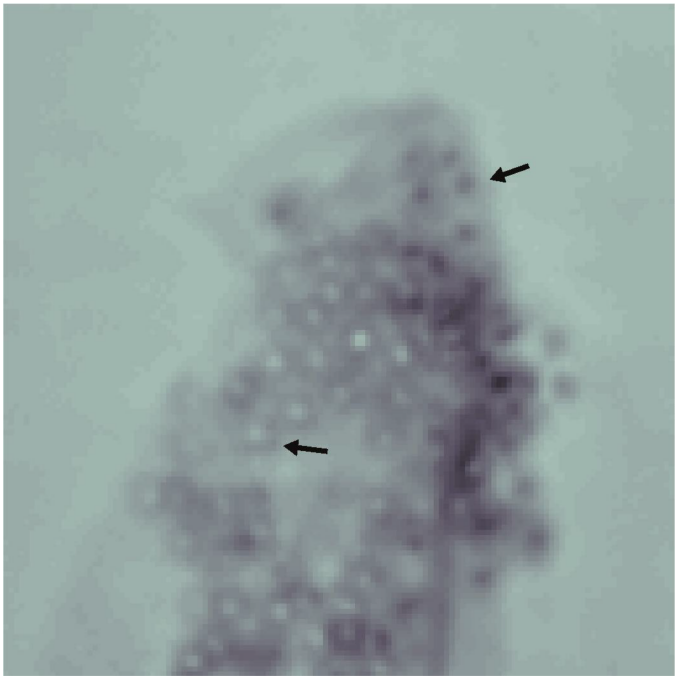

Figure 3.13: Magnified view of nanoparticles from the phase of the ptychographic reconstruction. The two different oxidation states of nanoparticles (light and dark) are indicated by black arrows. The silica shell of the nanoparticles is also visible as a light grey annulus. (*Figure reprinted from [140]*)

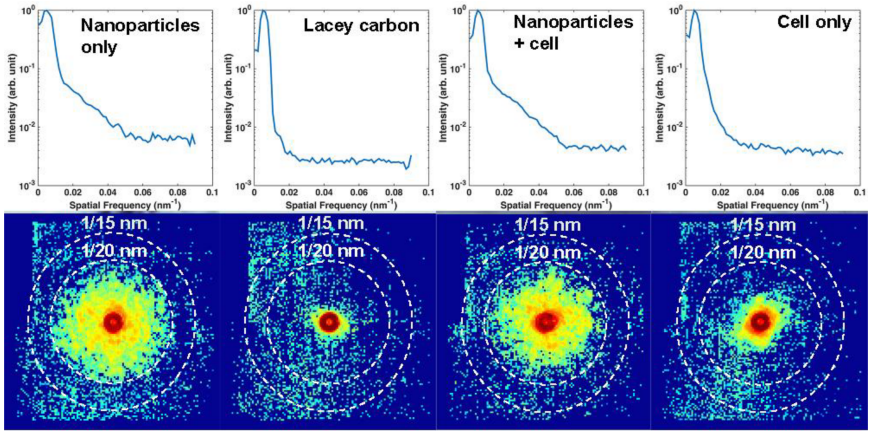

Figure 3.14: Increase in scattering power in regions containing nanoparticles. Radial average profiles (top) and diffraction patterns (bottom) corresponding to the zoomed in regions shown in Fig. 3.12 demonstrating an increase in scattered photons at higher spatial frequency in the presence of nanoparticles. (*Figure reprinted from [140]*)

shell having non-zero phase shift. Although the initial step of the nanoparticle synthesis a single iron oxide is expected (Fe_3O_4). During the course of the storage at room temperature and in an aqueous medium, a subset of nanoparticles may naturally oxidize from Fe_3O_4 to Fe_2O_3 [147]. The iron-oxide nanoparticles then exist as a mixture of these two oxides, each with distinct oxidative states and, consequently, distinct absorption coefficients at the Xray energies used in this experiment. This difference in the scattering properties of our iron-oxide nanolabels is evident in the phase images (Fig. 3.12b and Fig. 3.13). While we did not focus on a spectroscopic analysis and did not image over a range of probe energies required to quantitatively measure the iron X-ray absorption coefficient of each species, our correlative technique is in principle capable of spectroscopic studies, allowing discernment of chemical species for a given nanoparticle in a cellular context.

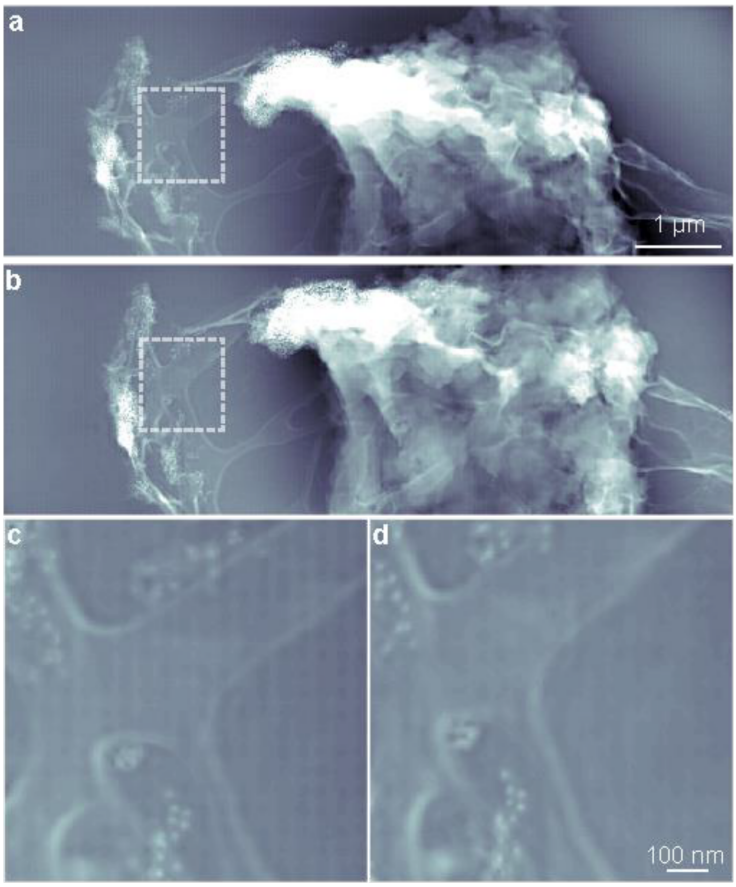

Figure 3.15: Consistency of nanoparticle phase contrast across projections. Comparison of nanoparticles phase contrast between **(a)** -9.1° projections and **(b)** 0° projection. Corresponding zoomed regions are shown in **(c)** and **(d)**, demonstrating that the phase contrast is consistent for each particle across multiple projections. (*Figure reprinted from [140]*)

3.2.6 Resolution estimation

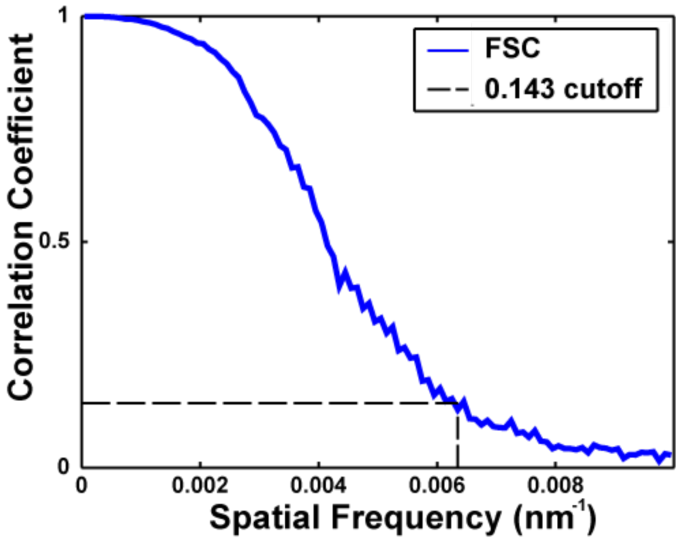

Figure 3.16: Fourier Shell Correlation calculated from reconstructions of two half sets of the STXM tomography data. The dashed line indicates a resolution of 157 nm. (*Figure reprinted from [140]*)

To estimate the 3D resolution in STXM tomography, we compared independent reconstructions performed on two separate halves of the tilt-series. The Fourier shell correlation (FSC) between the two reconstructions is an approach commonly used in single-particle cryo-electron microscopy to estimate the 3D resolution [148]. Based on the criterion of FSC = 0.143, we determined the 3D resolution of the STXM tomography reconstruction to be 157 nm (Fig. 3.16). Next, we estimated the resolution of our ptychographic reconstructions in two ways. First, we calculated the average phase retrieval transfer function (PRTF) for all of the patterns in a particular scan [149]. This gave us an upper and lower bound of the resolution as being between 25 and 15.5 nm in the full period based on a threshold of 0.5 (Fig. 3.17). Second, we performed line scans across individual nanoparticles, which are well resolved and of known size (~73 nm with ~22 nm core). Line scans across the nanoparticle cores show that spacing of 3

pixels or greater can be easily distinguished, from which we estimate a resolution of ~16.5 nm in the full period (Fig. 3.17). Taking both of these into account, we estimated the overall resolution in our images to be approximately 16.5 nm in the full period.

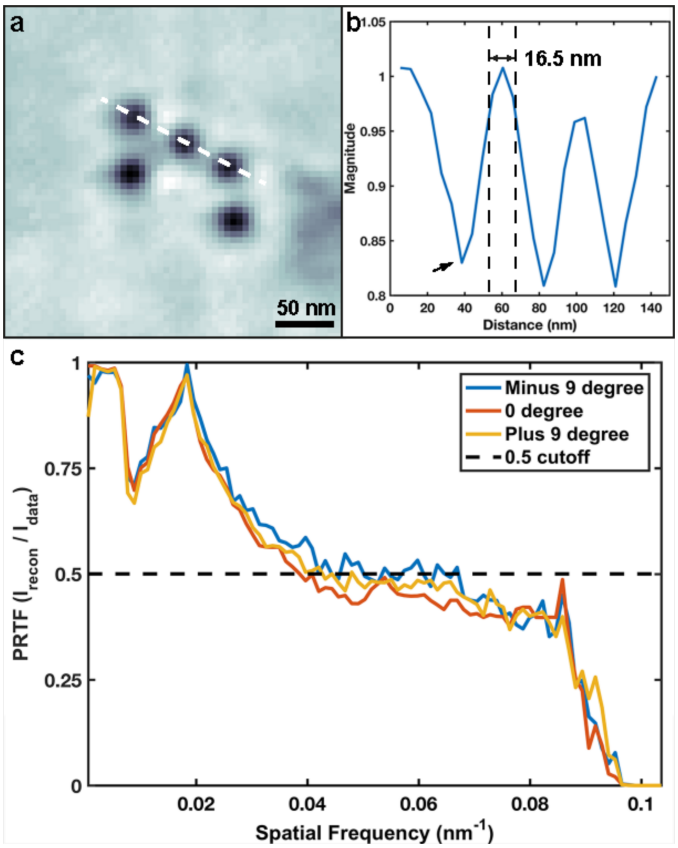

Figure 3.17: Resolution estimates of ptychography reconstructions. **(a)** Zoom in of a region with well isolated iron oxide cores from the magnitude image of the -9.1° ptychography projection. **(b)** Line scan across the dashed white line in **(a)** showing clearly resolved edge-to-edge separation of 16.5 nm between individual nanoparticle cores. The black arrow indicates the center of the first core in (a). **(c)** Average phase retrieval transfer function (PRTF) calculated from all 7500 patterns in each dataset for the three principle projections used for further analysis. The cut-off at 0.5 shows that the resolution of the whole images lies somewhere between 25 nm and 15 nm. (*Figure reprinted from [140]*)

3.2.7 Radiation dose and damage

Radiation dose is fundamentally limiting to high resolution imaging experiments. Our current experiment does not benefit from the advantage of cryo-protection and therefore directly suffers from the imparted X-ray dose at 710 eV. We limited the total dose on the sample by first obtaining low-dose STXM images of the sample. Each STXM projection imparts an estimated dose of only 25 Gy, with a full tomogram imparting a dose of $1.45x10^3$ Gy; this is well within the tolerable limit for our desired resolution in 3D [39]. A single ptychography scan imparted a dose of $1.17x10^3$ Gy per projection on the sample, similar to the total dose for the STXM tomography dataset. For this reason, while a full ptychographic tomography series was captured, we limited our analysis to a subset of measured projections suspecting that the high dose could lead to changes in sample morphology during the course of the tomography series. The zero degree projections taken before and after the ptychographic tomography series confirm these changes. In contrast, the appearance and localization of nanoparticles, which are more tolerant to dose, remains unchanged (Fig. 3.18). Since the total dose imparted to this cell is within the tolerable limit for cryogenically frozen samples [19], we believe that cryo-preservation alone will facilitate similarly high-resolution results in 3D. Furthermore, cryo-preservation will alleviate some of the issues related to interpreting cellular ultra-structure as the cells will be preserved in a more natural state. The combination of higher-resolution and more faithful preservation of cellular material will significantly benefit this imaging method.

3.2.8 Synthesis and characterization of fluorescent Fe_3O_4-SiO_2 core-shell nanoparticles

The Nanoparticles (NPs) synthesis protocol was adapted from the literature [150, 151] to generate fluorescent Fe_3O_4-SiO_2 NPs as follows. A mixture of hydrated

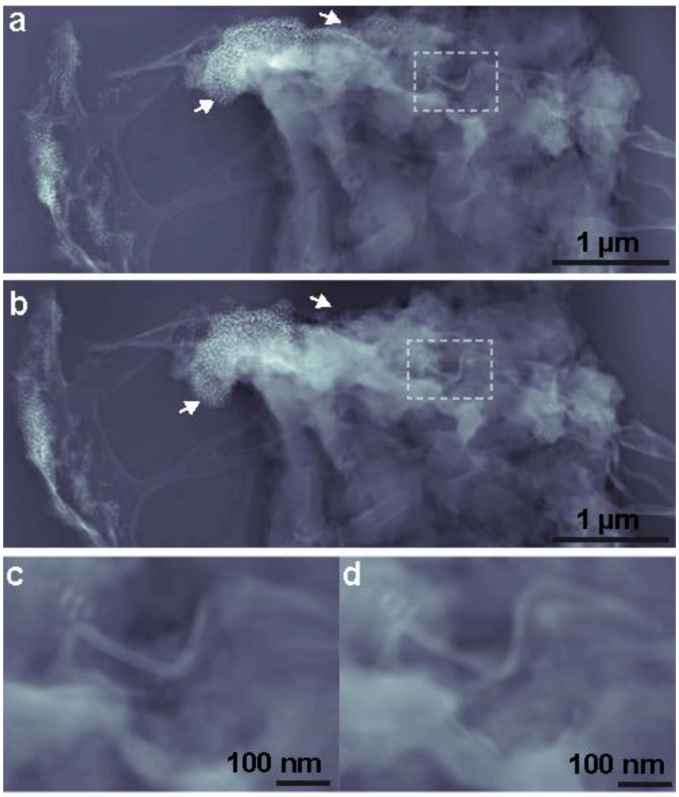

Figure 3.18: Comparison of the 0° projection before and after tomography series acquisition. **(a)** Phase image of the zero degree projection before tomography. **(b)** Phase image of the zero degree projection after tomography. The two images show clear differences (highlighted by white arrows) mostly relating to an overall loss of mass of the cell due to radiation damage. **(c)** and **(d)** Zoom in of the highlighted region in **(a)** and **(b)** respectively demonstrating that fine features and nanoparticles remain largely unchanged during the full exposure time. (*Figure reprinted from [140]*)

iron oxide (FeO(OH), 0.181 g), oleic acid (3.180 g) and docosane (5.016 g) was prepared in a round flask and stirred under vacuum for 1 h. This mixture was refluxed at 350°C for 2 h in argon atmosphere. After cooling to room temperature, the resulting black solid was dissolved in pentane, mixed with an ether:ethanol solution (2:1) and centrifuged. The decomposed organic black solution was removed and the Fe_3O_4 nanoparticles were re-dispersed in pentane and washed with the ether:ethanol solution. After centrifugation, the NPs were stabilized with oleylamine (200 μL) and dispersed in chloroform. Then, 1.75 mL of 2 M NaOH solution was added into 200 mL of a CTAB solution (25 g.L-1) and this mixture was kept at room temperature for 1 h under constant stirring. This mixture was heated up to 75 °C and 7.5 mL of Fe_3O_4 NPs chloroform suspension was slowly added into the CTAB basic aqueous solution under vigorous stirring. The formation of an oil-in-water microemulsion resulted in a turbid brown solution. The resulting solution was vigorously stirred for 2 h at 75 °C resulting in a transparent black Fe_3O_4/CTAB suspension. Then, 5 mL of tetraethylorthosilicate (TEOS) and 5 mL of FTIC-APTES (10 mg of fluorescein isothiocynanate [FITC] was reacted with 250 μL of 3- aminopropyltriethoxysilane [APTES] in 10 mL of ethanol for 2 h) were added to the Fe_3O_4/CTAB suspension and stirred for 3 h at 75 °C to obtain the fluorescent Fe_3O_4-SiO_2 NPs. These nanoparticles were washed 3 times with ethanol to remove the unreacted species and then dispersed in 20 mL of ethanol. The remaining sample was refluxed twice with an alcoholic solution of ammonium nitrate (6 g.L-1, NH_4NO_3) at 50°C to remove CTAB from the NPs pores. After washing them twice with ethanol, the fluorescent Fe_3O_4-SiO_2 NPs were dried under airflow for a few hours. All chemicals used along this protocol were purchased from Sigma-Aldrich. The morphology of the nanoparticles was investigated on a JEM 2100 JEOL transmission electron microscope. The samples were prepared by dropping a few drops of a highly diluted ethanolic nanoparticle suspension on regular TEM grids. The corresponding particle size distribution

was obtained by measuring the core and the nanoparticle diameters of more than 400 particles.

3.2.9 Preparation of graphene-oxide coated lacey carbon TEM grids

All the biological assays were performed on a substrate composed of a Gold 400 Mesh TEM grid with lacey carbon. Additionally, a graphene layer was deposited on top of the lacey carbon to allow the culture of adherent cells on the TEM grid. The graphene layer was created by deposition of graphene oxide on the TEM grid by the drop-casting method. A solution composed of 50% ethanol in double distilled water containing graphene oxide sheets is dropped on top of the TEM grid. After drying, TEM grids were annealed at 150° C for 30 min creating a homogeneous surface. This process also guarantees sterilization of the TEM grid. The prepared TEM grid was submerged in Dulbeccos modified Eagles medium (DMEM) supplemented with 10% fetal calf serum and placed on the bottom of a cell culture dish. Next, suspended HeLa cells are dropped on the solution and maintained at 37° C in a 5% CO_2 atmosphere

3.2.10 Nanoparticle treatment

The HeLa cells that had adhered to the graphene TEM grid were treated with the core-shell nanoparticles. The nanoparticles were suspended in distilled water (100μg/ml), and a few drops were added to the solution and dispersed gently. Cells were exposed to nanoparticles for 30 min, the medium was removed and the cells were gently washed with medium. Finally, the cells were fixed with paraformaldehyde.

3.3 Discussion

The power of correlative microscopy lies in its potential to bridge the gap between complementary techniques, possibly expanding where a given method may be limited. Ptychographic CDI can provide high contrast images with a spatial resolution in the tens of nanometers from relatively thick, extended cells, particularly in the soft X-ray regime. As such, it is well suited to image in the regime between visible light and electron microscopy and its incorporation into correlative schemes is an area of active research [112, 113, 127, 152]. However, biological specimens are a challenge to image with high resolution due to their sensitivity to radiation. This sensitivity imposes strict limits on 3D imaging of cells, given the high dose required to obtain multiple projections of a single cell. STXM tomography complements ptychographic imaging, providing an opportunity to image a radiation sensitive sample in 3D with a lower dose than a single ptychography scan. In doing so, STXM tomography provides an overview of a large sample region or an entire cell in 3D prior to high-resolution ptychographic imaging. In the ideal correlative experiment, a labeled sample could be initially inspected by fluorescence microscopy to identify temporal and spatial regions of interest. Then, a STXM tilt series would provide an overview of the whole cell in 3D. Next, high-resolution ptychographic imaging would provide near molecular details that could be correlated with known cellular structures. Finally, electron microscopy could be used to provide true molecular detail. The present revolution in imaging methods across the length scales will continue to benefit such correlative approaches. In summary, we demonstrate a proof-of-principle correlative imaging method across multiple length scales of mammalian cells treated with functionalized fluorescent nanoparticles. Using a HeLa cell as a model system, we first identify cellular features of interest by fluorescent microscopy and correlate them in 3D via STXM tomography. We then image sub-regions of interest by ptychographic CDI with a resolution of ~16.5 nm. We observe fine biological features such as membrane

ruffles and filopodia, and accurately localize individual fluorescent nanoparticles near the cell periphery and inside the cell. By choosing X-ray energies near the Fe L-edge, we enhance the image contrast of the coreshell Fe_3O_4-SiO_2 nanoparticles and identify them in two oxidation states. The ability to detect different oxidation states is important when the magnetic properties of the nanoparticles play a critical role in their function, such as magnetically induced heating of Fe_3O_4 nanoparticles in cancer therapy [99]. Although the nanoparticles were not targeted to specific biological structures in this study, incorporation of targeting moieties onto these nanoparticles is feasible and remains under investigation [153,154]. By incorporating cryogenic techniques, the applicability and resolution of this method can be further improved by removing the need for extensive fixation protocols [39]. Higher resolution would allow the visualization of subcellular organelles with much greater detail, such that the interaction between nanoparticles and organelles can be better understood. The ability to perform correlative cellular imaging and localize individual nanoparticles inside intact, unsectioned mammalian cells through a combination of fluorescent microscopy, STXM tomography and ptychography will not only yield a more comprehensive understanding of the cell as a complex biological system, but also find applications in quantifying cellparticle interactions in nanomedicine.

CHAPTER 4

Correlative 3D X-ray fluorescence and ptychographic tomography of un-labeled frozen hydrated green algae

Accurate knowledge of elemental distributions within biological organisms is critical for understanding their cellular role. The ability to couple this knowledge with overall cellular architecture in three-dimensional space deepens our mechanistic understanding of cellular chemistry. Using an unsectioned, frozen-hydrated *Chlamydomonas reinhardtii* cell as a model system, we report a new development in three-dimensional correlative microscopy using cryogenic X-ray ptychography and X-ray fluorescence microscopy. In combination with our recently developed tomographic reconstruction algorithm (GENFIRE) we produce high quality tomograms of the unlabeled alga's cellular ultrastructure, alongside three-dimensional distribution maps of key elements within the cell collected simultaneously. We demonstrate GENFIRE's ability to outperform conventional tomography algorithms and also the improvements in reconstruction quality arising from GENFIRE's ability to self-correct inaccuracies in recorded experimental tomography angles. We believe this application of correlative X-ray tomography will provide biologists with a new tool to probe a myriad of biological specimen that can provide new insights.

4.1 Introduction

Imaging biological material in a native or near-native state is of fundamental importance to modern high-resolution microscopy. Super resolution fluorescence microscopy, for which the 2014 Nobel prize in Chemistry was awarded, allows for the real-time imaging of cellular process at sub-wavelength resolutions [155, 156]. Cryo-electron tomography (cryo-ET) in combination with Focused Ion Beam (FIB) milling now offers exquisite windows inside of cells, resolving organelles and even individual protein complexes without the need for additional staining [157]. However, these techniques are not without limitations. The need for fluorescent labels potentially removes the cellular context of observed events and, the penetration depth of electrons through soft matter limits cryo-ET to either small cells or thin sections. Circumventing these difficulties require the use of additional techniques. One promising approach currently under development is coherent diffraction imaging [64,70] (CDI). CDI requires the collection of oversampled diffraction patterns from noncrystalline samples using bright coherent photons from sources including synchrotron radiation [10,67,119,127,140,158–160], high harmonic generation [104,161,162] and X-ray free electron lasers [107,124,163–165]. These patterns are then computationally inverted to produce an image using iterative phase retrieval algorithms such as hybrid input output [166] or oversampling smoothness [167]. Where hard X-rays are used as the illumination source, CDI permits imaging of thick biological samples without chemical labeling, due to their high penetration depth and natural contrast due to electron density. Ptychography, a scanning variant of CDI, has proven a powerful method for imaging a wide range of organic and inorganic materials such as whole cells, bone and integrated circuits in 2D and 3D [68, 119, 127, 129, 140]. A significant advantage of ptychography is that it does not require the sample to be isolated, and fields-of-view of more than 100 μm^2 can be achieved while maintaining resolution below 20nm [140]. Due to their short wavelength, hard X-rays also have the ability to stimulate X-ray

fluorescence from many different elements. This is exploited in X-ray fluorescence microscopy (XFM) to quantitatively map the distribution of trace elements within cells [168–170]. Both ptychography and XFM provide different but complementary information regarding the specimen of interest, and when combined they can offer deeper insights into relationship between structure and function in biological organisms.

Previously simultaneous ptychography and XFM has been achieved in 2D [127, 160], but its 3D extension has not been demonstrated. In this work, we demonstrate this correlative 3D imaging method on unlabeled frozen-hydrated green algae (Fig. 4.1 summarizes the experiment). The tomographic reconstructions were performed using using GENFIRE to reconstruct an intact, cryogenically preserved *Chlamydomonas reinhardtii* alga cell acquired using ptychography and XFM. Using ptychographic tomography we have mapped the three-dimensional cellular location of polyphosphate bodies and the pyrenoid inside the alga and then confirmed the identity of these structures using 3D elemental distribution maps recorded by XFM.

4.2 Results

4.2.1 GENFIRE Reconstructions

Fig. 4.2a, b and Fig. 4.2c, d show GENFIRE 3D XFM and ptychography phase-contrast reconstructions, respectively. The P and Ca XFM volumes are in excellent agreement with each other [172], and 3D mappings show distribution of the polyphosphate bodies along the cell wall in the lower half of the alga. Opposite the polyphosphate bodies, the S volume indicates localization of the pyrenoid due to high local concentration of the enzyme RuBisCo inside the organelle surrounded by a low-density area that is indicative of the starch sheath. The Cl concentration is primarily at the periphery, while the K volume shows clear K localization

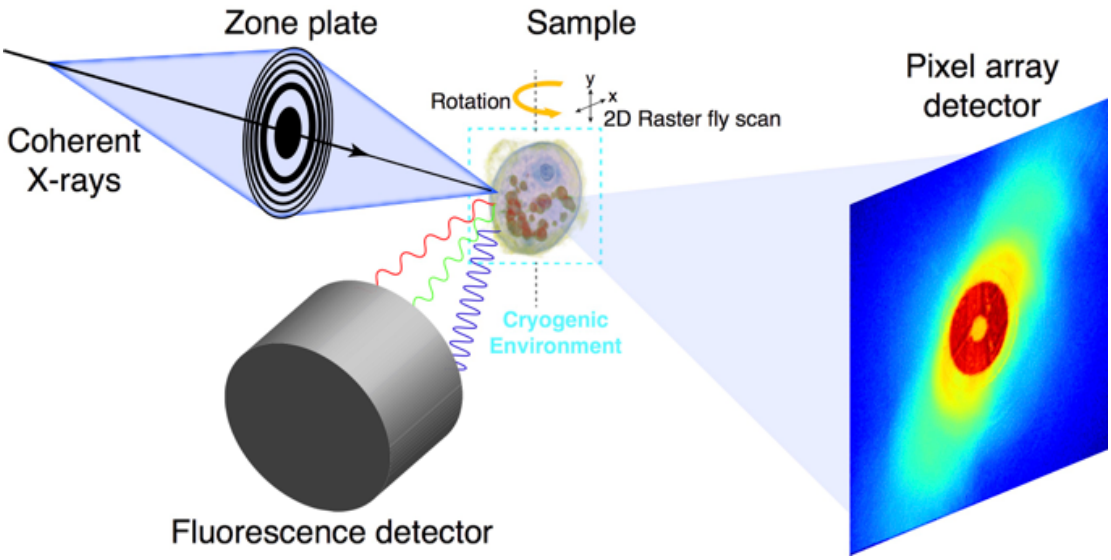

Figure 4.1: Experimental schematics for simultaneous X-ray fluorescence and ptychography measurements. A coherent monochromatic X-ray beam was focused by a Fresnel zone plate into a small focal spot on the sample. The sample preserved in the cryogenic environment was raster fly-scanned in the x-y plane. During the scan fluorescence signals and diffraction patterns were simultaneously recorded by a fluorescence detector and a pixel array detector, respectively. After finishing a 2D scan, the sample was rotated to a new angle until completing the whole 3D scan. (*Figure reprinted from [171]*)

within the alga, suggesting the cell is well-preserved during the freezing process. The ptychography phase-contrast reconstruction shows similar localization of the pyrenoid and polyphosphate bodies inside the cell. During data acquisition, the focused X-ray beam was allowed to dwell on one spot of the cell for an extended amount of time at the 0° position as the shutter was unintentionally left open, which resulted in a burnt hole through areas of the cell. This burnt hole can be seen in the 7th slab in Fig. 4.2c as a ~0.6 μm wide and ~2.2 μm long void near the polyphosphate bodies within the cell.

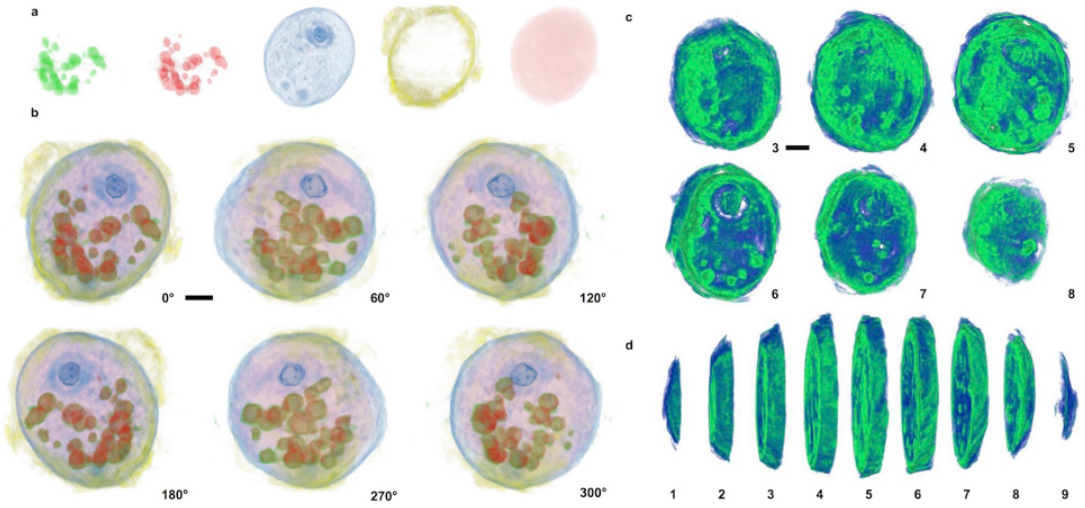

Figure 4.2: GENFIRE X-ray fluorescence and ptychography tomography reconstructions. **(a)** Zero-degree projection of reconstructed volume of P, Ca, S, Cl and K channels, respectively. **(b)** rotated view of the composite reconstructed volume, 60° apart in each image, showing clear localization of pyrenoid (S channel) near the top and polyphosphate bodies near the bottom (P and Ca channels). Scale bar 4 μm. **(c)** slabs of ~2 μm thickness through the ptychography tomographic volume, showing various organelles and a damaged spot in slab 7 due to overexposure. Scale bar 4 μm. **(d)** cut outs of the entire reconstructed volume viewed along the 80° direction. (*Figure reprinted from [171]*)

4.2.2 Comparison of GENFIRE with Other 3D Reconstruction Algorithms

When the number of projections is limited, due to either the missing wedge problem at high tilt or the threshold on imparted dose before radiation damage, GENFIRE produces better 3D reconstructions than other conventional tomographic methods such as filtered back projection (FBP) [3, 28]. Fig. 4.3a-e show the projections of FBP reconstructed volumes along the missing wedge direction for ptychography, P, S, Ca and K channels, respectively, and Fig. 4.3f-j show the same projection for GENFIRE reconstructed volumes. GENFIRE's Fourier-based approach provides a better recovery of missing data and more detailed information on cellular ultrastructure in all cases. For a more detailed comparison and analysis of GENFIRE with other tomographic reconstruction algorithms, see Chapter 2.

4.2.3 Angular Refinement

Prior to alignment, unprocessed projection images showed noticeable out-of-plane rotation and drift from tilt axis due to imperfect motor stage movement. Inaccuracies in projection alignment in any direction will result in lower reconstruction resolution. In extreme cases, this may lead to misinterpretation of reconstruction artifacts in the cell as true cellular features. To algorithmically correct this experimental error in projection tilt angles, an angular refinement procedure was incorporated into the GENFIRE tomographic reconstruction workflow [28]. Because X-ray fluorescence and ptychography data were acquired simultaneously in this work, the P channel projections were used for initial angular refinement as they had the best signal-to-noise ratio, and the resulting updated angles were used for all other reconstructions. Angular deviations were found to be between 2° in and (i.e. out-of-plane of rotation) and 1.5° along the rotation axis (Fig. 4.3k). Fig. 4.3l shows noticeable improvement in reconstruction quality after angular re-

finement. The blue and green solid volumes represent the reconstructions before and after angular refinement, respectively. Individual polyphosphate bodies in close proximity are better differentiated and isolated after refinement.

4.2.4 Estimation of 3D resolution

We quantified the 3D resolution of the reconstructions by plotting the density variations across a polyphosphate body in 3 axial directions (Fig. 4.4a, b) and (2) 3D power spectrum analysis (Fig. 4.4c). Both analyses indicate a half-period resolution of ~125 nm along the x and y axes and ~140 nm along the z direction for 3D fluorescence reconstruction, and 3D ptychography reconstruction has a half-period resolution of ~45 nm along the x and y axes and ~55 nm along the z direction. The decrease in resolution along z direction is expected due to the sparsity of data along this direction, i.e. the missing-wedge effect.

4.3 Discussion

4.3.1 Correlative imaging identifies cellular ultrastructure in 3D without chemical labeling

Simultaneous tomography of X-ray fluorescence and ptychography provide complementary structural information about the cell. In this experiment, phase imaging via X-ray ptychography provided a high resolution 3D map of *C. reinhardtii's* ultrastructure with contrast dictated by its electron density, highlighted distribution of polyphosphate bodies and pyrenoid in the cell, and even localized the small cellular volume that is affected by beam-induced radiation damage. In a complementary fashion, XFM confirms the identity of P-rich polyphosphate bodies and pyrenoid based on the distribution of specific trace elements within them. Importantly, all this mapping and identification is realized without sectioning and

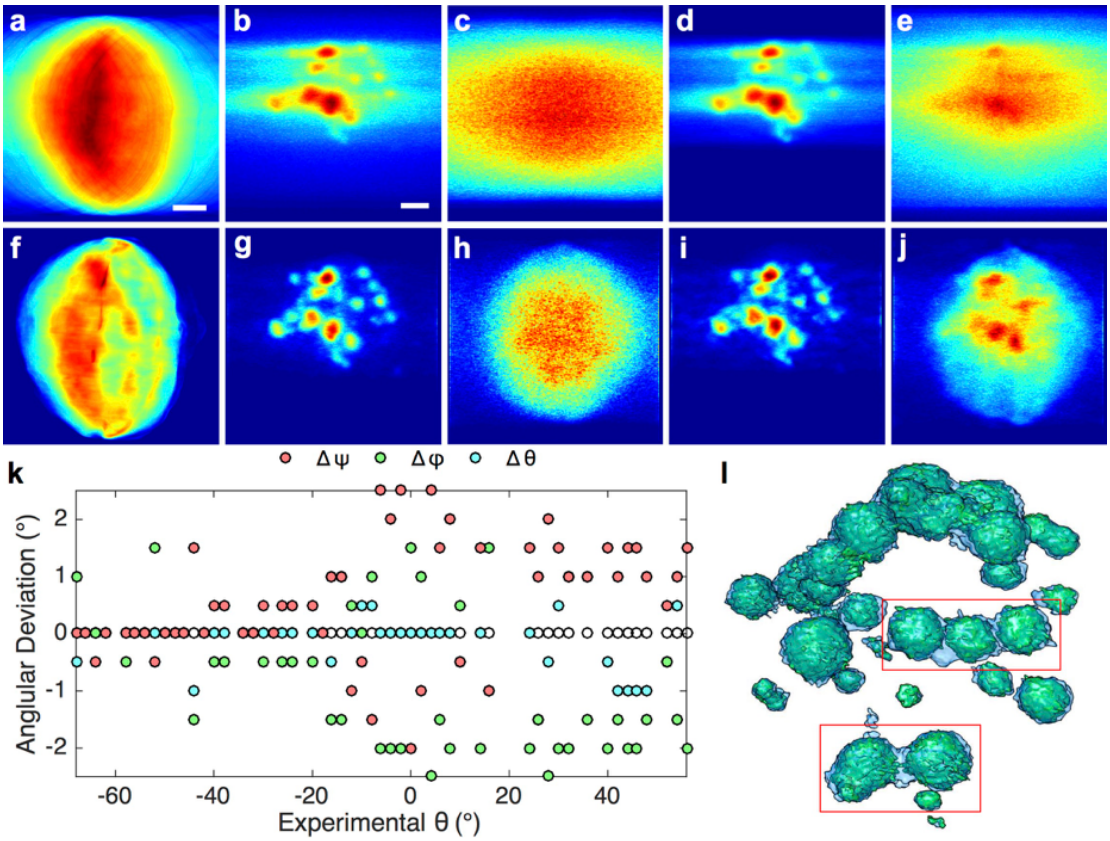

Figure 4.3: GENFIRE and filtered back projection (FBP) reconstruction comparison and angular refinement. **(a–e)** FBP reconstructions for ptychography phase contrast, P, S, Ca and K channels, respectively **(f–j)** GENFIRE reconstructions of the corresponding volumes as shown in **a–e**, showing excellent recovery of missing information in the missing wedge direction. Scale bars 4 μm. **(k)** Angular refinement results revealing angular deviations from zero-degree tilt axis along the and angles (Green: deviation, red: deviation, cyan: deviation). **(l)** Improvements in P channel 3D reconstruction as result of angular refinement. Light-blue and green volumes are before and after angular refinement, respectively. Red boxes highlight volumes where angular refinement improved resolution of individual polyphosphate bodies. (*Figure reprinted from [171]*)

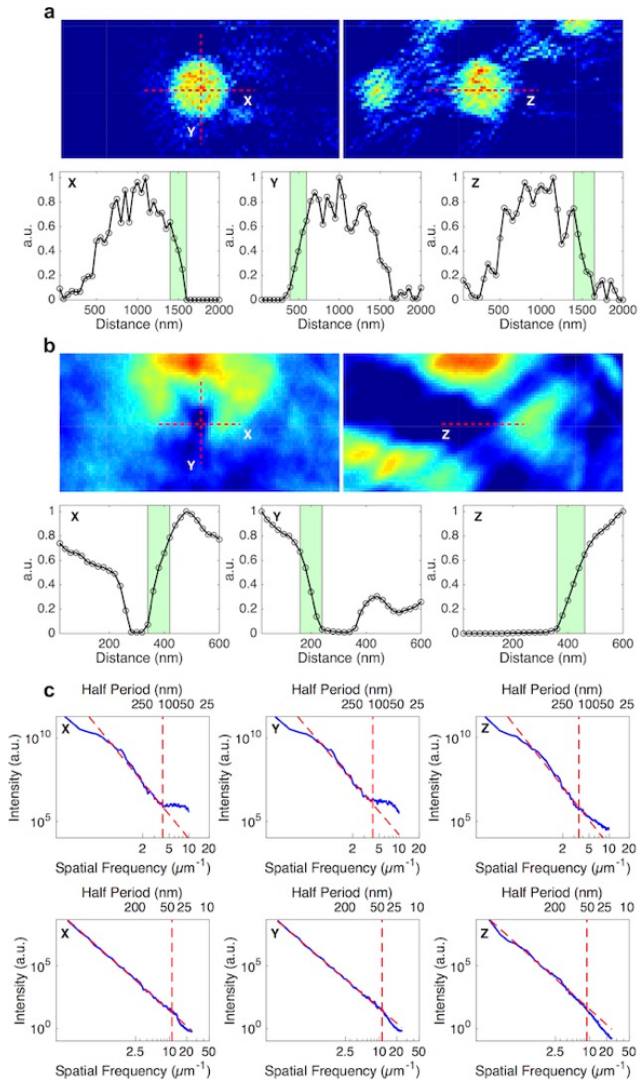

Figure 4.4: Quantification of 3D resolution. **(a)** one-pixel thick layer of a reconstructed polyphosphate body in P channel XFM volume along x and y (top left) and z directions (top right). Line scan profiles along the dash lines shown in the top images gives half-period resolutions of ~125 nm, ~125 nm and ~140 nm in x, y, z, respectively (bottom). **(b)** One-pixel layer through the burnt hole in ptychography reconstruction in x and y (top left) and z (top right). Line scan indicates resolution of ~45 nm along x and y directions, and ~55 nm along z. **(c)** 3D power spectrum analysis of XFM (top row) and ptychography (bottom row) along 3 axial directions, with cutoff spatial frequency at azimuthally averaged signal deviates, showing good agreement in resolution. (*Figure reprinted from [171]*)

without the need for additional labeling and chemical interventions. To extend this correlative imaging methodology to three dimensions, GENFIRE was used to produce 3D reconstruction at sufficient resolutions to isolate individual organelles in 3D. Tomograms provide more clarity about the alga's structure as individual organelles can be mapped in 3D. This type of 3D information can be valuable in other studies where knowing precise distributions or localization of organelles and its internal elemental composition can provide insights into the cell's metabolic state or cellular fate. GENFIRE may also be used as part of an angular refinement procedure to optimize the 3D reconstruction. Our angular refinement result shows small angular deviations in the initial 2/3 of the projections, suggesting that the tomography stage appeared to be stable early on during data acquisition. However, detected angular deviations increased noticeably in the last 1/3 of projections, indicating that the stage is behaving more erratically toward the end of the 3-day experiment. This type of diagnostic information can help devise better data collection schemes to improve the quality of data obtained.

4.4 Conclusion

In this work we have demonstrated a novel application of the GENFIRE tomography reconstruction algorithm by applying it to a correlative X-ray ptychography and X-ray fluorescence microscopy imaging experiment of a frozen-hydrated cell. The 3D fluorescence maps show clear localizations of P-rich polyphosphate bodies and the pyrenoid within the alga, and 3D ptychography map reveals the surrounding ultrastructure with enhanced elemental contrast. We also demonstrate the superior capability of GENFIRE as a tomography reconstruction method and showcased its angular refinement feature to computationally optimize tomography angle inaccuracies due to stage imperfections during data acquisition. The combination of ptychographic and fluorescence tomography can reveal detailed in-

formation on cellular ultrastructure and intracellular trace element distributions. Furthermore, X-ray's high penetration depth and recent advancements in cryogenic sample preservation permit this method to image thick whole cells. This is an especially desirable tool for biologists who are interested in visualizing whole cells in their native state in 3D without any sectioning or chemical labeling. This type of high resolution correlative 3D imaging cannot be achieved with cryogenic electron tomography, which is limited in sample thickness to ~1 μm due to absorption. Moreover, compared to super-resolution optical microscopy, which allows for the selective fluorescent labeling of molecules or molecular assemblies, X-ray diffraction microscopy is based on the natural density variations of biological specimens, so it enables quantitative 3D imaging of whole cells and cellular organelles. In the future this correlative imaging tool can be applied to construct more sophisticated biological 3D models of cellular organisms. With the continued development of specialized beamlines for X-ray ptychography and XFM, we believe this method will become a powerful tool for biologists to study cellular processes and the changes in chemical distributions that govern them.

4.5 Materials and Methods

4.5.1 Sample Cryo-preparation

C. reinhardtii (about 10 um) were grown to the early exponential phase in Tris-Acetate-Phosphate medium at 296 K on a rotary shaker (100 rpm). Five microliters of cell suspensions were dropped onto a plasma treated Si_3N_4 window (200 nm thick, 1.5 mm x 1.5 mm membrane area). The window was then mounted to a VitrobotTM Mark IV plunge freezer (FEI), where the temperature and humidity were set and equilibrated at 22° C and 100%, respectively. The window was blotted for 2 seconds at the blot force of 0, and then immediately plunged into a liquid ethane bath cooled by liquid nitrogen. The cryogenically prepared samples were

observed using a cryogenic light microscope and then stored in liquid nitrogen until they were retrieved for scanning in the X-ray microscope. Cells embedded in various thickness of ice layer were scanned.

4.5.2 Ptychography and XFM 2D Projection Acquisition

Our experiment was carried out at the Bionanoprobe, a hard X-ray nanoprobe with cryogenic sample environment and transfer capabilities located at the Advanced Photon Source at Argonne National Laboratory [173]. For X-ray measurements, a monochromatic X-ray beam at 5.5 keV photon energy was spectrally filtered using a double-crystal Si $< 111 >$ monochromator. Details of the experimental setup (shown in Fig. 4.1) are as follows. A Fresnel zone plate with an outermost zone width of 70 nm was used to focus the coherent X-ray beam down to a spot size of approximately 90 nm. The cryogenically-preserved sample was placed at the focus position, and was scanned in fly-scan mode for data collection [160, 174]. In this fly-scan mode, the fast scan was set along the horizontal x direction, where a piezo scanning stage was set to move across a scan line at a constant velocity by a Delta Tau Turbo PMAC2 Ultralite VME motion control system; the control system used feedback provided by a laser interferometer system reading piezo scanning stage positions to match the desired position and send triggers to detectors. As the sample was on-the-fly scanned, a collimated four-element silicon drift detector (Hitachi Vortex-ME4, mounted at 90° to the incident X-ray beam) and a Dectris Pilatus 100K hybrid pixel array detector (2 m downstream of the sample) were simultaneously triggered for every 50 nm sample motion to record both the fluorescence signals and ptychographic diffraction patterns, respectively. The corresponding pixel time for each acquisition was 65 ms, including 4 ms data readout time between triggers in Pilatus detector. A single projection scan covered 10μm x 10μm field of view which took about 48 mins to collect ~40,000 data points. For tomography, the sample was rotated with 2°

angular spacing, a total of 63 projections at different angles were acquired in an angular range of -68° to 56°.

4.5.3 GENFIRE Tomographic XFM Reconstructions

For XFM tomography, the best 53 out of the 63 projections were manually selected for the dataset from each of the 5 fluorescence channels (Fig. 4.5- 4.9). Hot pixels in the fluorescence images caused by readout errors were removed. In addition, a background subtraction was performed on each projection as follows. First the image was smoothed with a Gaussian kernel and a threshold was applied to define a region outside of the cell. This region was used to calculate a mean background which was subsequently subtracted from each image. Center of mass alignment was performed on the P channel to center the alga to the tilt axis, since the isolated phosphate bodies in the P channel had relatively high signal-to-noise ratio, and these parameters were used to align other channels' projection images which were acquired simultaneously and thus shared the same set of orientation parameters.

4.5.4 GENFIRE Ptychography Tomographic Reconstruction

2D ptychographic projections were reconstructed by a custom software developed for fly-scan ptychography [174]. This code employs graphical-processing-units (GPUs) to speed up data processing [175]. For reconstruction, a central area of 256 x 256 pixels of each diffraction pattern was used, resulting in an image pixel of 10.2 nm. Extended ptychographic iterative engine (ePIE) algorithm [118] was applied with 200 iterations in each ptychography reconstruction. As the monochromator was not stable at the beginning of the experiment, the reconstruction qualities of the first few scans were poor due to an unstable beam function. After excluding these scans and other low-quality projections, only 47 ptychographic projections were used for tomography (Fig. 4.10). The real space 2D phase projection images

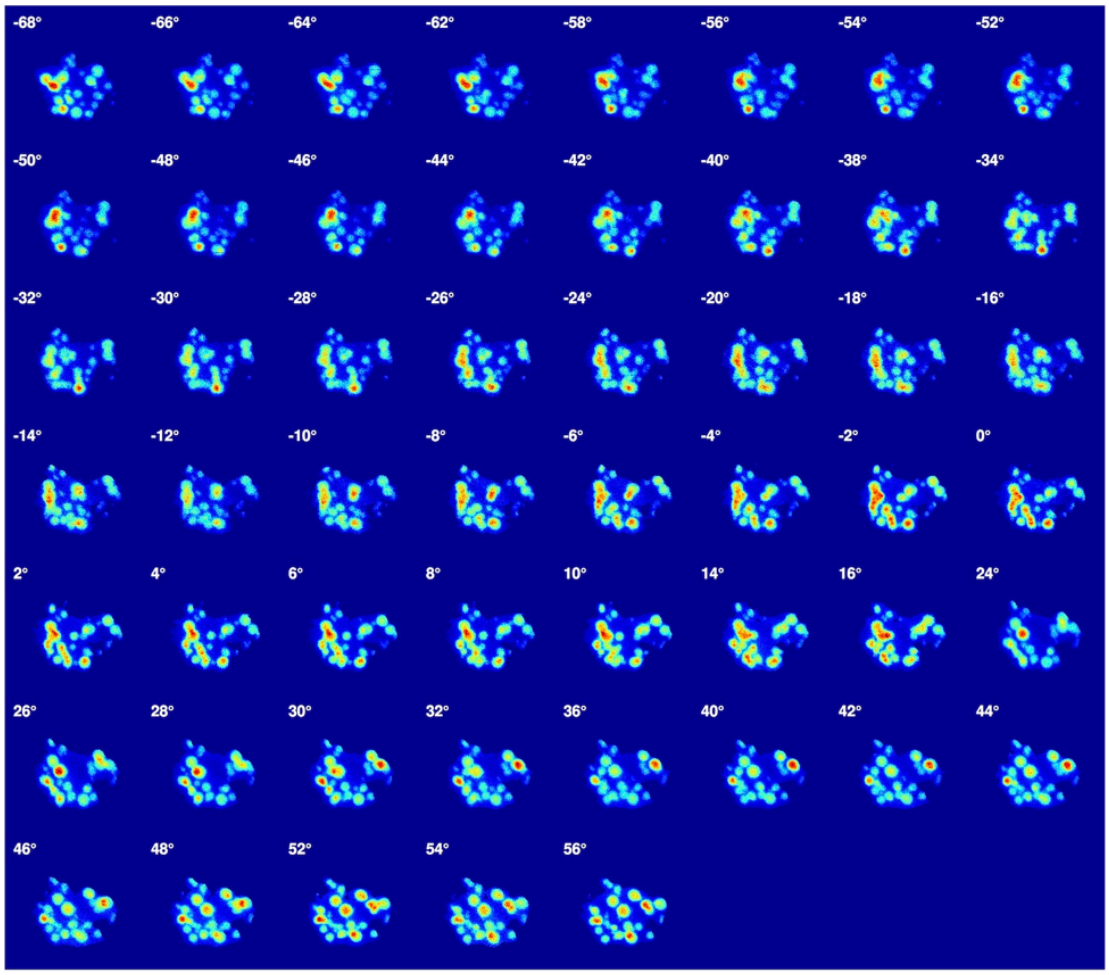

Figure 4.5: P channel XFM projections. (*Figure reprinted from [171]*)

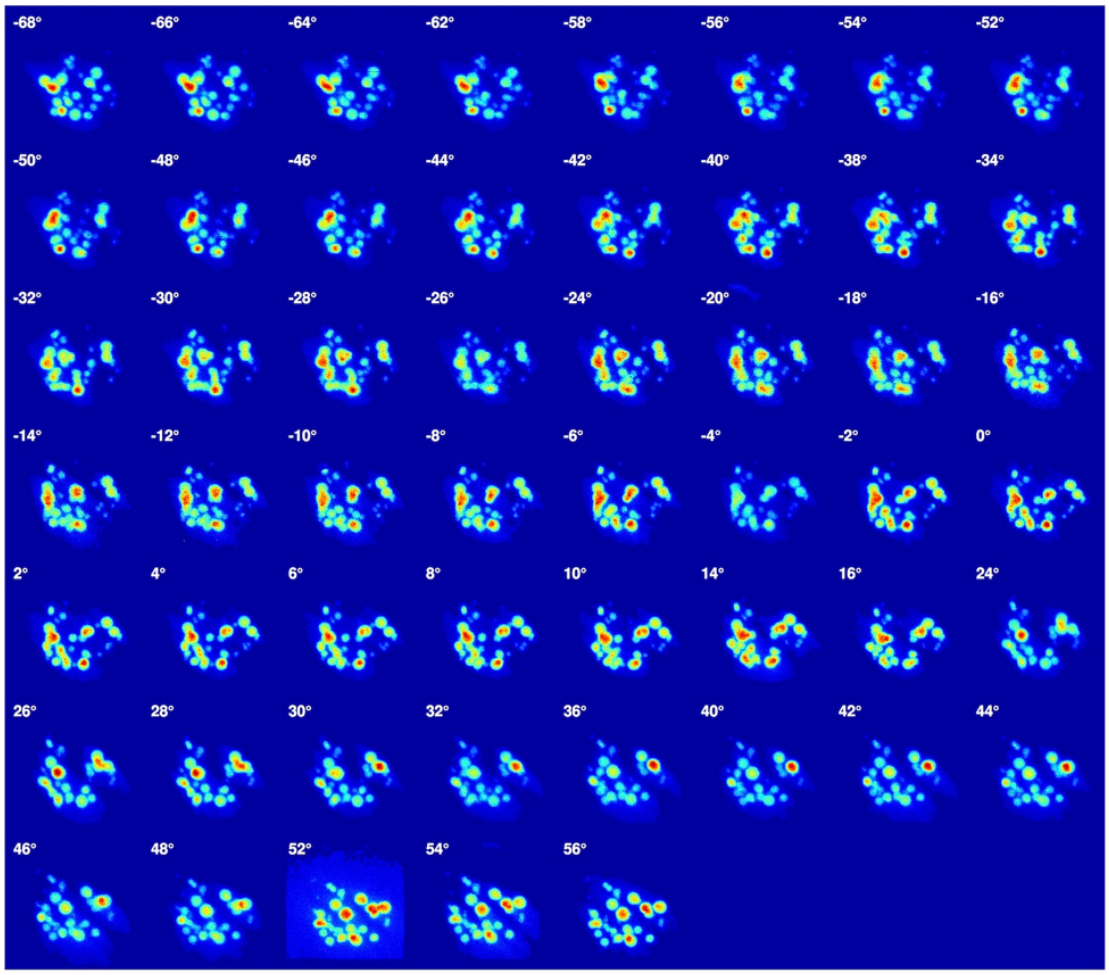

Figure 4.6: Ca channel XFM projections. (*Figure reprinted from [171]*)

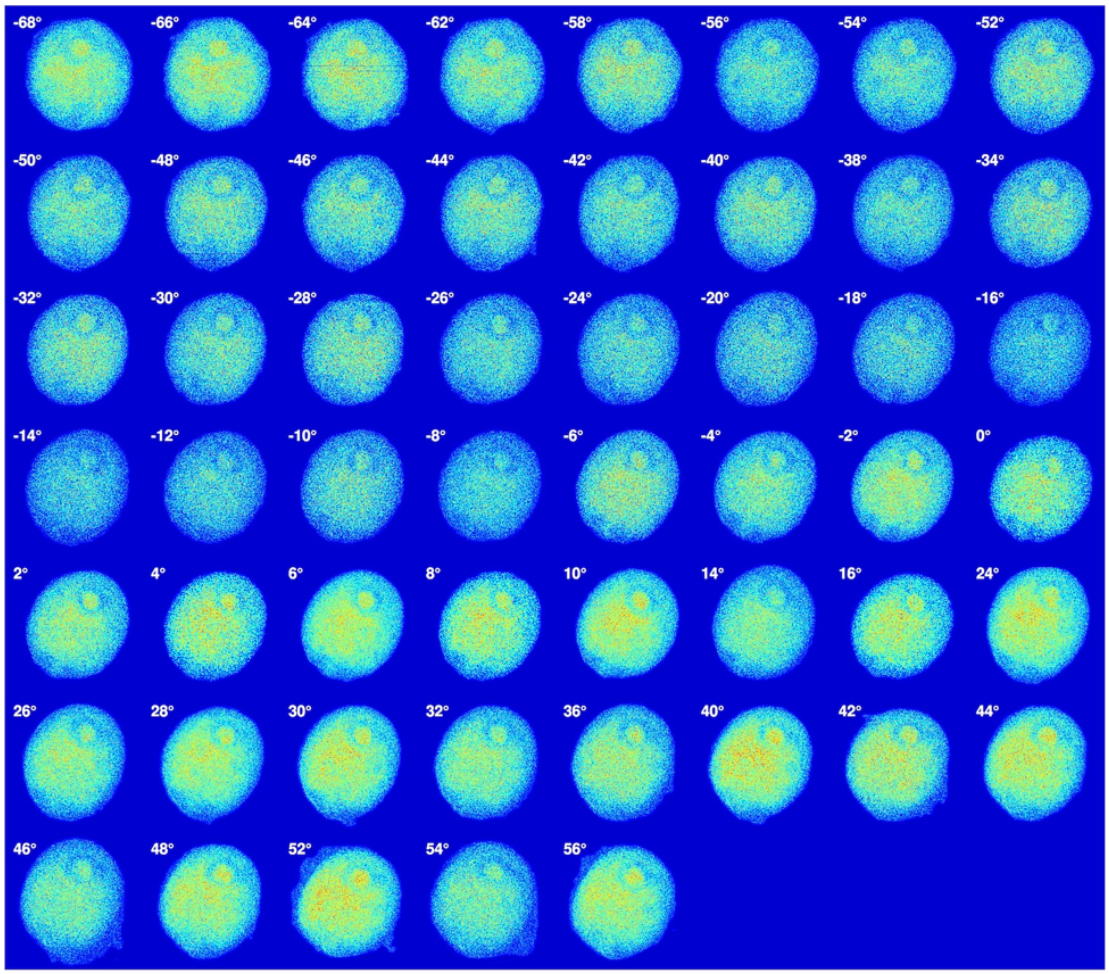

Figure 4.7: S channel XFM projections. (*Figure reprinted from [171]*)

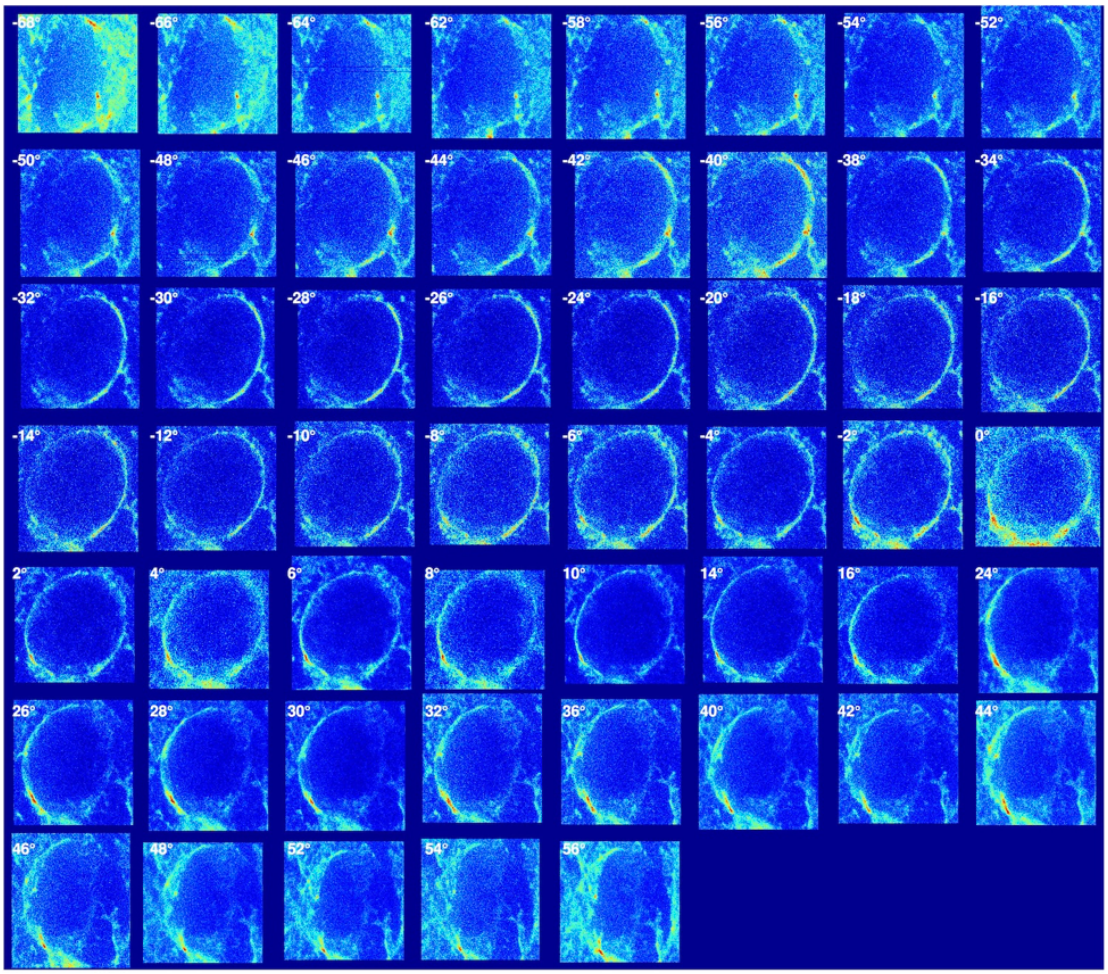

Figure 4.8: Cl channel XFM projections. (*Figure reprinted from [171]*)

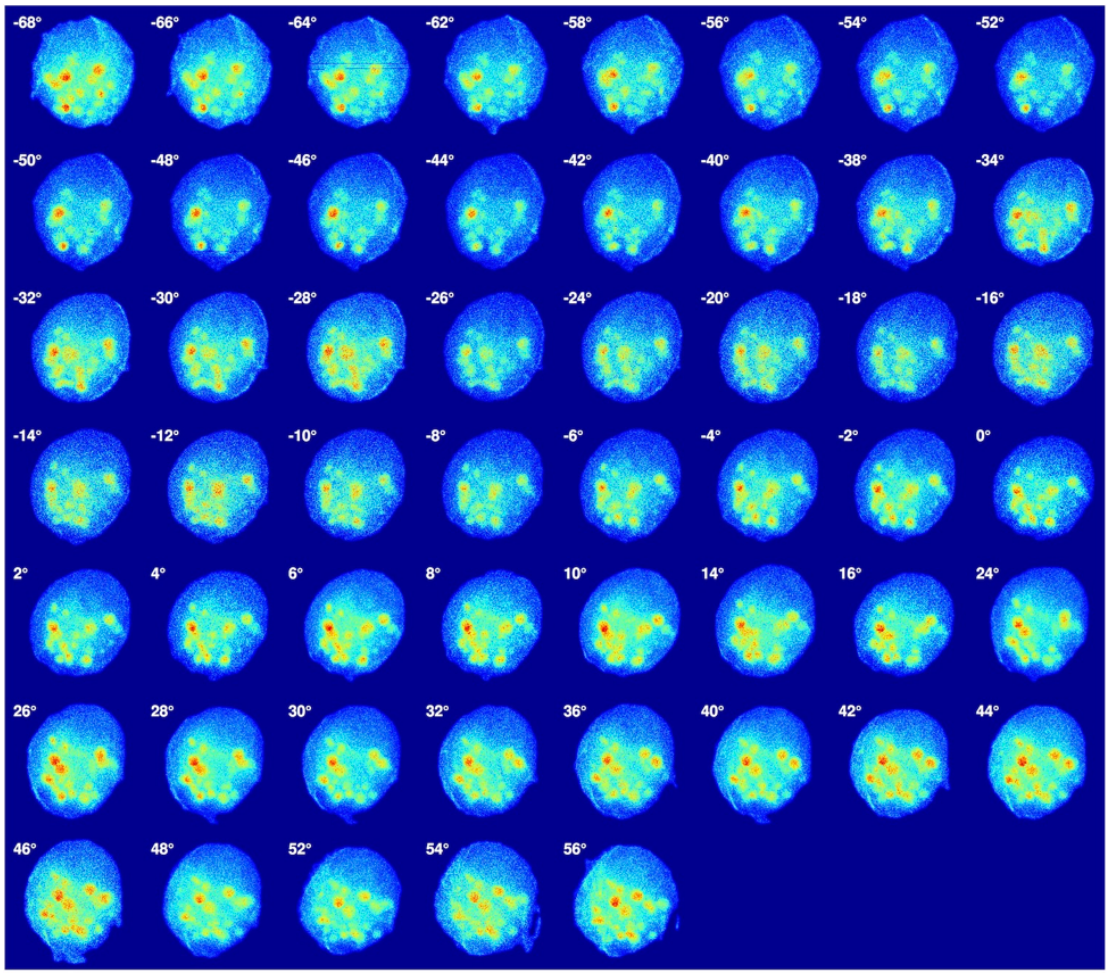

Figure 4.9: K channel XFM projections. (*Figure reprinted from [171]*)

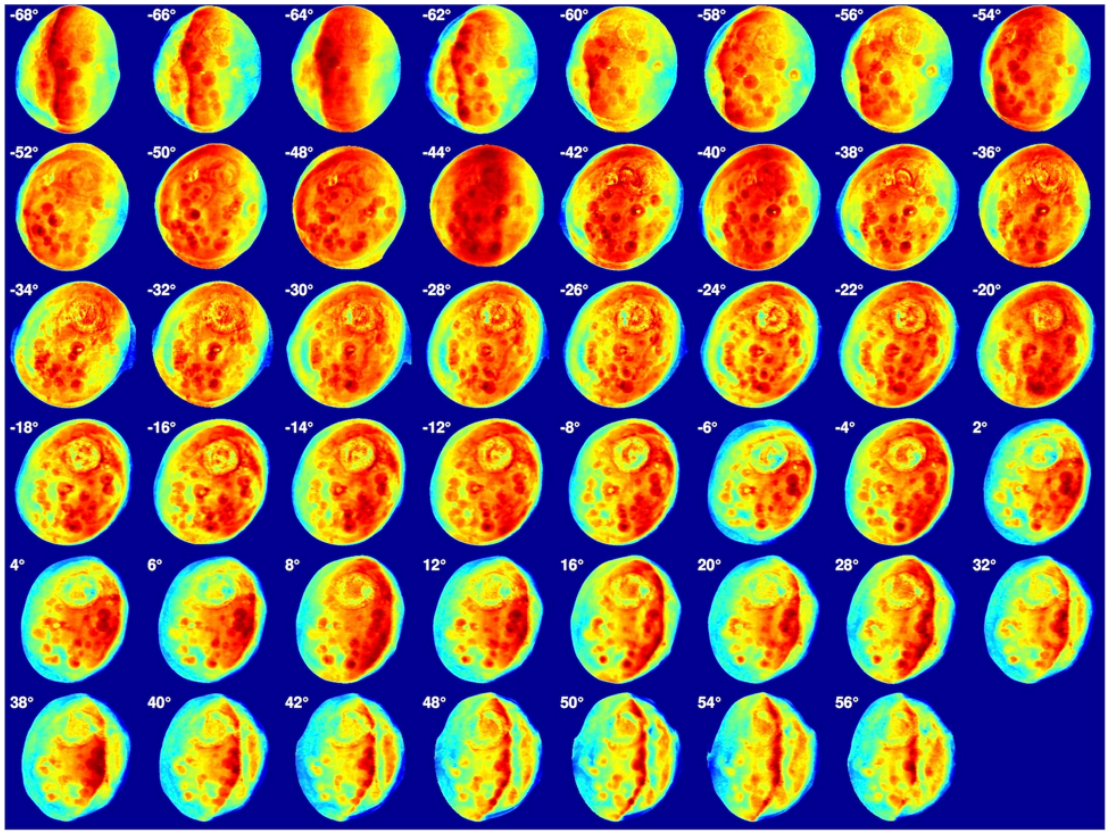

Figure 4.10: Ptychography projections after image pre-processing (i.e. background subtraction, alignment, masking). (*Figure reprinted from [171]*)

were then background subtracted, aligned by the center-of-mass method [22], and binned prior to tomographic reconstruction. For both tomographic reconstructions, 50 iterations of GENFIRE reconstruction were run with an oversampling ratio of 2, followed by 5 iterations of angular refinement to obtain the final reconstructed volumes.

4.5.5 Quantification of Radiation Dose

The X-ray flux after the FZP focusing was of the order of 3 x 10^8 photons/s. For each projection the estimated radiation dose deposited to the sample with 65 ms exposure time per 50 nm^2 pixel was about 2.07 x 10^7 Gy. In the tomography scan consisting of 63 projections, there was 1.30 x 10^9 Gy in total imparted to the sample.

4.6 Acknowledgements

We thank NIH NIGMS for support of this work under grant 1R01GM104530. The Bionanoprobe is funded by NIH/NCRR High End Instrumentation (HEI) grant (1S10RR029272-01) as part of the American Recovery and Reinvestment Act (ARRA). Use of the Advanced Photon Source, an Office of Science User Facility operated for the U.S. Department of Energy (DOE) Office of Science by Argonne National Laboratory, was supported by the U.S. DOE under Contract No. DE-AC02-06CH11357.

CHAPTER 5

Deciphering chemical order/disorder and material properties at the single-atom level

Perfect crystals are rare in nature. Real materials often contain crystal defects and chemical order/disorder such as grain boundaries, dislocations, interfaces, surface reconstructions and point defects [29, 176, 177]. Such disruption in periodicity strongly affects material properties and functionality [29, 176, 177]. Despite rapid development of quantitative material characterization methods [1, 2, 22, 29, 56, 57, 178–187], correlating three-dimensional (3D) atomic arrangements of chemical order/disorder and crystal defects with material properties remains a challenge. On a parallel front, quantum mechanics calculations such as density functional theory (DFT) have progressed from the modeling of ideal bulk systems to modeling "real" materials with dopants, dislocations, grain boundaries and interfaces [188, 189]; but these calculations rely heavily on average atomic models extracted from crystallography. To improve the predictive power of first-principles calculations, there is a pressing need to use atomic coordinates of real systems beyond average crystallographic measurements. Here we determine the 3D coordinates of 6,569 iron and 16,627 platinum atoms in an iron-platinum nanoparticle, and correlate chemical order/disorder and crystal defects with material properties at the single-atom level. We identify rich structural variety with unprecedented 3D detail including atomic composition, grain boundaries, anti-phase boundaries, anti-site point defects and swap defects. We show that the experimentally measured coordinates and chemical species with 22 picometre precision can be used as direct input for

DFT calculations of material properties such as atomic spin and orbital magnetic moments and local magnetocrystalline anisotropy. This work combines 3D atomic structure determination of crystal defects with DFT calculations, which is expected to advance our understanding of structureproperty relationships at the fundamental level.

5.1 Introduction

Intermetallic compounds such as FePt with an ordered face-centred tetragonal ($L1_0$) phase are very promising candidates for next-generation magnetic data storage media and permanent magnet applications [190–194]. As-synthesized, FePt thin films and nanoparticles have a chemically disordered face-centred cubic (fcc) structure ($A1$ phase). When annealed at high temperatures, they undergo a transition from an $A1$ phase to an $L1_0$ phase or to a chemically ordered fcc ($L1_2$) phase, depending on the chemical composition [191–194]. Owing to the chemical ordering and strong spin-orbit coupling, $L1_0$ FePt exhibits extremely large magnetocrystalline anisotropy energy (MAE) [190]. DFT calculations of model FePt nanoparticles have been performed to elucidate the roles of morphology, capping layers and surface segregation in determining the particles spin, orbital magnetic moments and MAE [193, 195, 196], which were compared with experimental measurements from electron microscopy, magnetometry and X-ray magnetic circular dichroism [193, 197, 198]. However, despite extensive studies of this material system, a fundamental understanding of 3D chemical order/disorder, crystal defects and the resulting magnetic properties at the individual atomic level remains elusive. Here we report the precise determination of the 3D coordinates and chemical species of 23,196 atoms in a single 8.4-nm $Fe_{0.28}Pt_{0.72}$ nanoparticle using atomic electron tomography (AET) [29].

5.2 Methods

5.2.1 Sample preparation

FePt nanoparticles were synthesized following procedures published elsewhere [199]. Briefly, 0.5 mmol platinum(II) acetylacetonate ($Pt(acac)_2$) was mixed with 20 ml phenyl ether under a gentle flow of nitrogen (N_2). The mixture was heated to 120°C, and kept at that temperature for 10 min with magnetic stirring. Under a nitrogen blanket, 1 mmol iron pentacarbonyl ($Fe(CO)_5$) was quickly injected, followed by sequential addition of 15 mmol oleic acid and oleylamine. The solution was heated to 220°C in 20 min and kept at that temperature for one hour. Then the mixture was further heated to 260°C and refluxed for another hour. After the solution was cooled down to room temperature, the nanoparticles were precipitated and purified by centrifugation. The collected nanoparticles were dispersed in hexane for storage.

5.2.2 Data acquisition

Samples were prepared by depositing a solution of the FePt nanoparticles in ethanol onto a 5-nm-thick silicon nitride membrane using an atomizer. After the particles were applied to the silicon nitride membrane, they were annealed at 600°C for 25 min in high vacuum. A thin, ultra-pure carbon layer was then applied over the course of 5 min at 700°C to enhance the conductivity of the membranes and to protect the particles from damage under the electron beam. Several tomographic tilt series were acquired from FePt nanoparticles using the TEAM I microscope and TEAM stage [30] at the National Center for Electron Microscopy in the Molecular Foundry. Images were acquired at 300 kV in ADFSTEM mode with a 30-mrad convergence semi-angle (resulting in a probe size of ~0.5 Å), 48 mrad and 251 mrad detector inner and outer semi-angles, and a beam current of 5055 pA (Fig. 5.1). A high-quality tilt series was selected for this study because

of its rich structural variety (Fig. 5.2).

Aberration Coefficients	Value (nm)	95% Confidence (nm)
A1	0	1
B2	13	19
A2	4	21
C3	-268	1,664
S3	107	129
A3	131	220
B4	3,930	5,825
D4	4,016	3,075
A4	3,181	5,005
C5	-705e3	771e3
A5	90e3	119e3

Figure 5.1: Residual aberrations in the STEM probe. Estimates of the residual aberration coefficients as measured by the aberration corrector software on a typical day preceding the ~6-hour experimental tilt series measurement. The 2-fold astigmatism was optimized manually by the operator during the tilt series to avoid issues with drift of the corrector lenses. All first-, second- and third-order aberration coefficients were tuned by the operator to be lower than the reported 95% measurement confidence reported by the software. Only one fourth-order coefficient (D4), a factory alignment not tuned by the operator, is reported as typically larger than the confidence error. Such values will produce the best possible probe size for this microscope based on geometrical estimates. (*Figure reprinted from [3]*)

This tilt series was collected at 68 angles with a tilt range of 65.6° to +64.0°. Ten images per tilt angle were measured with 3 μs dwell time to minimize image blurring. Owing to imperfections in the calibration of the x- and y- scanning coils in the microscopes STEM scanning system, an additional correction was applied to the images to ensure square pixels. This scan distortion was measured using a standard sample under the same imaging conditions and corrected using Fourier methods [200].

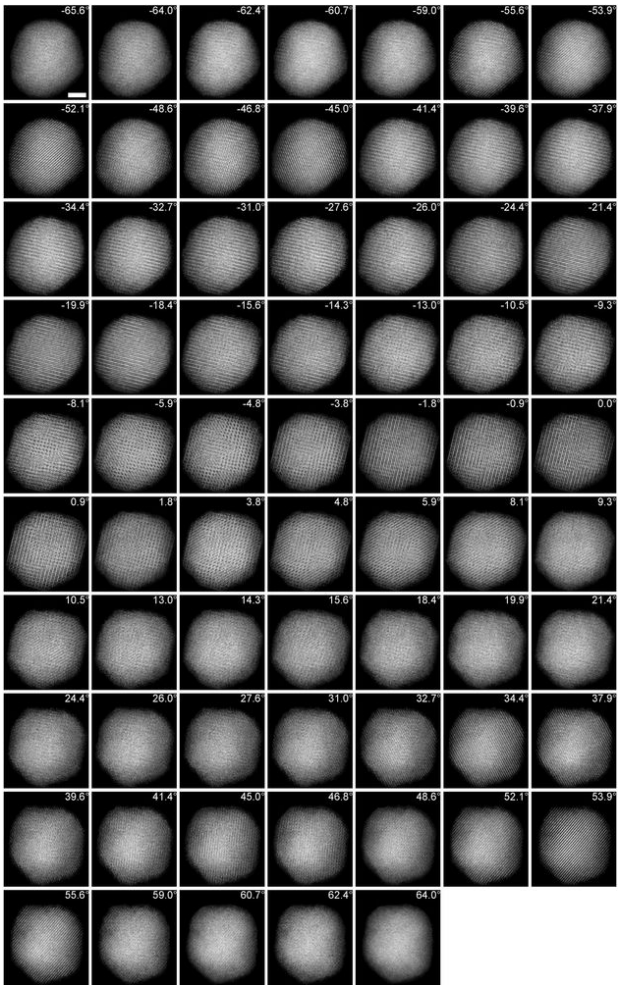

Figure 5.2: A representative tomographic tilt series from an FePt nanoparticle. The 68 projection images with a tilt range from 65.6° to +64.0° (shown at top right of each panel) were measured using an ADF-STEM. Careful examination of images taken before and after the tilt series indicates the consistency of the structure throughout the experiment. The total electron dose of the tilt series is 4.8x10^6 electrons per Å^2. Scale bar at top left, 2nm. (*Figure reprinted from [3]*)

5.2.3 Image denoising

The 10 acquired images for each tilt angle were aligned by cross-correlation with 0.1 pixel steps and averaged. The ADF-STEM images collected with the TEAM I microscope exhibit Poisson-Gaussian mixed noise [1], and follow the noise model of $Y = \alpha P(n_e) + N(\mu_b, \sigma_b)$, where Y is the measured counts of each pixel, α is the gain parameter (counts per electron), $P(n_e)$ is the Poisson distribution of n_e electrons, and $N(\mu_b, \sigma_b)$ is the normal distribution of the mean μ_b and the standard deviation σ_b. The noise parameters α, μ_b, σ_b were estimated from the local mean and the variance based on spatial averaging of acquired images. The images were de-noised by sparse 3D transform-domain collaborative filtering [83], while Anscombe variance-stabilizing transformation and its inverse were applied to the images before and after denoising with estimated noise parameters [201]. The robustness of this denoising method has been tested by other experimental data sets and multislice simulations [1].

5.2.4 GENFIRE reconstruction

After denoising, the 68 images were projected onto the tilt axis (*y-axis*) to obtain 1D curves, and the images were aligned along the tilt axis by using cross-correlation among the 1D curves. During this process, the optimal background of each image was determined by maximizing the crosscorrelation among the 1D curves and was subsequently subtracted from each image. Alignment along the *x-axis* was achieved by the centre of mass method [2]. From the aligned tilt series, a 3D reconstruction was performed using GENFIRE. GENFIRE started with assembling a rectangular 3D Fourier grid from the measured images. For each image, its Fourier transform represents a plane slicing through the origin of the 3D Fourier grid (that is, the Fourier slice theorem [51]). For any Fourier grid point (k_x, k_y, k_z), a perpendicular distance (D_j) to the j^{th} Fourier plane and

the foot of the perpendicular line, (u_j, v_j), were calculated with j = 1, 2, ... 68. The value of (u_j, v_j) was computed from the jth image using the discrete Fourier transform instead of the fast Fourier transform (FFT) as (u_j, v_j) are non-integer coordinates. By repeating the above procedure, we calculated the values of all the (u_j, v_j) points with D_j smaller than a predefined threshold D_{th}, from which the value of the grid point, $F(k_x, k_y, k_z)$, was computed using (Eq 2.1). By properly choosing a suitable oversampling ratio and predefined threshold ($D_{th} = 0.05$ voxels and $O = 4$ in this case), we accurately computed the values of a small fraction of grid points from the images (Eq 2.1). For the remaining grid points without any (u_j, v_j) point satisfying $D_j < D_{th}$, we set them as undefined. The algorithm then iterated between real and reciprocal space using the FFT and its inverse. In real space, a support and positivity were incorporated as constraints. In this case, a 256 x 256 x 256 voxel cube with smoothed edges was used as a support. In each iteration, the values outside the support and the negative values inside the support were set to zero. In reciprocal space, the grid points with measured data were enforced as constraints in each iteration, while the values of the undefined grid points were iteratively updated by the algorithm. The algorithm was monitored by an error metric in each iteration, defined as the difference between the values of the measured and calculated grid points. After 500 iterations, the error metric could not be further improved and an initial 3D reconstruction was obtained. To identify atomic positions and species with high precision, we have implemented a method to refine the tilt angles from the initial 3D reconstruction, which is routinely used in single-particle cryo-electron microscopy [19, 74]. For each tilt orientation, we found the corresponding three Euler angles (ϕ, θ, ψ) and scanned each of the Euler angles with a small angular increment. At each increment, the 3D reconstruction was projected back to calculate a 2D image. An error metric, defined as the difference between the calculated and measured images, was computed. By scanning all the three angles, we obtained an optimal set

of the Euler angles for the tilt orientation, corresponding to the minimum error metric. This procedure was repeated for all the tilt orientations (angles). Because it is computationally intensive to calculate 2D images from a 3D reconstruction, we refined θ and ϕ sequentially. We first scanned θ and used GENFIRE with the refined θ angles to compute a new 3D reconstruction. We then repeated this procedure for the ϕ angles. The angular refinement and reconstruction procedure were iterated until there was no further improvement, producing a final 3D reconstruction. Our numerical simulation and additional experimental results have indicated that GENFIRE produces superior 3D reconstruction relative to other iterative tomographic methods [17, 73] (Chapter 2).

5.2.5 Atom Tracing and Analysis

From the 3D reconstruction, we developed an atom tracing and classification method to determine the coordinates of all individual Fe and Pt atoms based on their local intensity distribution (Methods). This process resulted in a 3D atomic model of 16,627 Pt and 6,569 Fe atoms. To verify this atomic model, we applied multislice simulations to calculate 68 ADF-STEM images from the model using the same experimental parameters (Methods). Fig. 5.6ac shows good agreement between a measured and a simulated (multislice) image. Using the same reconstruction, atom tracing and classification procedures, we obtained a new 3D model consisting of 16,577 Pt and 6,747 Fe atoms. Compared to the experimental atomic model, 99.0% of all atoms are correctly identified in the new 3D model and the root-mean-square deviation of the common atom positions is 22 pm. (Fig. 5.6d). To further confirm the precision of our atomic position measurements, we performed a lattice and structural analysis of the experimental 3D atomic model and determined the atomic displacements of the nanoparticle (Fig. 5.3).

By comparing the atomic positions to an ideal fcc lattice, we estimated an

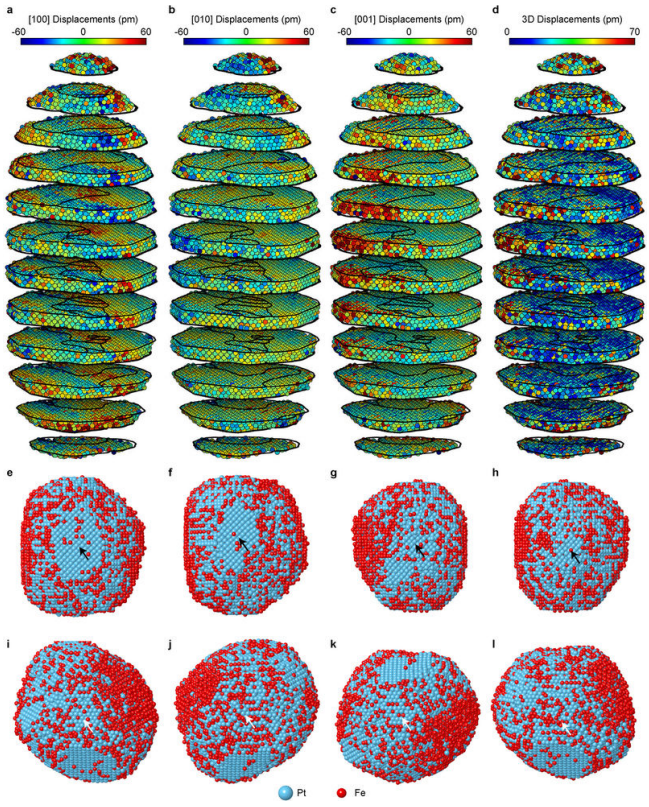

Figure 5.3: Measurements of 3D atomic displacements in the FePt nanoparticle. **(a-c)**, Atomic displacements along the [100] **(a)**, [010] **(b)** and [001] **(c)** directions, determined by quantitatively comparing the measured atomic coordinates with an ideal fcc lattice. **(d)**, 3D atomic displacements in the nanoparticle. The displacement fields indicate that the FePt nanoparticle does not contain substantial strain; the only small strain is observed at the interface between the nanoparticle and the substrate. The black lines in the images show the grain boundaries, indicating that the grain boundaries were not caused by the strain. **(e-h)**, [100] facets of the FePt nanoparticle (black arrows) that are dominated by Pt atoms. **(i-l)**, [111] facets of the FePt nanoparticle (white arrows) that are less dominated by Pt atoms. This experimental observation confirms previous Monte Carlo simulations, which suggested that when there are excess Pt atoms in the fcc cuboctahedral FePt nanoparticle, the [100] facets are more occupied by Pt atoms, while the [111] facets are not. The aggregation of the Fe atoms on two opposite surfaces of the nanoparticle is due to the missing wedge problem. (*Figure reprinted from [3]*)

average 3D precision of 21.6 pm which agrees with the multislice result. Next, we classified the 3D chemical order/disorder of the FePt nanoparticle by determining the short-range order parameter (SROP) of all phases present in the 3D structure (Methods). The nanoparticle consists of two large $L1_2$ $FePt_3$ grains with interlocking concave shapes (Fig. 1). Seven smaller grains are located at the boundary between the two large $L1_2$ grains, including three $L1_2$ $FePt_3$ grains, three $L1_0$ FePt grains and a Pt-rich A1 grain (Fig. 5.4b). This level of complexity of the 3D chemical order/disorder can only be fully revealed by AET [29]. To illustrate this point, we used multislice ADF-STEM simulations to calculate 2D images from the 3D atomic model along the [100], [010] and [001] directions (Fig. 5.4c). Several $L1_0$ grain signatures appearing in the 2D images (magenta in Fig. 5.4c) are actually deceptive structural information, derived from the overlapping of the two large $L1_2$ grains.

Figure 5.5a shows the 3D grain boundaries (black lines) of the nanoparticle. The grains are more ordered in their cores and become less ordered closer to their surfaces. Four representative cut-outs of the atomic model are shown in Fig. 5.5be. The most chemically ordered region of the nanoparticle is at the core of a large $L1_2$ grain with a SROP close to 1 (Fig. 5.5b). Fig. 5.5c shows the grain boundary width varying between two large $L1_2$ grains. Anti-phase boundaries between the two $L1_2$ grains are also observed. The largest $L1_0$ grain is shown in Fig. 5.4b (third grain from the left) and Fig. 5.5d. This $L1_0$ grain sits between the two large $L1_2$ $FePt_3$ grains (Fig. 5.5a) with each of its two Fe sub-lattices matching the Fe sub-lattice of the neighbouring $L1_2$ grains, suggesting the shared Fe lattice with its neighbouring grains may have facilitated the nucleation of the $L1_0$ phase. The central region of the nanoparticle has the highest degree of chemical disorder, including a Pt-rich A1-phase grain (Fig. 5.5e), with much lower SROP values than those in the two large $L1_2$ grains.

With the exponential growth of computing power and improvements in *ab ini-*

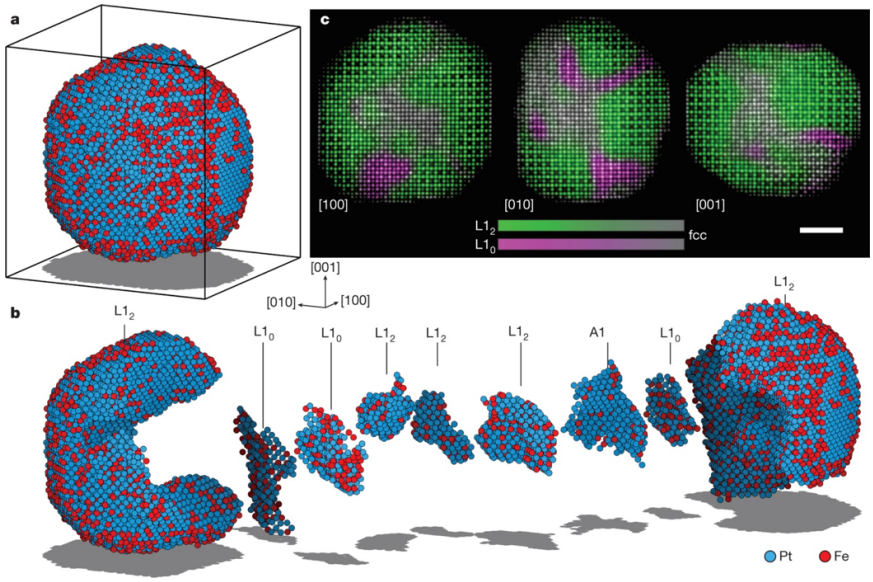

Figure 5.4: 3D determination of atomic coordinates, chemical species and grain structure of an FePt nanoparticle. **(a)**, Overview of the 3D positions of individual atomic species with Fe atoms in red and Pt atoms in blue. **(b)**. The nanoparticle consists of two large $L1_2$ grains, three small $L1_2$ grains, three small $L1_0$ grains and a Pt-rich $A1$ grain. **(c)**, Multislice images obtained from the experimental 3D atomic model along the [100], [010] and [001] directions, where several $L1_0$ grains (magenta) appearing in the 2D images are deceptive structural information. color bars indicate the degree of ordering, from pure $L1_2/L1_0$ to chemically disordered fcc. Scale bar, 2nm. (*Figure reprinted from [3]*)

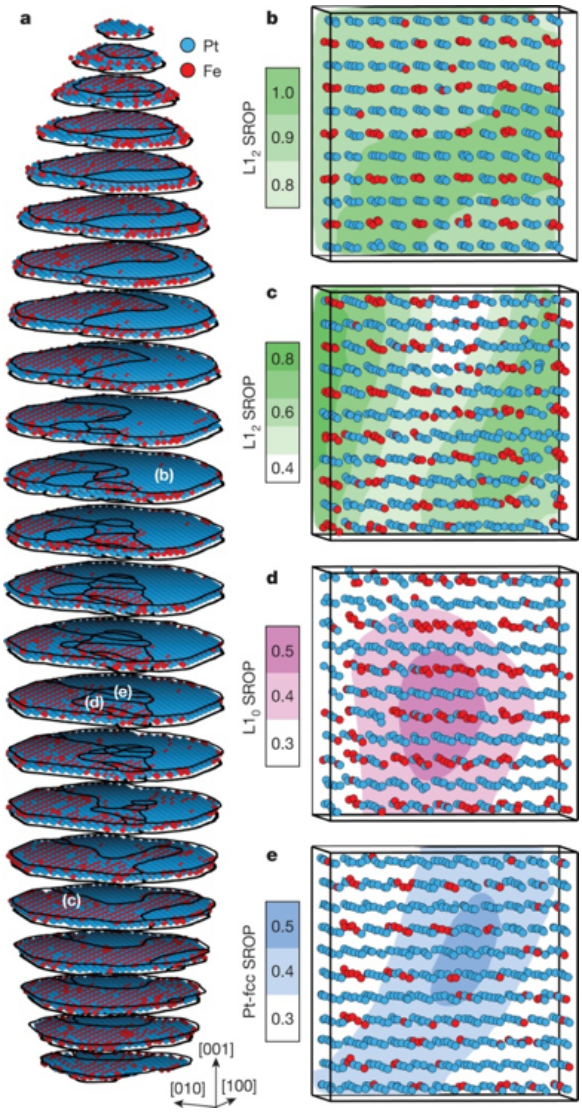

Figure 5.5: 3D identification of grain boundaries and chemical order/disorder. **(a)** Atomic coordinates and species of the FePt nanoparticle divided into slices one fcc unit-cell thick. The grain boundaries are marked with black lines. (**b-e**) Four representative cut-outs of the experimental atomic model, showing the most chemically ordered $L1_2$ region of the particle **(b)**. a grain boundary between the two large $L1_2$ grains **(c)**, the largest $L1_0$ grain **(d)**, and the most chemically disordered region of the particle centred on a Pt-rich $A1$ grain **(e)**. The locations of the cut-outs are labelled in parentheses in (**a**), and the SROP of each cut-out is averaged along the [010] viewing direction and displayed as the background color (see color bar at left of (**b**–**e**). (*Figure reprinted from [3]*)

tio techniques, our measured atomic coordinates of the whole FePt nanoparticle with 23,196 atoms could be used as direct input for first-principles calculations. The local MAE and atomic magnetic moments extracted from the nanoparticle could then be used as parameters for micromagnetic simulations33, whose precision is at present limited by parameters taken from either bulk or modelled values. Looking forward, the ability to determine the chemical order/ disorder and crystal defects with high precision and to correlate their 3D atomic arrangements with material properties at the single-atom level is expected to find applications in materials science, physics, chemistry, nanoscience and nanotechnology.

5.2.6 Multislice STEM simulations

A tilt series of 68 images with refined experimental Euler angles were calculated using multislice simulations [20]. A total of 68 cubic super cells with a = 100 Å were created. The final 3D atomic model was placed within the super cells. Individual super cells were divided into multiple 2.0-Å-thick slices along the z-axis, with 1,800 x 1,800 pixels sampling in the *x*- and *y-axes* for both the specimen and probe. The experimental parameters (300 keV electron energy, 0 mm C3 aberration, 5 mm C5 aberration, 30 mrad convergence semi-angle, 48 and 251 mrad detector inner and outer semi-angles) were used for the simulations, resulting in a tilt series of ADF-STEM images with 255 x 255 pixels per image and a pixel size of 0.37 Å. For each tilt angle, 16 frozen phonon configurations were simulated and averaged to obtain a calculated image. Each multislice image was convolved with a Gaussian function, whose width was determined by minimizing the error between the measured and simulated images. This procedure was used to account for the electron probe size and other incoherent effects. Fig. 5.6 compares the measured and multislice simulated images at 0° tilt. A 3D volume was then reconstructed from the simulated tilt series with GENFIRE, and a new 3D model was obtained by using the same atom tracing procedure.

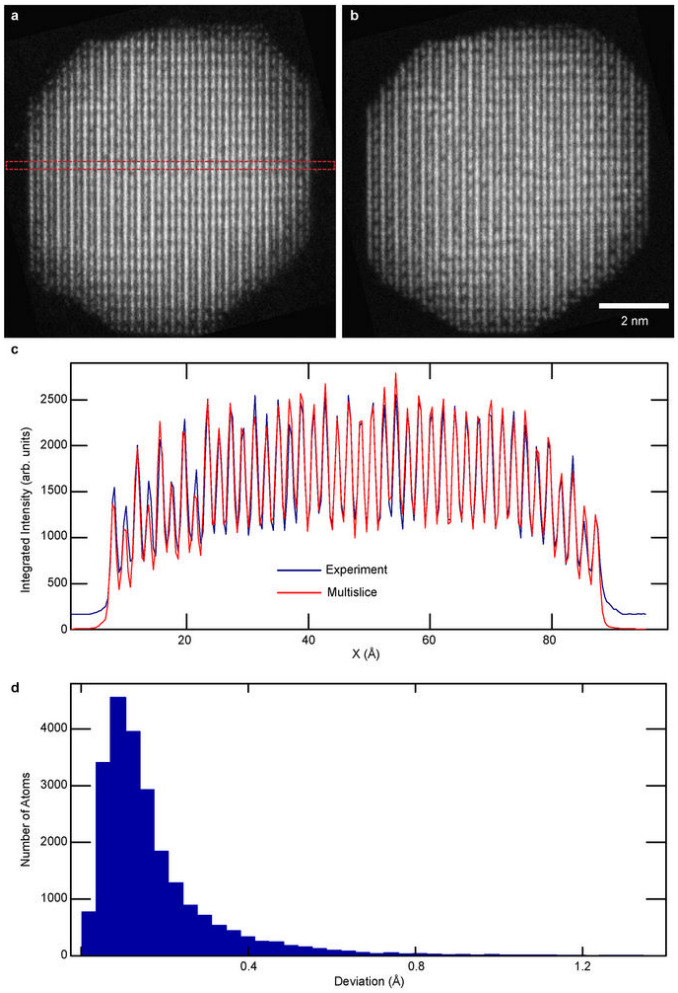

Figure 5.6: Validating the measured atomic model using multislice STEM simulations. **(a)**, **(b)**, Comparison between the experimental (a) and multislice ADF-STEM simulation **(b)** images at 0° tilt. The multislice image was convolved with a Gaussian function to account for the source size and other incoherent effects. Poisson-Gaussian noise was then added to the multislice image. **(c)**, Line-cut of **(a)** and **(b)** along the dashed rectangle in **(a)**, showing good agreement between the experimental and multislice images. Note that a slight in-plane rotation was applied to the images to make horizontal line-cuts for a quantitative comparison. **(d)**, Histogram of the difference (deviation) in atomic positions between the experimental atomic model and that obtained from 68 multislice images. 99.0% of the atoms were correctly identified with a root-mean-square deviation of 22 pm. (*Figure reprinted from [3]*)

A total of 23,324 atoms were traced, comprising 16,577 Pt and 6,747 Fe atoms. 23,043 common pairs of the atoms between experimental and multislice 3D model were selected based on the criterion that each pair should be within the radius of the Fe atom. Among the common pairs, 6,401 common pairs were identified as Fe atoms (97.4%), and 16,562 common pairs were identified as Pt atoms (99.6%), resulting in 99.0% of all atoms having been correctly identified. A histogram of the atomic deviation between the common pairs is shown in Fig. 5.6d, indicating a root-mean-square deviation of 22.2 pm. This simulation requires many days using an advanced computing cluster; however, a recently developed software package called *Prismatic* demonstrates potential for alleviating this concern [202](Appendix A).

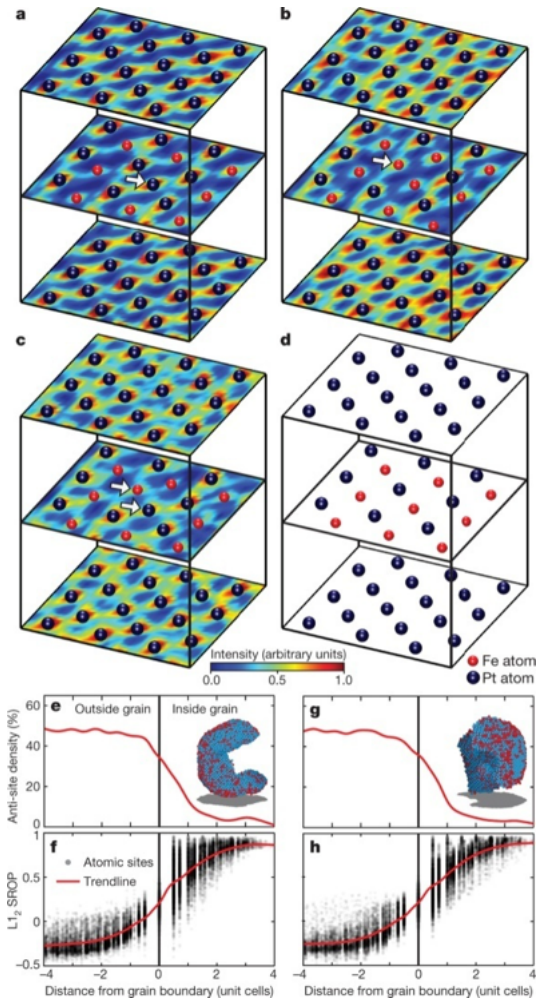

Figure 5.7: Observation of anti-site point and swap defects, and statistical analysis of the chemical order/disorder and anti-site density. (**a-c**) 3D atomic positions overlaid on the 3D reconstructed intensity (color scale at bottom) illustrating anti-site point defects (arrows): a Pt atom occupying an Fe atom site **(a)**, an Fe atom occupying a Pt atom site **(b)**, a pair of nearest-neighbour Fe and Pt atoms are swapped (swap defect) **(c)**. **(d)** 3D atomic structure of an ideal $L1_2$ $FePt_3$ phase for reference. The anti-site defect density **(e)** and SROP (f) for a large $L1_2$ grain, inset in **(e)**, as a function of the distance from the grain surface (unit cell size=3.875Å). The anti-site defect density **(g)** and SROP **(h)** for the other large $L1_2$ grain, inset in **(g)**, as a function of the distance from the grain surface. Smooth red trend lines are overlaid on the defect density distribution as a guide for the eye. (*Figure reprinted from [3]*)

APPENDIX A

A streaming multi-GPU implementation of image simulation algorithms in scanning transmission electron microscopy

Simulation of atomic resolution image formation in scanning transmission electron microscopy can require significant computation times using traditional methods. A recently developed method, termed PRISM, demonstrates potential for significant acceleration of such simulations with negligible loss of accuracy. Here we present a software package called *Prismatic* for parallelized simulation of image formation in STEM using both the PRISM and multislice methods. By distributing the workload between multiple CUDA-enabled GPUs and multicore processors, accelerations as high as 1000x for PRISM and 30x for multislice are achieved relative to traditional implementations using a single 4-GPU machine. *Prismatic* is freely available as an open-source CUDA/C++ package (http://prism-em.com) with both a command line and graphical user interface.

A.1 Introduction

Scanning transmission electron microscopy (STEM) has had a major impact on materials science [203, 204], especially for atomic-resolution imaging since the widespread adoption of hardware aberration correction [205–207]. Many large-scale STEM experimental techniques are routinely validated using imaging or diffraction simulations, such as electron ptychography [208], 3D atomic recon-

struction using dynamical scattering [209], high precision surface atom position measurements on catalytic particles [210], de-noising routines [211], phase contrast imaging with phase plates [212], new dynamical atomic contrast models [213], 3D atomic electron tomography [3], and many others. The most commonly employed simulation algorithm for STEM simulation is the multislice algorithm introduced by Cowlie and Moodie [214]. This method consists of two main steps. The first is calculation of the projected potentials from all atoms into a series of 2D slices. Second, the electron wave is initialized and propagated through the sample. The multislice method is straightforward to implement and is quite efficient for plane-wave or single-probe diffraction simulations [215].

A large number of electron microscopy simulation codes are available, summarized in Table A.1. Most of these codes use the multislice method, and many have implemented parallel processing algorithms for both central processing units (CPUs) and graphics processing units (GPUs). Recently some authors have begun using hybrid CPU+GPU codes for multislice simulation [234]. Multislice simulation relies heavily on the the fast Fourier transform (FFT) which can be computed using heavily optimized packages for both CPUs [235] and GPUs [236]. The other primary computational requirement of multislice calculations is large element-wise matrix arithmetic, which GPUs are very well-suited to perform [237]. Parallelization is important because STEM experiments may record a few integrated values or even full probe images from thousands or even millions of probe positions [212, 238]. Performing STEM simulations on the same scale as these experiments is very challenging, because in the conventional multislice algorithm the propagation of each STEM probe through the sample is computed separately. Furthermore, if additional simulation parameters are explored the number of required simulations can become even larger, requiring very large computation times even using a modern, paralellized implementation. To address this issue, we introduced a new algorithm that offers a substantial speed increase for STEM image

Table A.1: A non-exhaustive list of electron microscopy simulation codes. (*Figure reprinted from [202]*)

Code(s)	Author(s)	Reference(s)	Comments
xHREM	Ishizuka	[216, 217]	
computem	Kirkland	[20, 215]	CPU parallelized
EMS, JEMS	Stadelmann	[218, 219]	
MacTempas	Kilaas	[220]	
QSTEM	Koch	[221]	
CTEMsoft	De Graef	[222]	
Web-EMAPS	Zuo et al.	[223]	deprecated
STEM_CELL	Carlino, Grillo et al.	[224, 225]	CPU parallelized
STEMSIM	Rosenauer and Schowalter	[226]	
MALTS	Walton et al.	[227]	Lorentz TEM
Dr. Probe	Barthel and Houben	[228]	
FDES	Van den Broek et al.	[229]	GPU parallelized
μSTEM	D'Alfonso et al.	[230, 231]	GPU par., inelastic
STEMsalabim	Oelerich et al.	[232]	CPU parallelized
Prismatic	Pryor Jr. and Ophus	[233], this work	multi-GPU streaming

simulations [233]. This algorithm is referred to as the plane-wave reciprocal-space interpolated scattering matrix (PRISM) method.

In this manuscript, we introduce a highly-optimized multi-GPU simulation code that can perform both multislice and PRISM simulations of extremely large structures called *Prismatic*. We will briefly describe the multislice and PRISM algorithms, and describe the implementation details for our parallelized CPU and CPU+GPU codes. We perform timing benchmarks to compare both algorithms under a variety of conditions. Finally, we demonstrate the utility of our new code with typical use cases and compare with the popular package *computem* [20]. *Prismatic* includes a graphical user interface (GUI) and uses the cross-platform build system CMake [239]. All of the source code is freely available. Throughout this manuscript, we use the NVIDIA convention of referring to the CPU and GPU(s) as the host and device(s), respectively.

A.2 Methods

A.2.1 Description of Algorithms

A flow chart of the steps performed in our code are given in Fig. A.1. Both multislice and PRISM share the same initial steps, where the sample is divided into slices which are used to compute the projected potential from the atomic scattering factors give in [20]. This step is shown schematically in Figs. A.1a and b, and is implemented by using a precomputed lookup table for each atom type [212, 233].

Figs.A.1c-e show the steps in a multislice STEM simulation. First the complex electron wave Ψ representing the initial converged probe is defined, typically as an Airy disk function shown in Fig. A.1c. This probe is positioned at the desired location on the sample surface in realspace, as in Fig. A.1d. Next, this probe

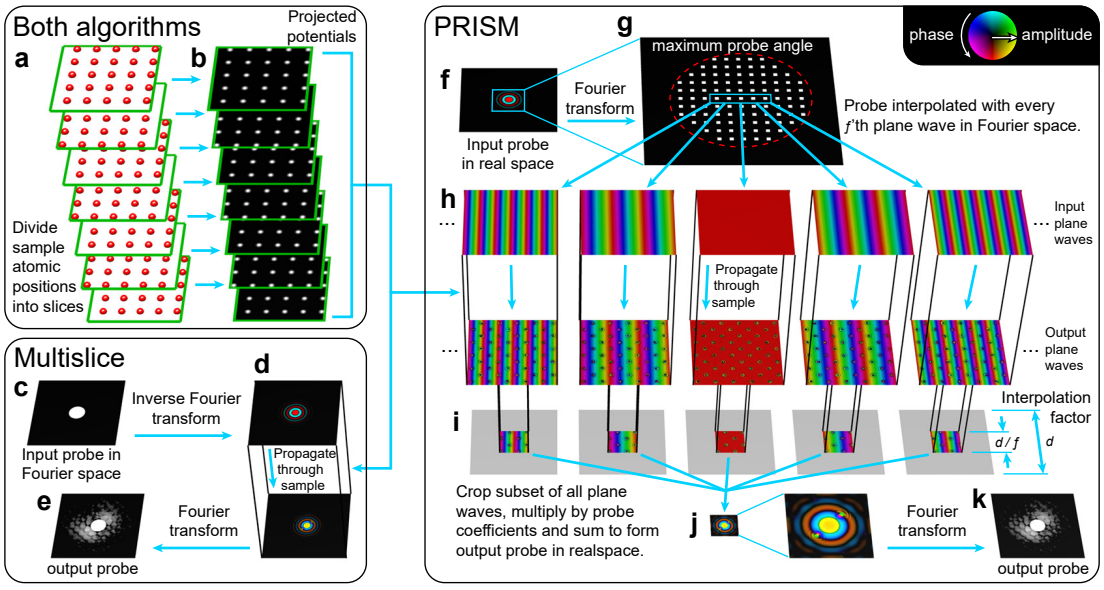

Figure A.1: Flow chart of STEM simulation algorithm steps. **(a)** All atoms are separated into slices at different positions along the beam direction, and **(b)** atomic scattering factors are used to compute projected potential of each slice. **(c)** Multislice algorithm, where each converged probe is initialized, **(d)** propagated through each of the sample slices defined in **(b)**, and then **(e)** output either as images, or radially integrated detectors. **(f)** PRISM algorithm where **(h)** converged probes are defined in coordinate system downsampled by factor f as a set of plane waves. **(h)** Each required plane wave is propagated through the sample slices defined in **(b)**. **(i)** Output probes are computed by cropping subset of plane waves multiplied by probe complex coefficients, and **(j)** summed to form output probe, **(k)** which is then saved. (*Figure reprinted from [202]*)

is propagated through the sample's potential slices defined in Fig. A.1b. This propagation is achieved by alternating two steps. The first step is a transmission through a given potential slice V_p^{2D} over the realspace coordinates $\vec{r}$

$$\psi_{p+1}(\vec{r}) = \psi_p(\vec{r}) \exp\left[\sigma V_p^{2D}(\vec{r})\right] \tag{A.1}$$

where σ is the beam-sample interaction constant. Next, the electron wave is propagated over the distance t to the next sample potential slice, which is done in Fourier space over the Fourier coordinates $\vec{q}$

$$\Psi_{p+1}(\vec{q}) = \Psi_p(\vec{q}) \exp(-i\pi\lambda|\vec{q}|^2 t) \tag{A.2}$$

where λ is the electron wavelength. These steps are alternated until the electron probe has been propagated through the entire sample. Next, the simulated output is computed, which is typically a subset of the probe's intensity summed in Fourier space as shown in Fig. A.1e. The steps given in Figs. A.1c-e are repeated for the desired probe positions, typically a 2D grid. The simulation result can be a single virtual detector, an array of annular ring virtual detectors or the entire probe diffraction pattern for each probe location, giving a 2D, 3D or 4D output respectively. For more details on the multislice method we refer readers to Kirkland [20].

The PRISM simulation method for STEM images is outlined in Figs. A.1f-k. This method exploits the fact that an electron scattering simulation can be decomposed into an orthogonal basis set, as in the Bloch wave method [20]. If we compute the electron scattering for a set of plane waves that forms a complete basis, these waves can each be multiplied by a complex scalar value and summed to give a desired electron probe. A detailed description of the PRISM algorithm is given in [233].

The first step of PRISM is to compute the sample potential slices as in Figs.A.1a-b. Next, a maximum input probe semi-angle and an interpolation factor

f is defined for the simulation. Fig. A.1g shows how these two variables specify the plane wave calculations required for PRISM, where every f^{th} plane wave in both spatial dimensions inside the maximum scattering angle is required. Each of these plane waves must be propagated through the sample using the multislice method given above, shown in Fig. A.1h. Once all of these plane waves have been propagated through the sample, together they form the desired basis set we refer to as the compact S-matrix. Next we define the location of all desired STEM probes. For each probe, a subset of all plane waves is cut out around the maximum value of the input STEM probe. The size length of the subset regions is d/f, where d is the simulation cell length. The probe coefficients for all plane waves are complex values that define the center position of the STEM probe, and coherent wave aberrations such as defocus or spherical aberration. Each STEM probe is computed by multiplying each plane wave subset by the appropriate coefficient and summing all wave subsets. This is equivalent to using Fourier interpolation to approximate the electron probe wavefunction. As long as the subset region is large enough to encompass the vast majority of the probe intensity, the error in this approximation will be negligible [233]. Finally, the output signal is computed for all probes as above, giving a 2D, 3D or 4D output array. As will be shown below, STEM simulations using the PRISM method can be significantly faster than using the multislice method.

A.3 Implementation Details

A.3.1 Computational Model

Wherever possible, parallelizable calculations in *Prismatic* are divided into individual tasks and performed using a pool of CPU and GPU worker threads that asynchronously consume the work on the host or the device, respectively. We refer to a GPU worker thread as a host thread that manages work dispatched to a

single device context. Whenever one of these worker threads is available, it queries a mutex-synchronized dispatcher that returns a unique work ID or range of IDs. The corresponding work is then consumed, and the dispatcher requeried until no more work remains. This computational model, depicted visually in Fig. A.2, provides maximal load balancing at essentially no cost, as workers are free to independently obtain work as often as they become available. Therefore, machines with faster CPUs may observe more work being performed on the host, and if multiple GPU models are installed in the same system their relative performance is irrelevant to the efficiency of work dispatch. The GPU workers complete most types of tasks used by *Prismatic* well over an order of magnitude faster than the CPU on modern hardware, and if a CPU worker is dispatched one of the last pieces of work then the entire program may be forced to unnecessarily wait on the slower worker to complete. Therefore, an adjustable early stopping mechanism is provided for the CPU workers.

GPU calculations in *Prismatic* are performed using a fully asynchronous memory transfer and computational model driven by CUDA streams. By default, kernel launches and calls to the CUDA runtime API for transferring memory occur on what is known as the default stream and subsequently execute in order. This serialization does not fully utilize the hardware, as it is possible to simultaneously perform a number of operations such as memory transfer from the host to the device, memory transfer from the device to the host, and kernel execution concurrently. This level of concurrency can be achieved using CUDA streams. Each CUDA stream represents an independent queue of tasks using a single device that execute internally in exact order, but that can be scheduled to run concurrently irrespective of other streams if certain conditions are met. This streaming model combined with the multithreaded work dispatch approach described previously allow for concurrent two-way host/device memory transfers and simultaneous data processing. A snapshot of the output produced by the NVIDA Visual Profiler

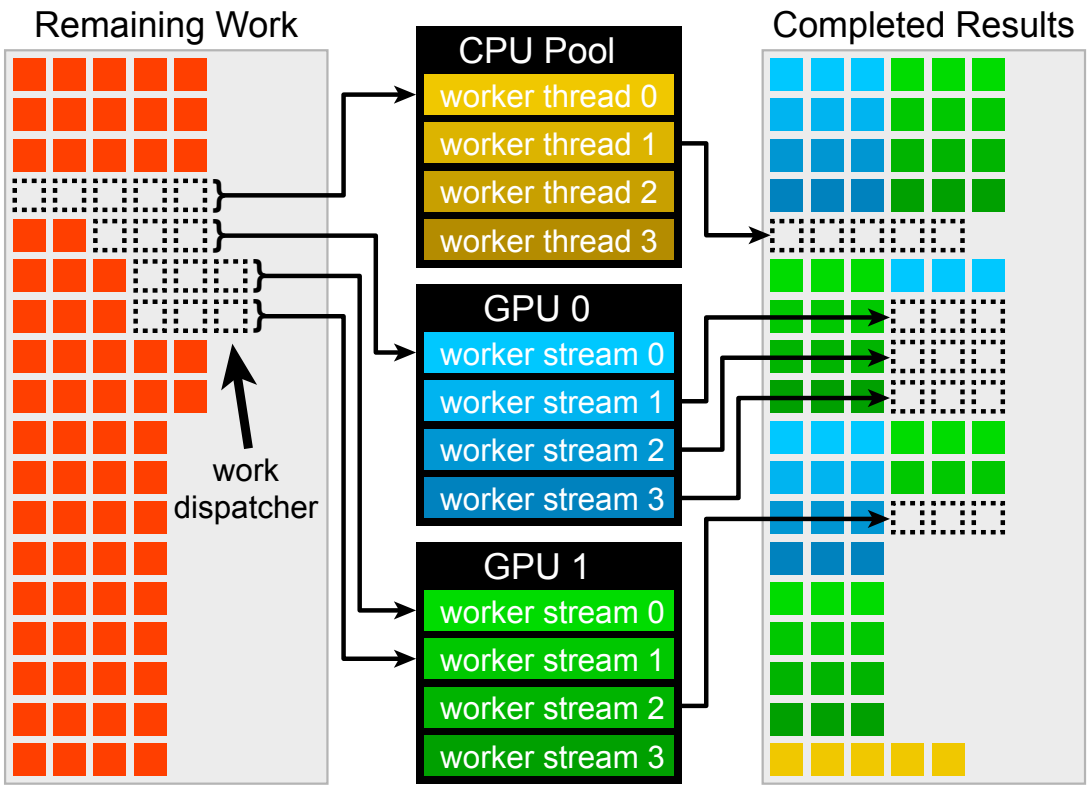

Figure A.2: Visualization of the computation model used repeatedly in the *Prismatic* software package, whereby a pool of GPU and CPU workers are assigned batches of work by querying a synchronized work dispatcher. Once the assignment is complete, the worker requests more work until no more exists. All workers record completed simulation outputs in parallel. (*Figure reprinted from [202]*)

for a single device context during a streaming multislice simulation similar to those described later in this work verifies that *Prismatic* is indeed capable of such concurrency (Fig. A.3).

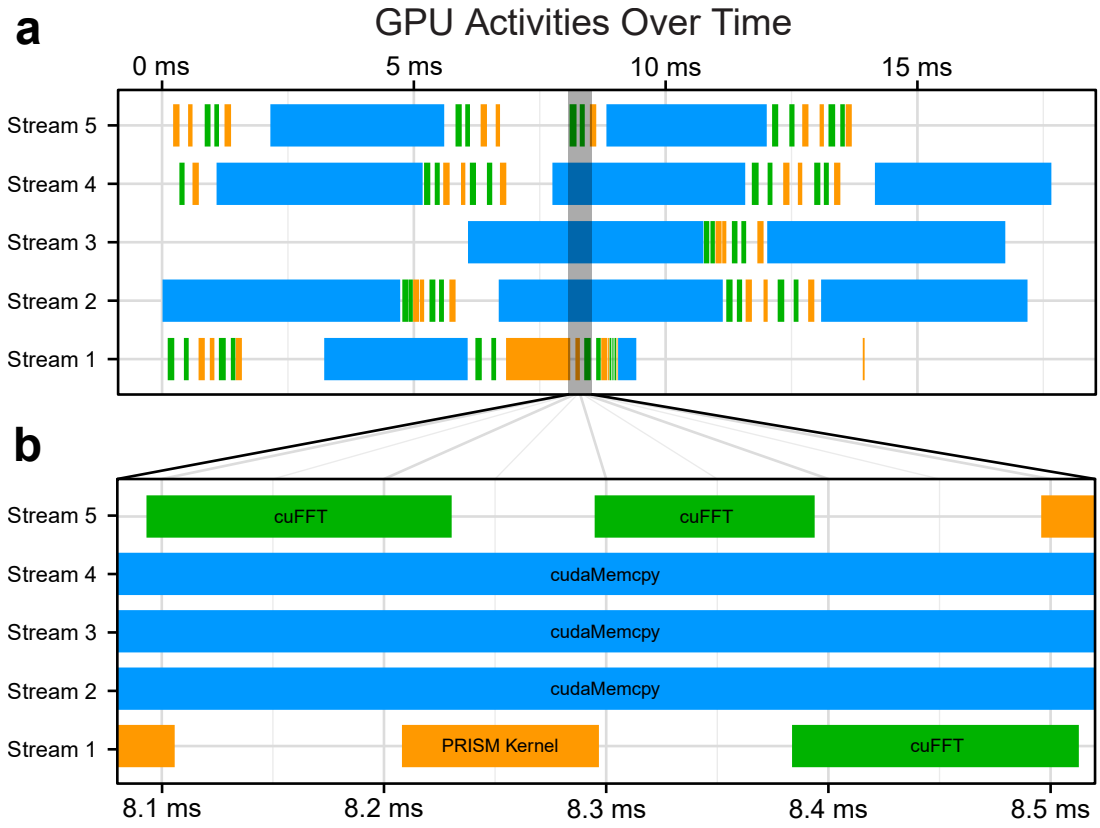

Figure A.3: **(a)** Sample profile of the GPU activities on a single NVIDIA GTX 1070 during a multislice simulation in streaming mode with **(b)** enlarged inset containing a window where computation is occurring on streams #1 and #5 while three separate arrays are simultaneously being copied on streams #2-4. (*Figure reprinted from [202]*)

To achieve maximum overlap of work, each CUDA-enabled routine in *Prismatic* begins with an initialization phase where relevant data on the host-side is copied into page-locked (also called "pinned") memory, which provides faster transfer times to the device and is necessary for asynchronous memory copying as the system can bypass internal staging steps that would be necessary for pageable

memory [240]. CUDA streams and data buffers are then allocated on each device and copied to asynchronously. Read-only memory is allocated once per device, and read/write memory is allocated once per stream. It is important to perform all memory allocations initially, as any later calls to *cudaMalloc* will implicitly force synchronization of the streams. Once the initialization phase is over, a host thread is spawned for each unique CUDA stream and begins to consume work.

A.3.2 Calculation of the Projected Potentials

Both PRISM and multislice require dividing the atomic coordinates into thin slices and computing the projected potential for each. The calculation details are described in Kirkland and require evaluation of modified Bessel functions of the second kind, which are computationally expensive [20]. This barrier is overcome by precomputing the result for each unique atomic species and assembling a lookup table. Each projected potential is calculated on a supersampled grid, integrated, and cached. The sample volume is then divided into slices, and the projected potential for each slice is computed on separate CPU threads using the cached potentials. In principle this step could be GPU accelerated, but even for a large sample with several hundred thousand atoms the computation time is on the order of seconds and is considered negligible.

A.3.3 PRISM Probe Simulations

Following calculation of the projected potential, the next step of PRISM is to compute the compact S-matrix. Each plane wave component is repeatedly transmitted and propagated through each slice of the potential until it has passed through the entire sample, at which point the complex-valued output wave is stored in real space to form a single layer of the compact S-matrix. This step of PRISM is highly analogous to multislice except whereas multislice requires

propagating/transmitting the entire probe simultaneously, in PRISM each initial Fourier component is propagated/transmitted individually. The advantage is that in PRISM this calculation must only be performed once per Fourier component for the entire calculation, while in multislice it must be repeated entirely at every probe position. Thus, in many sample geometries the PRISM algorithm can significantly out-perform multislice despite the overhead of the S-matrix calculation [233].

The propagation step requires a convolution operation which can be performed efficiently through use of the FFT. Our implementation uses the popular FFTW and cuFFT libraries for the CPU and GPU implementations, respectively [235, 236]. Both of these libraries support batch FFTs, whereby multiple Fourier transforms of the same size can be computed simultaneously. This allows for reuse of intermediate twiddle factors, resulting in a faster overall computation than performing individual transforms one-by-one at the expense of requiring a larger block of memory to hold the multiple arrays. *Prismatic* uses this batch FFT method with both PRISM and multislice, and thus each worker thread will actually propagate a number of plane waves or probes simultaneously. This number, called the *batch_size*, may be tuned by the user to potentially enhance performance at the cost of using additional memory, but sensible defaults are provided.

In the final step of PRISM, a 2D output is produced for each probe position by applying coefficients, one for each plane wave, to the elements of the compact S-matrix and summing along the dimension corresponding to the different plane waves. These coefficients correspond to Fourier phase shifts that scale and translate each plane wave to the relevant location on the sample in real space. The phase coefficients, which are different for each plane wave but constant for a given probe position, are precomputed and stored in global memory. Each threadblock on the device first reads the coefficients from global memory into shared memory, where they can be reused throughout the lifetime of the threadblock. Components

of the compact S-matrix for a given output wave position are then read from global memory, multiplied by the relevant coefficient, and stored in fast shared memory, where the remaining summation is performed. This parallel sum-reduction is performed using a number of well-established optimization techniques including reading multiple global values per thread, loop unrolling through template specialization, and foregoing of synchronization primitives when the calculation has been reduced to the single-warp level [241]. Once the realspace exit wave has been computed, the modulus squared of its FFT yields the calculation result at the detector plane.

A.3.4 Multislice Probe Simulations

The implementation of multislice is fairly straightforward. The initial probe is translated to the probe position of interest, and then is alternately transmitted and propagated through the sample. In practice this is accomplished by alternating forward and inverse Fourier transforms with an element-wise complex multiplication in between each with either the transmission or propagation functions. Upon propagation through the entire sample, the squared intensity of the Fourier transform of the exit wave provides the final result of the calculation at the detector plane for that probe position. For additional speed, the FFTs of many probes are computed simultaneously in batch mode. Thus in practice *batch_size* probes are transmitted, followed by a batch FFT, then propagated, followed by a batch inverse FFT, etc.

A.3.5 Streaming Data for Very Large Simulations

The preferred way to perform PRISM and multislice simulations is to transfer large data structures such as the projected potential array or the compact S-matrix to each GPU only once, where they can then be read from repeatedly

over the course of the calculation. However, this requires that the arrays fit into limited GPU memory. For simulations that are too large, we have implemented an asynchronous streaming version of both PRISM and multislice. Instead of allocating and transferring a single read-only copy of large arrays, buffers are allocated to each stream large enough to hold only the relevant subset of the data for the current step in the calculation, and the job itself triggers asynchronous streaming of the data it requires for the next step. For example, in the streaming implementation of multislice, each stream possesses a buffer to hold a single slice of the potential array, and after transmission through that slice the transfer of the next slice is requested. The use of asynchronous memory copies and CUDA streams permits the partial hiding of memory transfer latencies behind computation (Fig. A.3). Periodically, an individual stream must wait on data transfer before it can continue, but if another stream is ready to perform work the device is effectively kept busy. Doing so is critical for performance, as the amount of time needed to transfer data can become significant relative to the total calculation. By default, *Prismatic* uses an automatic setting to determine whether to use the single-transfer or streaming memory model whereby the input parameters are used to estimate how much memory will be consumed on the device, and if this estimate is too large compared with the available device memory then streaming mode is used. This estimation is conservative and is intended for convenience, but users can also forcibly set either memory mode.

A.3.6 Launch Configuration

All CUDA kernels are accompanied by a launch configuration that determines how the calculation will be carried out [240]. The launch configuration specifies the amount of shared memory needed, on which CUDA stream to execute the computation, and defines a 3D grid of threadblocks, each of which contains a 3D arrangement of CUDA threads. It is this arrangement of threads and threadblocks

that must be managed in software to perform the overall calculation. The choice of launch configuration can have a significant impact on the overall performance of a CUDA application as certain GPU resources, such as shared memory, are limited. If too many resources are consumed by individual threadblocks, the total number of blocks that run concurrently can be negatively affected, reducing overall concurrency. This complexity of CUDA cannot be overlooked in a performance-critical application, and we found that the speed difference in a suboptimal and well-tuned launch configuration could be as much as 2-3x.

In the reduction step of PRISM, there are several competing factors that must be considered when choosing a launch configuration. The first of these is the threadblock size. The compact S-matrix is arranged in memory such that the fastest changing dimension, considered to be the x-axis, lies along the direction of the different plane waves. Therefore to maximize memory coalescence, threadblocks are chosen to be as large as possible in the x-direction. Usually the result will be threadblocks that are effectively 1D, with $BlockSize_y$ and $BlockSize_z$ equal to one; however in cases where very few plane waves need to be computed the blocks may be extended in y and z to prevent underutilization of the device. To perform the reduction, two arrays of shared memory are used. The first is dynamically sized and contains as many elements as there are plane waves. This array is used to cache the phase shift coefficients to prevent unnecessary reads from global memory, which are slow. The second array has $BlockSize_x$*$BlockSize_y$*$BlockSize_z$ elements and is where the actual reduction is performed. Each block of threads steps through the array of phase shifts once and reads them into shared memory. Then the block contiguously steps through the elements of the compact S-matrix for a different exit-wave position at each y and z index, reading values from global memory, multiplying them by the associated coefficient, and accumulating them in the second shared memory array. Once all of the plane waves have been accessed, the remaining reduction occurs

quickly as all remaining operations occur in fast shared memory. Each block of threads will repeat this process for many exit-wave positions which allows efficient reuse of the phase coefficients from shared memory.

The parallel reduction is performed by repeatedly splitting each array in half and adding one half to the other until only one value remains. Consequently, if the launch configuration specifies too many threads along the x-direction, then many of them will become idle as the reduction proceeds, which wastes work. Conversely, choosing $BlockSize_x$ to be too small is problematic for shared memory usage, as the amount of shared memory per block for the phase coefficients is constant regardless of the block size. In this case, the amount of shared memory available will rapidly become the limiting factor to the achievable occupancy. A suitably balanced block size produces the best results.

The second critical component of the launch configuration is the number of blocks to launch. Each block globally reads the phase coefficients once and then reuses them, which favors using fewer blocks and having each compute more exit-wave positions. However, if too few blocks are launched the device may not reach full occupancy. The theoretically optimal solution would be to launch the minimal amount of blocks needed to saturate the device and no more.

Considering these many factors, *Prismatic* uses the following heuristic to choose a good launch configuration. At runtime, the properties of the available devices are queried, which includes the maximum number of threads per threadblock, the total amount of shared memory, and the total number of streaming multiprocessors. $BlockSize_x$ is chosen to be either the largest power of two smaller than the number of plane waves or the maximum number of threads per block, whichever is smaller. The total number of threadblocks that can run concurrently on a single streaming multiprocessor is then estimated using $BlockSize_x$, the limiting number of threads per block, and the limiting number of threadblocks per streaming multiprocessor. The total number of threadblocks across the en-

tire device is then estimated as this number times the total number of streaming multiprocessors, and then the grid dimensions of the launch configuration are set to create three times this many blocks, where the factor of three is a fudge factor that we found produces better results.

A.4 Benchmarks

A.4.1 Algorithm Comparison

A total of four primary algorithms are implemented *Prismatic*, as there are optimized CPU and GPU implementations of both PRISM and multislice simulation. To visualize the performance of the different algorithms, we performed a number of benchmarking simulations spanning a range of sample thicknesses, sizes, and with varying degrees of sampling. Using the average density of amorphous carbon, an atomic model corresponding to a 100x100x100 Å carbon cell was constructed and used for image simulation with various settings for slice thickness and pixel sampling. The results of this analysis are summarized in Fig. A.4. These benchmarks are plotted as a function of the maximum scattering angle $q_{\max}$, which varies inversely to the pixel size.

The difference in computation time t shown in Fig. A.4 between traditional CPU multislice and GPU PRISM is stark, approximately four orders of magnitude for the "fast" setting where $f = 16$, and still more than a factor of 500 for the more accurate case of $f = 4$. For both PRISM and multislice, the addition of GPU acceleration increases speed by at least an order of magnitude. Note that as the thickness of the slices is decreased, the relative gap between PRISM and multislice grows, as probe calculation in PRISM does not require additional propagation through the sample. We have also fit trendline curves of the form

$$t = A + B\,{q_{\max}}^{n}, \tag{A.3}$$

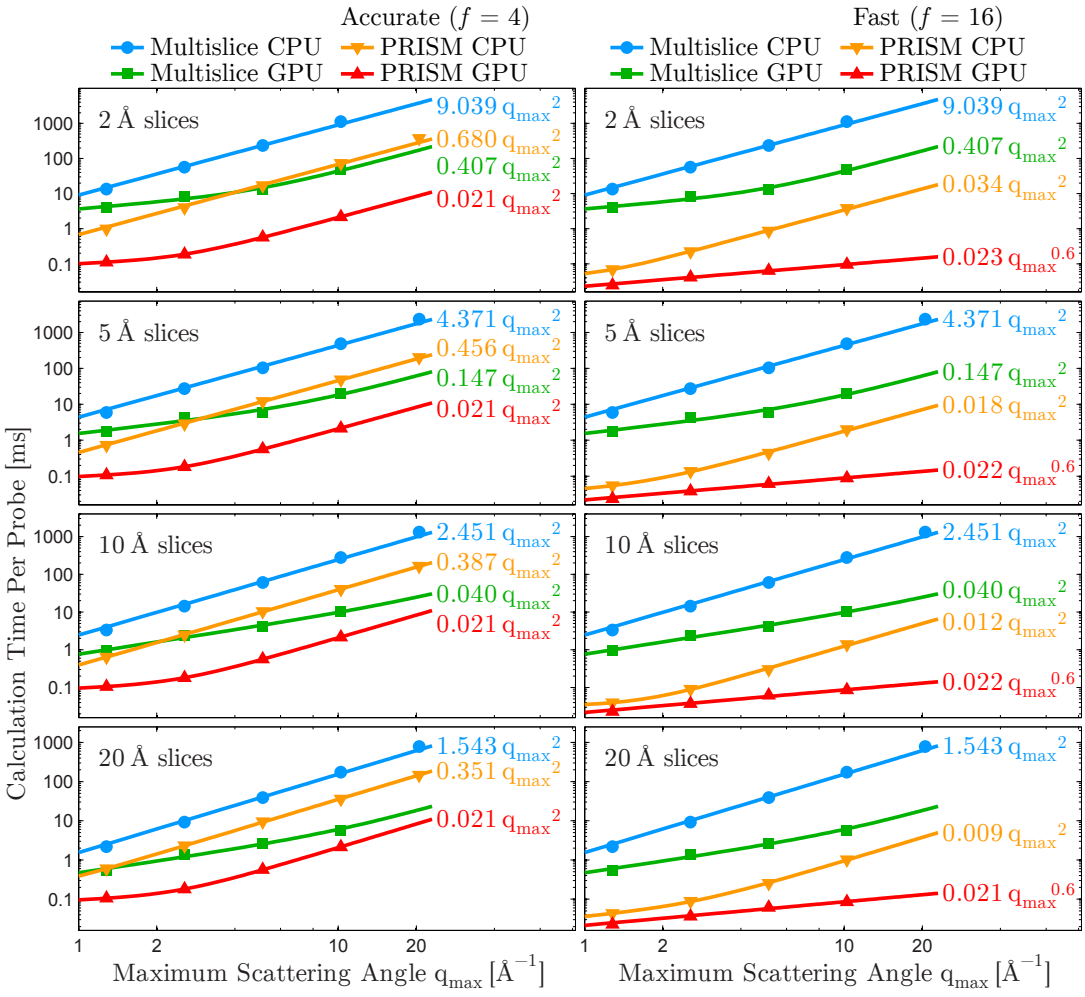

Figure A.4: Comparison of the CPU/GPU implementations of the PRISM and multislice algorithms described in this work. A 100x100x100 Å amorphous carbon cell was divided slices of varying thickness and sampled with increasingly small pixels in real space corresponding to digitized probes of array size 256x256, 512x512, 1024x1024, and 2048x2048, respectively. Two different PRISM simulations are shown, a more accurate case where the interpolation factor $f = 4$ (left), and a faster case with $f = 16$ (right). The multislice simulation is the same for both columns. Power laws were fit of the form $A + B\,q_{\max}{}^{n}$ where possible. The asymptotic power laws for higher scattering angles are shown on the right of each curve. (*Figure reprinted from [202]*)

where A and B are prefactors and n is the asymptotic power law for high scattering angles. We observed that most of the simulation types approximately approach $n = 2$, which is unsurprising for both PRISM and multislice. The limiting operation in PRISM is matrix-scalar multiplication, which depends on the array size and varies as ${q_{\max}}^2$. For multislice the computation is a combination of multiplication operations and FFTs, and the theoretical $\mathcal{O}(n \log n)$ scaling of the latter is only slightly larger than 2 and thus the trendline is an approximate lower bound. The only cases that fall significantly outside the $n = 2$ regime were the multislice GPU simulations with the largest slice separation (20 Å) and the "fast" PRISM GPU simulations where $f = 16$. These calculations are sufficiently fast that the relatively small overhead required to compute the projected potential slices, allocate data, etc., is actually a significant portion of the calculation, resulting in scaling better than ${q_{\max}}^2$. For the $f = 16$ PRISM case, we observed approximately ${q_{\max}}^{0.6}$ scaling, which translates into sub-millisecond calculation times per probe even with small pixel sizes and slice thicknesses.

To avoid unnecessarily long computation times for the many simulations, particularly multislice, different numbers of probe positions were calculated for each algorithm, and thus we report the benchmark as time per probe. Provided enough probe positions are calculated to obviate overhead of computing the projected potential and setting up the remainder of the calculation, there is a linear relationship between the number of probe positions calculated and the calculation time for all of the algorithms, and computing more probes will not change the time per probe significantly. Here this overhead is only on the order of 10 seconds or fewer, and the reported results were obtained by computing 128x128 probes for PRISM CPU and multislice CPU, 512x512 for multislice GPU, and 2048x2048 for PRISM GPU. All of these calculations used the single-transfer memory implementations and were run on compute nodes with dual Intel Xeon E5-2650 processors, four Tesla K20 GPUs, and 64GB RAM from the VULCAN cluster within the Lawrence

Berkeley National Laboratory Supercluster.

A.4.2 Hardware Scaling

Modern high performance computing is dominated by parallelization. At the time of this writing virtually all desktop CPUs contain at least four cores, and high end server CPUs can have as many as twenty or more [242]. Even mobile phones have begun to routinely ship with multicore processors [243]. In addition to powerful CPUs, GPUs and other types of coprocessors such as the Xeon Phi [244] can be used to accelerate parallel algorithms. It therefore is becoming increasingly important to write parallel software that fully utilizes the available computing resources.

To demonstrate how the algorithms implemented in *Prismatic* scale with hardware, we performed the following simulation. Simulated images of a 100x100x100 Å amorphous carbon cell were produced with both PRISM and multislice using 5 Å thick slices, pixel size 0.1 Å, and 80 keV electrons. This simulation was repeated using varying numbers of CPU threads and GPUs. As before, a varying number of probes was computed for each algorithm, specifically 2048x2048 for GPU PRISM, 512x512 for CPU PRISM and GPU multislice, and 64x64 for CPU multislice. This simulation utilized the same 4-GPU VULCAN nodes described previously. The results of this simulation are summarized in Fig. A.5.

The ideal behavior for the CPU-only codes would be to scale as $1/x$ with the number of CPU cores utilized such that doubling the number of cores also approximately doubles the calculation speed. Provided that the number of CPU threads spawned is not greater than the number of cores, the number of CPU threads can effectively be considered the number of CPU cores utilized, and this benchmark indicates that both CPU-only PRISM and multislice possess close to ideal scaling behavior with number of CPU cores available.

The addition of a single GPU improves both algorithms by approximately a factor of 8 in this case, but in general the relative improvement varies depending on the quality and number of the CPUs vs GPUs. The addition of a second GPU improves the calculation speed by a further factor of 1.8-1.9 with 14 threads, and doubling the number of GPUs to four total improves again by a similar factor. The reason that this factor is less than two is because the CPU is doing a nontrivial amount of work alongside the GPU. This claim is supported by the observation that when only using two threads the relative performance increase is almost exactly a factor of two when doubling the number of GPUs. We conclude that our implementations of both algorithms scale very well with available hardware, and potential users should be confident that investing in additional hardware, particularly GPUs, will benefit them accordingly.

A.4.3 Data Streaming/Single-Transfer Benchmark

For both PRISM and multislice, *Prismatic* implements two different memory models, a single-transfer method where all data is copied to the GPU a single time before the main computation begins, and a streaming mode where asynchronous copying of the required data is triggered across multiple CUDA streams as it is needed throughout the computation. Streaming mode reduces the peak memory required on the device at the cost of redundant copies; however, the computational cost of this extra copying can be partially alleviated by hiding the transfer latency behind compute kernels and other copies (A.3). To compare the implementations of these two memory models in *Prismatic*, a number of amorphous carbon cells of increasing sizes were used as input to simulations using 80 keV electrons, 20 mrad probe convergence semi-angle, 0.1 Å pixel size, 4 Å slice thickness, and 0.4 Å probe steps. Across a range of simulation cell sizes the computation time of the streaming vs. single-transfer versions of each code are extremely similar while the peak memory may be reduced by an order of magnitude or more (Fig. A.6).

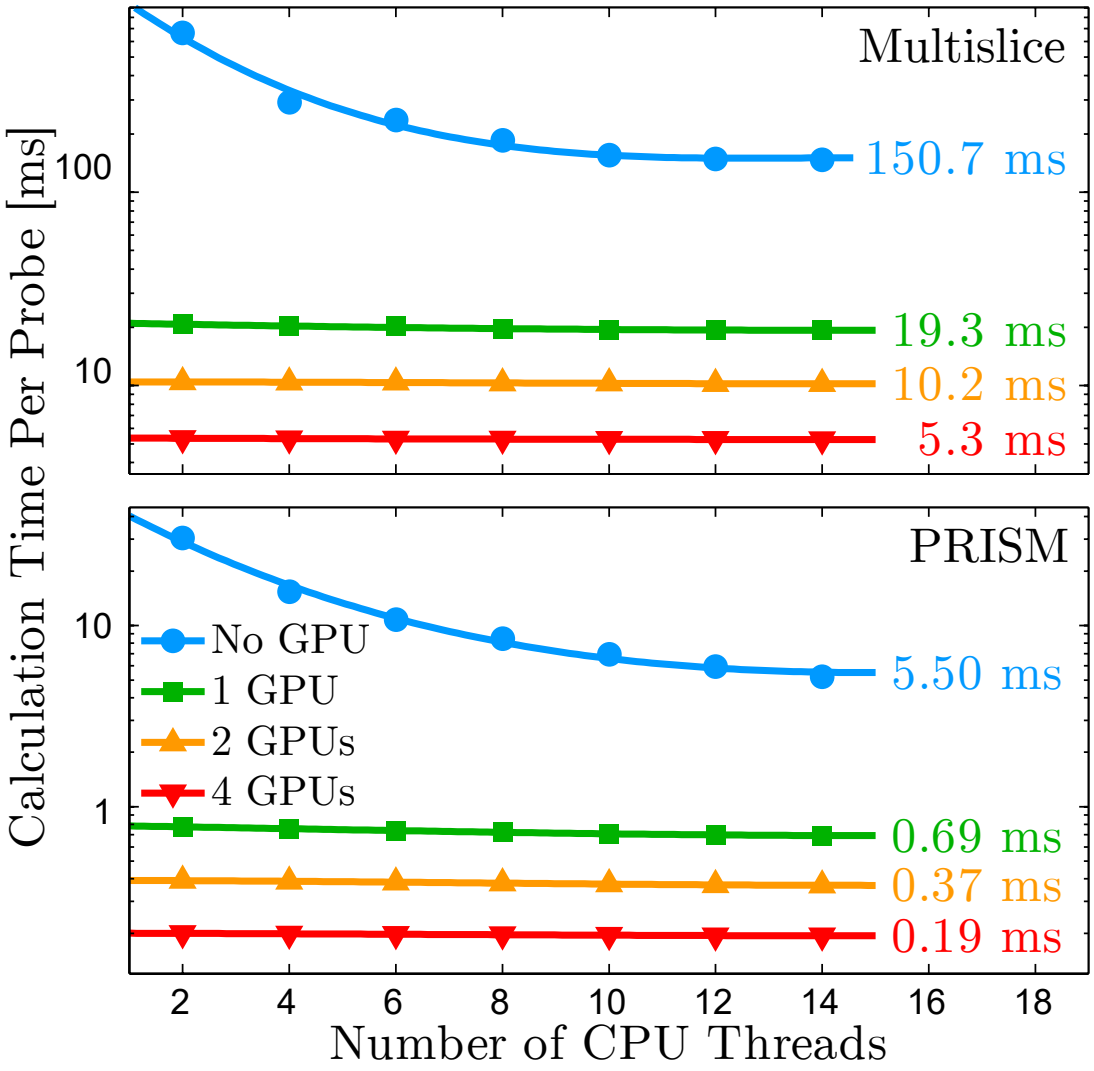

Figure A.5: Comparison of the implementations of multislice and PRISM for varying combinations of CPU threads and GPUs. The simulation was performed on a 100x100x100 Å amorphous carbon cell with 5 Å thick slices, and 0.1 Å pixel size. All simulations were performed on compute nodes with dual Intel Xeon E5-2650 processors, four Tesla K20 GPUs, and 64GB RAM. Calculation time of rightmost data point is labeled for all curves. (*Figure reprinted from [202]*)

For the streaming calculations, memory copy operations may become significant relative to the computational work (Fig. A.3);however, this can be alleviated by achieving multi-stream concurrency.

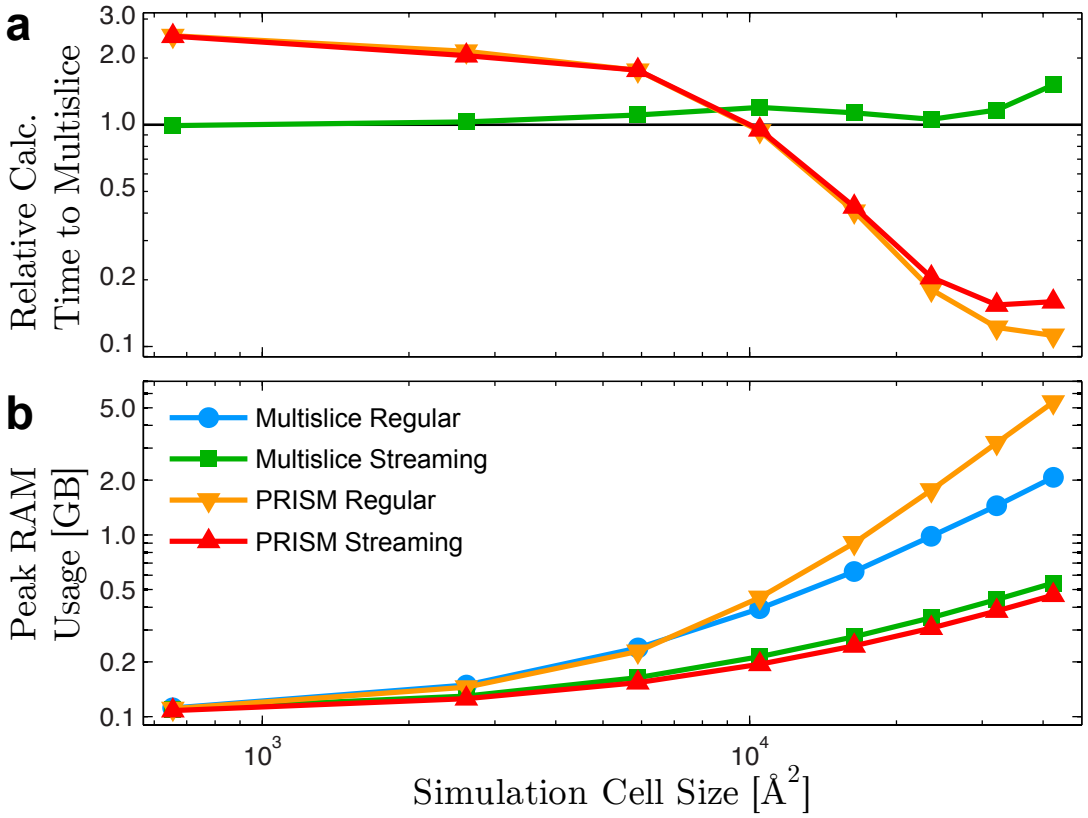

Figure A.6: Comparison of **(a)** relative performance and **(b)** peak memory consumption for single transfer and streaming implementations of PRISM and multislice. (*Figure reprinted from [202]*)

A.4.4 Comparison to existing methods

All previous benchmarks in this work have measured the speed of the various algorithms included in *Prismatic* against each other; however, relative metrics are largely meaningless without an external reference both in terms of overall speed and resulting image quality. To this end, we also performed STEM simulations of significant size and compare the results produced by the algorithms in *Prismatic*

and the popular package *computem* [20, 215].

We have chosen a simulation cell typical of those used in structural atomic-resolution STEM studies, a complex RuddlesdenPopper (RP) layered oxide. The RP structure we used contains 9 pseudo-cubic unit cells of perovskite strontium titanate structure, with two stacking defects every 4.5 1x1 cells that modify the composition and atomic coordinates. The atomic coordinates of this cell were refined using Density Functional Theory and were used for very-large-scale STEM image simulations [245]. This 9x1x1 unit cell was tiled 4x36x25 times resulting in final sample approximately 14 x 14 nm in-plane and 10 nm thick, containing roughly 1.4 million atoms.

Simulations were performed with multislice as implemented in *computem* (specifically using the *autostem* module), multislice in *Prismatic*, and the PRISM method with f values of 4, 8 and 16 using 80 keV electrons, 1024 x 1024 pixel sampling, 20 mrad probe convergence semi-angle, and 5 Å thick potential slices. A total of 720x720 evenly spaced probes were computed for each simulation, and a total of 32 frozen phonon configurations were averaged to produce the final images, which are summarized in Fig. A.7. The PRISM algorithms were run on the VULCAN GPU nodes while *computem* simulations utilized better VULCAN CPU nodes with dual Intel Xeon E5-2670v2 CPUs and 64GB RAM.

The mean computation time per frozen phonon for the *computem* simulations was 709.8 minutes resulting in a total computation time of 15.8 days. The use of our GPU multislice code here provides an acceleration of about 28x, reducing the computation from more than two weeks to just over one day. The PRISM $f = 4$ simulation is almost indistinguishable from the multislice results, and gives a 2.7x speed up over our GPU multislice simulation. For the $f = 8$ PRISM simulation, some intensity differences are visible in the two bright field images, but the relative contrast of all atomic sites is still correct. This simulation required just over an hour, providing a speedup of 25X relative to our GPU multislice simulation. The

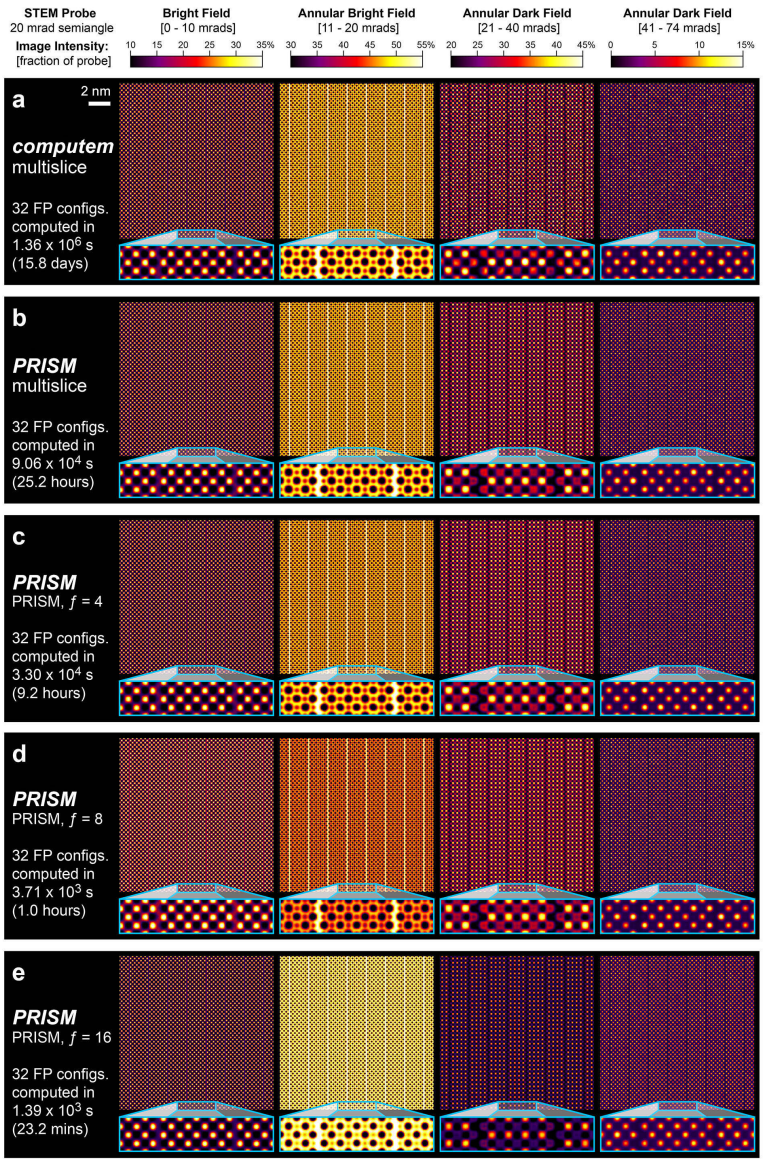

Figure A.7: Comparison of simulation results produced by *computem* and *Prismatic*. The sample is composed of 36x36x25 pseudocubic perovskite unit cells, and images were simulated using 80 keV electrons, a 20 mrad probe convergence semi-angle, 0 Å defocus, and 1024x1024 pixel sampling for the probe and projected potential. A total of 720x720 probe positions were computed and the final images are an average over 32 frozen phonon configurations. Separate PRISM simulations were performed with interpolation factors 4, 8, and 16. (*Figure reprinted from [202]*)

$f = 16$ PRISM result show substantial intensity deviations from the ideal result, but require just 43 seconds per frozen phonon configuration. The total difference in acceleration from CPU multislice to the fastest PRISM simulation shown in Fig. A.7 is just under three orders of magnitude. Ultimately, the users purpose dictates what balance of speed and accuracy is appropriate, but the important point is that calculations that previously required days or weeks on a computer cluster may now be performed on a single workstation in a fraction of the time. ‘

A.5 Application to atomic electron tomography

One potential application of STEM image simulations is atomic electron tomography (AET) experiments. In previous studies, we have used multislice simulations to validate the tomographic reconstructions, and estimate both the position and chemical identification errors [1, 3]. However, the 3D reconstruction algorithm assumes that the projection images are linearly related to the potential of the reconstruction. This assumption was sufficient for atomic resolution tomographic reconstruction, but the measured intensity has some non-linear dependence on the atomic potentials, due to effects such as exponential decrease of electrons in the unscattered STEM probe, channeling effects along atomic columns, coherent diffraction at low scattering angles and other related effects [246–250].

One potentially important application of STEM image simulations is AET experiments. One of the ADF-STEM images from an atomic-resolution tilt series of a FePt nanoparticle [3] is shown in Fig. A.8a, with the corresponding linear projection from the 3D reconstruction shown in Fig. A.8b. In this study and others, we have used multislice simulations to validate the tomographic reconstructions and estimate both the position and chemical identification errors [1, 3]. One such multislice simulation is given in Fig. A.8c. This simulation was performed at 300 kV using a 30 mrad STEM probe, with a simulation pixel size of 0.0619 Å and

a spacing between adjacent probes of 0.3725 Å. The image results shown are for 16 frozen phonon configurations using a 41159 mrad annular dark field detector. This experimental dataset includes some postprocessing and was obtained freely online [3].

The 3D reconstruction algorithm we have used, GENeralized Fourier Iterative REconstruction (GENFIRE), assumes that the projection images are linearly related to the potential of the reconstruction [3, 28]. This assumption was sufficient for atomic-resolution tomographic reconstruction, but the measured intensity has some non-linear dependence on the atomic potentials, due to effects such as exponential decrease of electrons in the unscattered STEM probe, channeling effects along atomic columns, coherent diffraction at low scattering angles, and other related effects [213, 246–250]. These effects can be seen in the differences between the images shown in Fig. A.8b, c. The multislice simulation image shows sharper atomic columns, likely due to the channeling effect along atomic columns that are aligned close to the beam direction [248]. Additionally, there are mean intensity differences between the center part of the particle (thickest region) and the regions closed to the surfaces in projection (thinnest regions). Including these dynamical scattering effects in the reconstruction algorithm would increase the accuracy of the reconstruction.

However, Fig. A.8h shows that the computation time for the multislice simulation is prohibitively high. Even using the Prismatic GPU code, each frozen phonon configuration for multislice require almost 7 hours. Using 16 configurations and simulating all 65 projection angles would require months of simulation time, or massively parallel simulation on a super cluster. An alternative is to use the PRISM algorithm for the image simulations, shown in Fig. A.8d, e and f for interpolation factors of $f = 8, 16 and 32$, respectively. Fig. A.8g shows the relative errors of Fig. A.8bf, where the error is defined by the root-mean-square of the intensity difference with the experimental image in Fig. A.8a, divided by the

root-mean-square of the experimental image. Unsurprisingly, the linear projection shows the lowest error since it was calculated directly from the 3D reconstruction built using the experimental data. The multislice and PRISM $f = 8$ and $f = 16$ simulations show essentially the same errors within the noise level of the experiment. The PRISM $f = 32$ has a higher error, and obvious image artifacts are visible in Fig. A.8f. Thus, we conclude that using an interpolation factor $f = 16$ produces an image of sufficient accuracy. This calculation required only 90 s per frozen phonon calculation, and therefore computing 16 configurations for all 65 tilt angles would require only 26 h. One could therefore imagine integrating this simulation routine into the final few tomography reconstruction iterations to account for dynamical scattering effects and to improve the reconstruction quality.

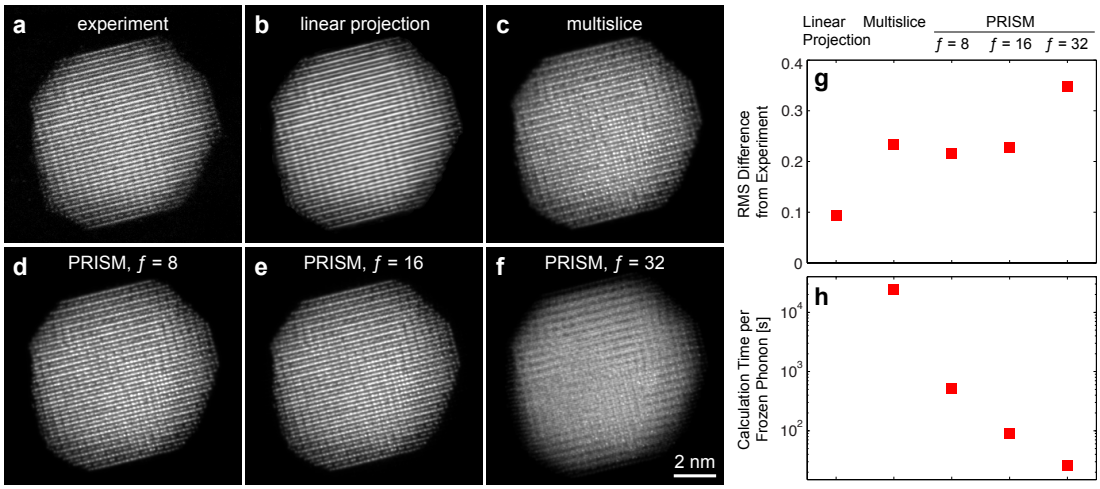

Figure A.8: Images from one projection of an atomic electron tomography tilt series, from **(a)** experiment, **(b)** linear projection of the reconstruction, **(c)** multislice simulation, and (d)-**(f)** PRISM simulations for $f = 8$, 16, and 32 respectively. (*Figure reprinted from [202]*)

A.6 Conclusion

We have presented *Prismatic*, an asynchronous, streaming GPU implementation of the PRISM and multislice algorithms for image formation in scanning transmission electron microscopy. Both algorithms were described in detail as well as our approach to implementing them in a parallel framework. Our benchmarks demonstrate that this software may be used to simulate STEM images up to several orders of magnitude faster than using traditional methods, allowing users to simulate complex systems on a GPU workstation without the need for a computer cluster. *Prismatic* is freely available as an open-source C++/CUDA package with a graphical interface that contains convenience features such as allowing users to interactively view the projected potential slices, compute/compare individual probe positions with both PRISM and multislice, and dynamically adjust positions of virtual detectors. A command line interface is also provided. We hope that the speed of this code as well as the convenience of the user interface will have significant impact for users in the EM community.

APPENDIX B

Quantitative Single-Shot 3D Coherent Diffraction Imaging of Core-Shell Nanocubes with Elemental Specificity

We report 3D coherent diffractive imaging (CDI) of Au/Pd core-shell nanoparticles with 6.1nm spatial resolution with elemental specificity. We measured single-shot diffraction patterns of the nanoparticles using intense X-ray free electron laser pulses. By exploiting the curvature of the Ewald sphere and the symmetry of the nanoparticle, we reconstructed the 3D electron density of 34 core-shell structures from these diffraction patterns. To extract 3D structural information beyond the diffraction signal, we implemented a super-resolution technique by taking advantage of CDIs quantitative reconstruction capabilities. We used high-resolution model fitting to determine the Au core size and the Pd shell thickness to be 65.0 $\pm$ 1.0nm and 4.0 $\pm$ 0.5nm, respectively. We also identified the 3D elemental distribution inside the nanoparticles with an accuracy of 3%. To further examine the model fitting procedure, we simulated noisy diffraction patterns from a Au/Pd core-shell model and a solid Au model and confirmed the validity of the method. We anticipate this super-resolution CDI method can be generally used for quantitative 3D imaging of symmetrical nanostructures with elemental specificity.

B.1 Introduction

Core-shell nanoparticles exhibit unique electronic, chemical, catalytic and optical properties that have found applications across several disciplines [251–254]. Conventional methods to characterize these nanoparticles rely on electron microscopy, scanning probe microscopy, X-ray diffraction, scattering and spectroscopic techniques [251–254]. Although atomic electron tomography has recently been used to determine the 3D structure of nanoparticles at the single atom level, the sample has to be thin enough to mitigate the dynamical scattering effect [2, 3, 29]. Scanning probe microscopy is limited to studies of surface structures and X-ray diffraction and scattering methods only provide average structural information [251, 253, 254]. In contrast, CDI can be used to determine the 3D internal electron density of thick samples at high resolution [70, 255]. Following the first experimental demonstration in 1999 [64], a number of CDI methods have been developed and applied to image a broad range of samples in physics, chemistry, materials science, nanoscience and biology [10, 67, 68, 71, 111, 114, 115, 119, 124, 141, 149, 159, 163, 256–261].

With the advent of X-ray free electron lasers (XFELs) that produce extremely intense and short X-ray pulses [70, 262, 263], CDI has opened the door for high-resolution imaging of both physical and biological specimens based on the diffraction-before-destruction scheme [40, 264]. However, because an intense XFEL pulse destroys a specimen after one exposure, it would be desirable to find a way to obtain 3D structure information from a single X-ray pulse. One method to achieve 3D structure determination from a single sample orientation is the use of the curvature of Ewald sphere and additional constraints such as symmetry and sparsity [81, 265–269]. Here, we implemented a super-resolution CDI technique to extract 3D structural information of core-shell nanoparticles beyond the diffraction signal. We reconstructed the 3D electron density of individual Au/Pd core-shell

nanoparticles from single-shot diffraction patterns with 6.1 nm resolution. By exploiting CDIs quantitative reconstruction, we used high-resolution model fitting to determine the size of the Au core and the thickness of the Pd shell to be 65.0 ± 1.0 nm and 4.0 ± 0.5 nm, respectively. We quantified the 3D elemental distribution inside the nanoparticle with an accuracy better than 3%. Finally, by implementing a semi-automated data analysis and 3D reconstruction pipeline, we established a general method for high-throughput, quantitative characterization of symmetrical nanoparticles.

B.2 Results

B.2.1 XFEL experiment and 3D reconstruction of core-shell nanoparticles

Au/Pd core-shell nanoparticles were synthesized by a seed mediated growth method from soluble precursors [271]. Au nanoparticles with truncated cubic shapes were prepared first as the cores. After the epitaxial growth of a Pd shell on the cubic Au core, the composite nanoparticles adopted a perfect cubic shape. SEM and TEM images shows a monodisperse shape and size distribution of the nanoparticles (Fig. B.1 insets). The formation of Au/Pd core-shell structure was also implicated by the alternating bright and dark fringes in the TEM image caused by the superposition of two misfit crystalline lattices in a core-shell construction. The XFEL experiment was conducted using the SPring-8 Angstrom Compact Free Electron Laser [263].

Fig. B.1 shows the schematic layout of the single-shot 3D diffractive imaging experiment. X-ray pulses with an energy of 6 keV and a repetition rate of 10 Hz were focused to a 1.5 m spot by a pair of Kirkpatrick-Baez (K-B) mirror. Each pulse contained ~10^{11} photons with a pulse duration of 5-6 fs (Fig. B.2). Nanoparticles were deposited onto a 100-nm-thick Si_3N_4 membrane grid and inserted into

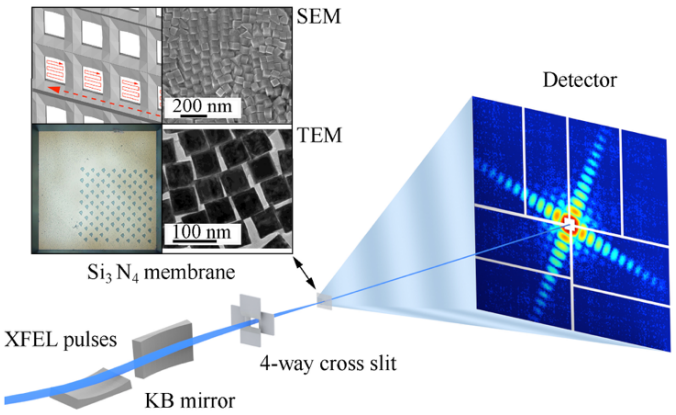

Figure B.1: Schematic layout of the single-shot 3D diffractive imaging set-up. XFEL pulses with an energy of 6 keV and a pulse duration of 5-6 fs were focused to a 1.5 m spot by a pair of K-B mirrors. A four-way cross slit was used to eliminate the parasitic scattering from the mirrors. Au/Pd core-shell nanoparticles with a monodisperse shape and size distribution (insets) were supported on a 100-nm-thick Si3N4 membrane grid and raster scanned relative to the focused beam. Each intense X-ray pulse produced a single-shot diffraction pattern, recorded by an octal multi-port charge-coupled device. A small hole was created on the Si3N4 membrane after a single exposure (insets). (*Figure reprinted from [270]*)

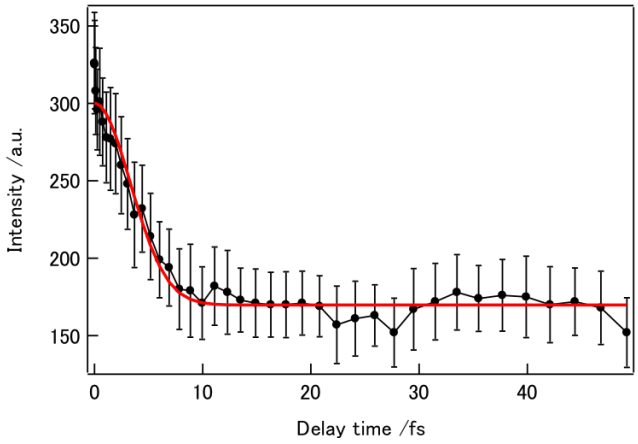

Figure B.2: Intensity correlation measurements of the pulse duration of SACLA at 10 keV using an autocorrelation technique64. Gaussian fitting of the intensity correlation curve gave a full width of half maximum (FWHM) of 7.8 ± 0.3 fs. After considering a deconvolution factor, the pulse duration was estimated to be 5.5 fs. The autocorrelationtechnique was also applied at 6 keV, resulting in an estimated pulse duration of ~5 fs (FWHM)65. Based on these experimental measurements, we concluded that the pulse duration in our experiment is ~5-6 fs (FWHM). (*Figure reprinted from [270]*)

a multi-application X-ray imaging chamber where the sample was scanned relative to the X-ray pulses [152]. Single-shot X-ray diffraction patterns were measured by an octal multi-port charge-coupled device [272]. The nanoparticles were destroyed after the impinging of X-ray pulses, leaving small holes on the Si_3N_4 membrane (Fig. B.1 inset). A total of 39,151 diffraction patterns were acquired consisting of no, partial, single, and multiple hits. Single-hits were separated from these patterns based on a threshold of the average diffraction intensity. A good hit rate for single-shot diffraction pattern is around a few percent. From the hit candidates, we selected a subset of 34 diffraction patterns for further analysis.

The 34 diffraction patterns were processed and reconstructed by using a semi-automated 3D data analysis pipeline, shown in Fig. B.3. From each diffraction pattern, the background was subtracted based on the most recently available background exposure. An additional flat background subtraction was required, the value of which was determined by first smoothing and thresholding each pattern to determine the background region. The final subtracted value was determined by the average nonnegative pixel intensity in the background region multiplied by a single scaling factor, whose value was optimized based upon the quality of the resulting reconstructions. The center of each diffraction pattern was determined based on the centro-symmetry of the diffraction intensity at the low spatial frequency. Since the diffraction patterns have larger oversampling ratios [76], each pattern was binned by 99 pixels to enhance the signal-to-noise ratio [273]. Figure B.4 shows the 34 processed single-shot diffraction patterns, in which the diffraction signal is limited by the size of the detector. The orientation of each single-shot diffraction pattern can in principle be determined by the self-common arc method [267]. The 34 diffraction patterns in this experiment were oriented close to the four-fold symmetry axis as the majority of nanocubes sit flat on the surface of Si_3N_4 membranes (Fig. B.1 insets). This allowed us to develop a simpler approach to refine the orientation of each diffraction pattern. We first estimated

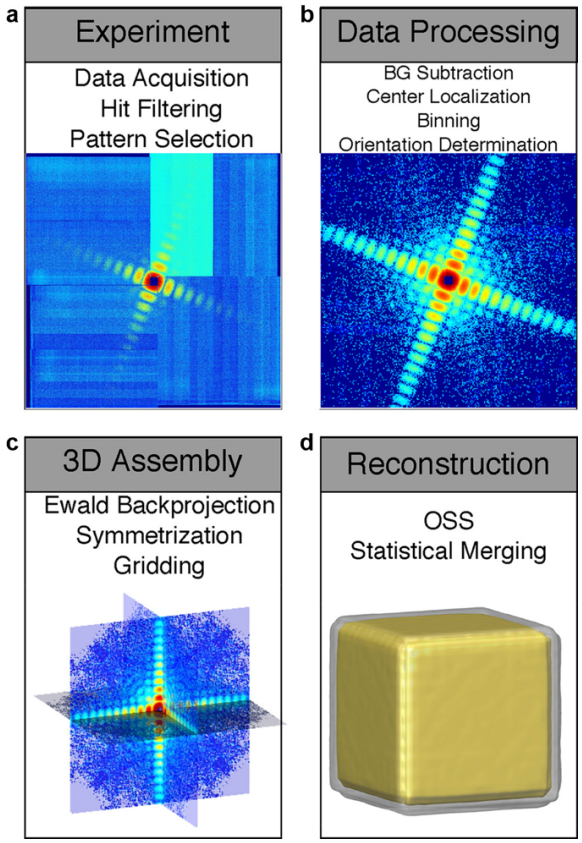

Figure B.3: Semi-automated data analysis and 3D reconstruction pipeline. **(a)**. A large number of diffraction patterns were experimentally collected consisting of no, partial, single, and multiple hits by XFEL pulses. High-quality single-hit diffraction patterns were selected from these patterns. The different colors in the pattern are due to the difference of the read-out noise of the detector segments. **(b)**. After background subtraction and center localization, each diffraction pattern was binned by 99 pixels to enhance the signal-to-noise ratio and the orientation of the pattern was determined. **(c)**. By taking advantage of the curvature of the Ewald sphere and symmetry intrinsic to the nanoparticle, a single-shot diffraction pattern was used to produce a 3D Cartesian grid of the Fourier magnitudes by a gridding method. **(d)**. The 3D phase retrieval was performed by the OSS algorithm. Among 1,000 independent reconstructions, the top 10% with the smallest R-factors were averaged to obtain a final 3D reconstruction for each single-shot diffraction pattern. (*Figure reprinted from [270]*)

the size of a nanocube based on the speckle size and experimental parameters. We then slightly changed the orientation of the nanocube and calculated the corresponding diffraction pattern. By minimizing the difference between the calculated and measured diffraction patterns, we determined the orientation of each diffraction pattern with an angular precision of ~0.5°.

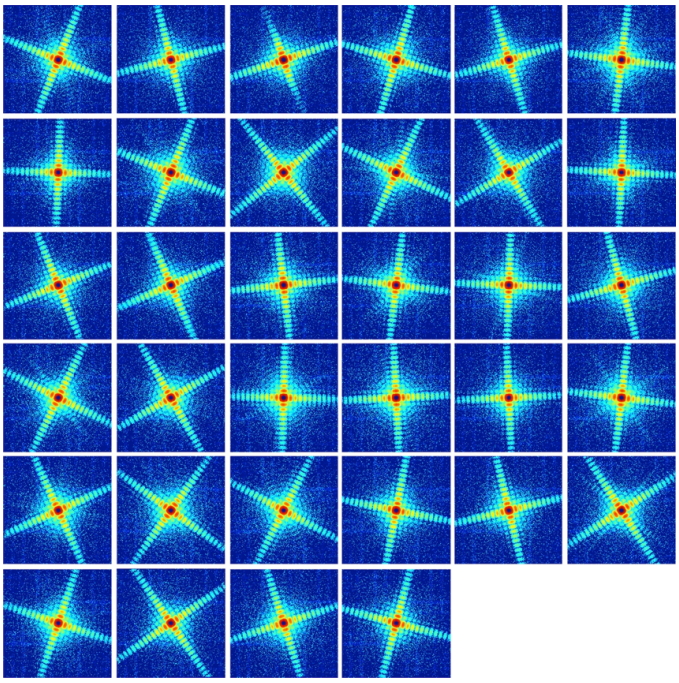

Figure B.4: 34 processed single-shot diffraction patterns, each of which was measured by impinging a very intense and short XFEL pulse on a Au/Pd core-shell nanocube. The orientation of these selected patterns is close to the four-fold symmetry axis as the majority of nanocubes sit flat on the surface of a Si_3N_4 membrane. (*Figure reprinted from [270]*)

Each diffraction pattern was then projected onto the surface of the Ewald sphere [81]. By taking into account of the curvature of the Ewald sphere and the 48 octahedral symmetry operations, a 3D Cartesian grid of the Fourier magnitudes

was assembled by the following interpolation approach,

$$|F_{obs}(\vec{k})| = \frac{\sum_i \frac{|F(\vec{k_i})|W(\vec{k_i})}{\Delta\Omega_i|\vec{k_i}-\vec{k}|}}{\sum_i \frac{W(\vec{k_i})}{|\vec{k_i}-\vec{k}|}} \tag{B.1}$$

$$W(\vec{k_i}) = \begin{cases} 1, & \frac{|\vec{k_i}-\vec{k}|}{\Delta p} < d_c. \\ 0, & \frac{|\vec{k_i}-\vec{k}|}{\Delta p} \geq d_c. \end{cases} \tag{B.2}$$

where $|F_{obs}(\vec{k})|$ is the interpolated Fourier magnitudes on the 3D Cartesian grid point $(\vec{k})$, $|F(\vec{k_i})|$ is the measured Fourier magnitudes of the i^{th} pixel projected onto the surface of the Ewald sphere, $W(\vec{k_i})$ represents a spherical interpolation kernel of radius d_c (where $d_c = 0.7$ voxels in this case), $\Delta\Omega_i$ is the solid angle subtended by the i^{th} pixel of the detector and Δp is the pixel size in reciprocal space. When the diffraction pattern has a large oversampling ratio and the Fourier magnitudes change smoothly [76], this interpolation approach is computationally efficient and accurate. Using Eq. (B.1), we produced a 3D Cartesian grid of the Fourier magnitudes for each single-shot diffraction pattern. A fraction of the grid points were filled in by the measured data and the remaining points were set as undefined. The phase retrieval was carried out by the oversampling smoothness (OSS) algorithm [167]. A total of 1,000 independent, randomly seeded 3D reconstructions were performed for each 3D grid of the Fourier magnitudes. Each reconstruction consisted of 1,000 iterations of OSS with ten progressive filters, positivity constraint, and a loose support. The algorithm iterated between real and reciprocal space. The positivity and support constraints were applied in real space and the measured grid points were enforced in reciprocal space, while the undefined points were iteratively determined by the algorithm. An R-factor, defined as the sum of difference between measured and calculated Fourier magnitudes normalized by the sum of measured Fourier magnitudes, was used to monitor the convergence of the iterative algorithm. After 1,000 iteration, the majority of 1,000

independent reconstructions had converged and the top 10% with the smallest R-factors were averaged to obtain a final 3D reconstruction. The Phase Retrieval Transfer Function (PRTF) was also monitored across reconstructions to further validate quality (Fig. B.5).

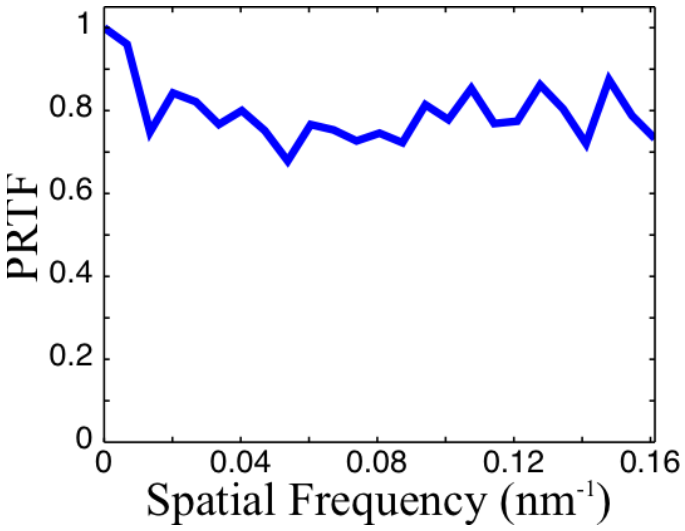

Figure B.5: Average Phase Retrieval Transfer Function (PRTF) across all of the multiple experimental reconstructions for all 34 diffraction patterns. (*Figure reprinted from [270]*)

Because the quantity of data obtained during an XFEL experiment is so high, we have implemented a semi-automated pipeline for diffraction pattern selection, data analysis and 3D reconstruction (Fig. B.3), allowing the visualization of the final 3D reconstructions during the experiment. By using this semi-automated pipeline, we obtained the final reconstructions of the 34 single-shot diffraction patterns (Fig. B.7). Figure B.6a show the iso-surface renderings of a representative final reconstruction, in which the core and shell structures are clearly visible. To quantify the resolution, we calculated the Fourier shell correlation (FSC) between the final reconstructions of different single-shot diffraction patterns, which has been widely used to estimate the resolution in single-particle cryo-electron microscopy [19]. Based on the criterion of FSC = 0.5, we estimated a 3D reso-

lution of 6.1 nm was achieved for the reconstructions (Fig. B.6b). The sudden drop of the FSC curve corresponds to the cut-off of the diffraction intensity by the detector edge, indicating that either the use of a larger detector or shortening the distance between the sample and the detector will improve the resolution.

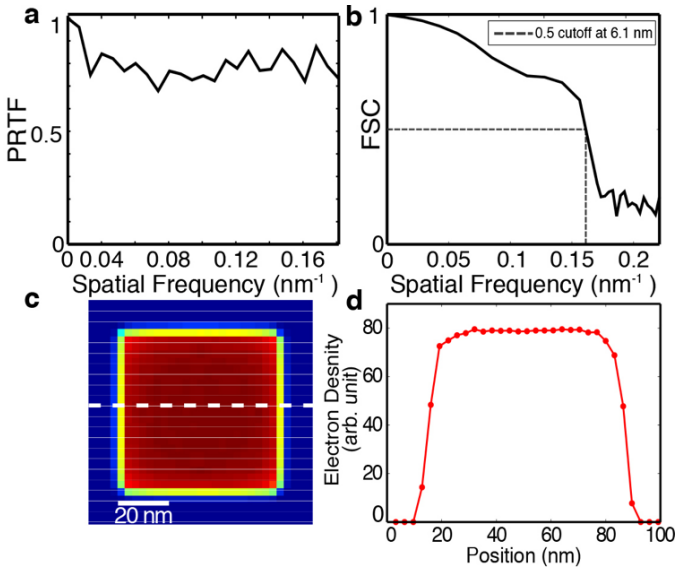

Figure B.6: Quantitative analysis of the 3D reconstruction. **(a)**, Average Phase Retrieval Transfer Function (PRTF) across all of the multiple experimental reconstructions for all 34 diffraction patterns. **(b)**, Average Fourier shell correlation (FSC) between every pair of the 34 reconstructed nanoparticles, indicating a 3D resolution of 6 nm based on the criterion of FSC = 0.5. **(c)**, Central 32-nm-thick slice of a final 3D reconstruction with an overlaid line scan plotted in **(d)**, showing the electron density variation of the Au core and Pd shell. (*Figure reprinted from [270]*)

To precisely determine the size and elemental specificity of the core-shell nanoparticles, we implemented a super-resolution 3D CDI technique. This technique exploited the quantitative 3D reconstruction and used model fitting to achieve resolution beyond the diffraction signal. Specifically, for each of the top 10% independent reconstructions resulting from a single-shot diffraction pattern,

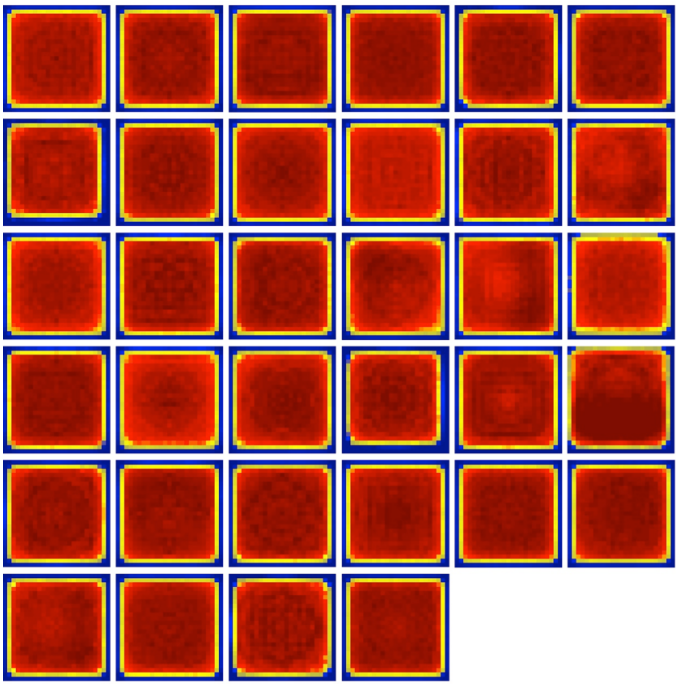

Figure B.7: Central 32-nm-thick slices of the final 3D reconstructions for the 34 single-shot diffraction patterns. The red color represents the Au core and yellow is the Pd shell. (*Figure reprinted from [270]*)

a 3D model was created at five times the voxel resolution of the reconstructed structure. The model was binned and compared with the reconstruction using an error metric,

$$Err = \frac{\sum_{\vec{r}} |\rho_{rec}(\vec{r}) - \rho_{mod}(\vec{r})|}{\sum_{\vec{r}} \rho_{mod}(\vec{r})} \tag{B.3}$$

where $\rho_{rec}(\vec{r})$ and $\rho_{mod}(\vec{r})$ are the electron intensity of the reconstruction and model, respectively. By varying the core size, shell thickness, and ratio of core to shell density, a series of errors were computed using Eq. (B.3) and the model with the lowest error was recorded for the reconstruction. For all the top 10% independent reconstructions from a single-shot diffraction pattern, the parameters of the recorded models were averaged to obtain the core size, shell thickness, and ratio of core to shell density. To validate this technique, we applied it to 34 single-shot diffraction patterns, each of which was measured from a different core-shell nanoparticle. Figure B.8 shows the distribution of the average core size, shell thickness, and ratio of core to shell density for the 34 nanoparticles. The core size is between 64 and 67 nm, while the shell thickness is within 3-5 nm. By statistically averaging the 34 nanoparticles, we obtained a 4.0 ± 0.5 nm thick shell of Pd surrounding a uniform 65.0 ± 1.0 nm Au core, indicating that we can achieve resolution better than the diffraction signal (6.1 nm). The average intensity ratio between the Au core and Pd shell was 1.69, which is within 3% agreement of the tabulated scattering factor ratio of 1.64 [274]. A validation simulation was performed to verify that such precision could be obtained and that a distinction could be made between a model with a thin shell and one without B.9.

Finally, we performed numerical simulations on single-shot 3D imaging of individual viruses without the requirement of multiple-particle averaging. The faustovirus of ~200 nm in diameter was chosen as a model system in our simulations. The 3D structure of the virus was obtained from the Electron Microscopy Data Bank (EMDB ID 8144) and converted to 3D electron density. Figures B.10(a-

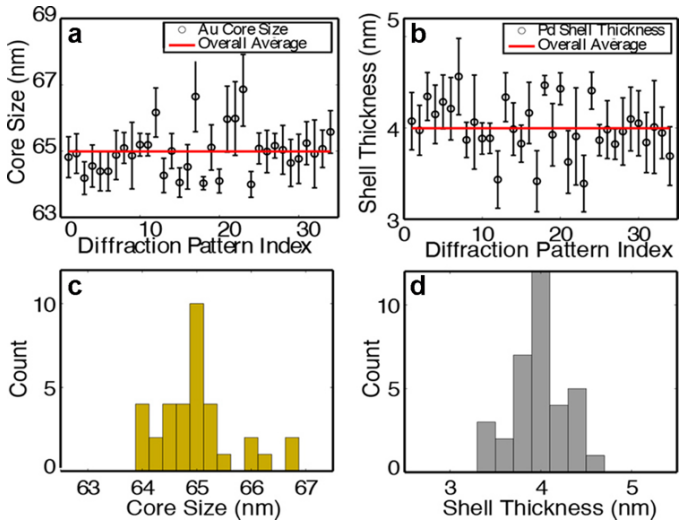

Figure B.8: Experimental implementation of 3D super-resolution CDI of core-shell nanoparticles. **(a)** and **(b)**, The distribution of the core size and shell thickness obtained from 34 single-shot diffraction patterns. Each data point shows the mean and standard deviation of the top 10% of 1,000 independent reconstructions for a single-shot diffraction pattern. The horizontal red lines indicate the average core size and shell thickness across all 34 nanoparticles. **(c)** and **(d)**, The core/shell distribution of the 34 nanoparticles, indicating the Au core size and the Pd shell thickness are 65.0 ± 1.0 nm and 4.0 ± 0.5 nm, respectively, which are beyond the diffraction signal resolution (6.1 nm). (*Figure reprinted from [270]*)

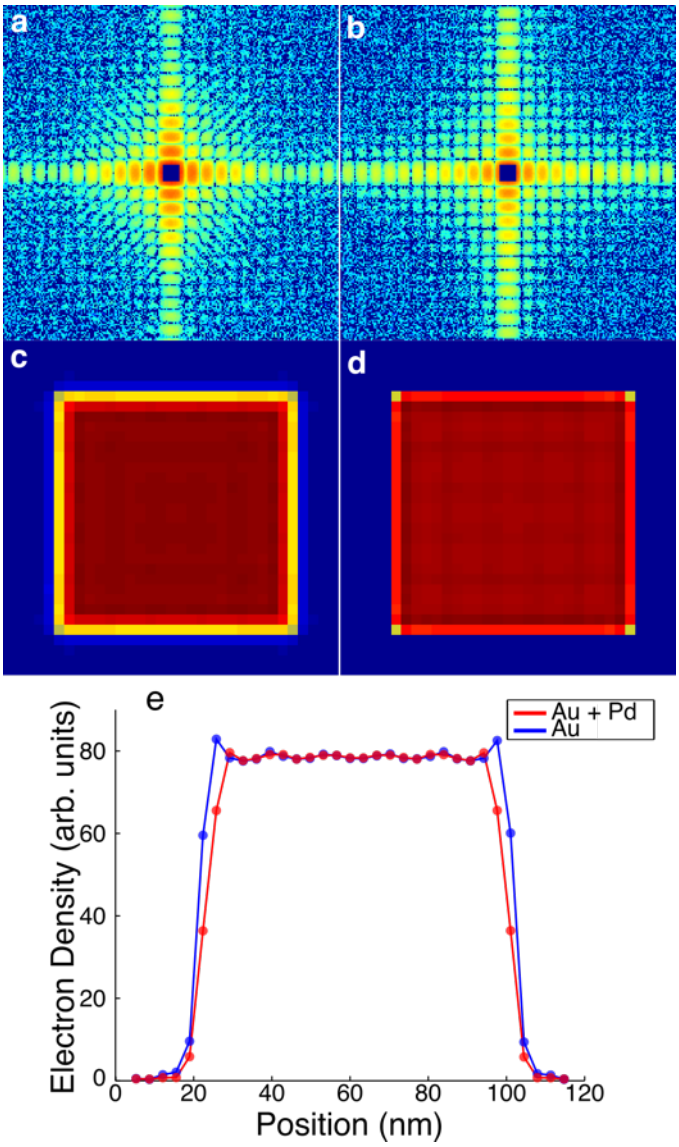

Figure B.9: Numerical simulations on 3D super-resolution CDI of nanoparticles. Noisy diffraction patterns were calculated from a core/shell model with a 65 nm Au core and a 4 nm Pd shell **(a)** and a solid cubic model of 73 nm Au **(b)**. The central data in the diffraction pattern were removed to simulate a beam stop. The top 10% of 1,000 independent reconstructions were averaged and the central 20 nm sections are shown for the Au/Pd core-shell model **(c)** and the solid Au model **(d)**. **(e)**, Line scans through the center of the corresponding reconstructions of the Au/Pd core-shell and the solid Au model. (*Figure reprinted from [270]*)

c) show three 6-nm-thick central slices of the virus capsid along the 2-, 3-, and 5-fold symmetry, respectively. XFEL pulses were simulated based on the Linac Coherent Light Source (LCLS) parameters with E = 1.8 keV and 10^{13} photons per pulse [262]. Each XFEL pulse was focused to a spot of 1 μm in diameter and impinged on a single virus aerosolized by a particle jet using a diffraction-before-destruction data collection scheme [40, 264]. The diffraction intensity was collected by a simulated LCLS detector with 760 x 760 pixels, a pixel size of 110 x 110 μm, and a quantum efficiency of 80%. The detector was placed at a distance of 0.75 m downstream of the sample. To simulate real experimental conditions, both Poisson and detector readout noise were added to the diffraction intensity. Figure B.10(d) shows a representative single-shot diffraction pattern of a faustovirus capsid, which has a missing center slightly larger than the central speckle and a diffraction angle at the edge of $2\Theta = 3.26°$. This diffraction pattern was sampled onto the detector in the same way as the core-shell nanocubes except with icosahedral instead of octahedral symmetry. A total of 1,000 independent OSS reconstructions were performed using a loose spherical support. The best 100 reconstructions with smallest R-factors were averaged to obtain a tighter support. Another round of 1,000 iterations were performed with this tighter support, and the top 100 reconstructions were averaged to produce the final reconstruction. Figures B.10(e-g) show the three corresponding slices of the faustovirus capsid reconstructed from the noisy diffraction pattern (Fig. B.10d), which are in good agreement with the original model (Fig. B.10(a-c)). By computing the Fourier shell correlation between the model and the reconstruction (Fig. B.10(h)), we estimated a 3D resolution of 12.4 nm was achieved in our simulations. The spatial resolution can in principle be improved by focusing the XFEL pulse to a smaller than 1 μm spot, coupled with a larger detector.

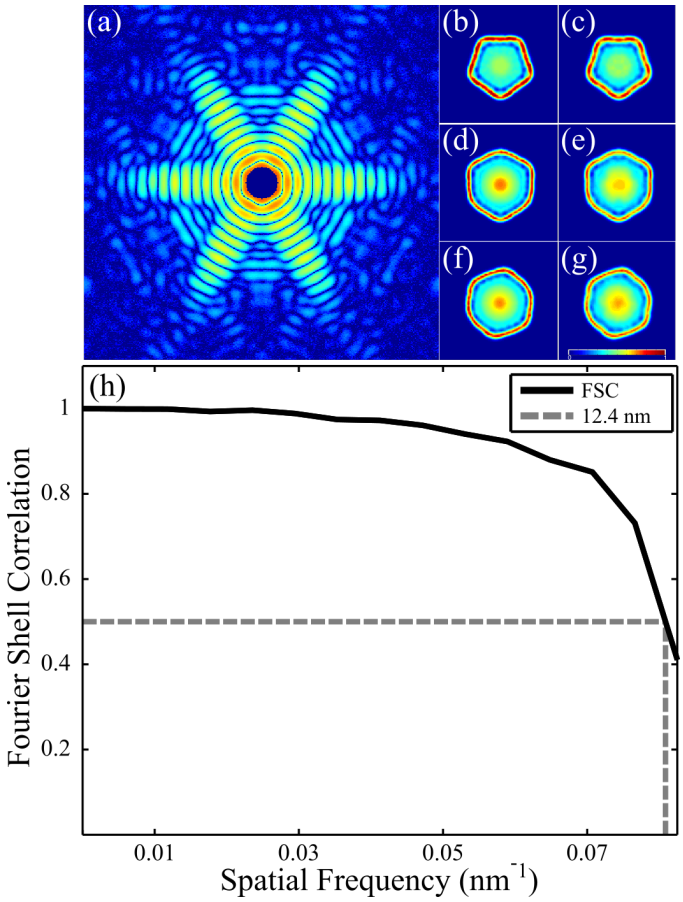

Figure B.10: Simulation of 3D CDI of the icosahedral faustovirus. **(a)** A noisy diffraction pattern along the three-fold axis was used as input to the reconstruction process. Representative slices through the center of the reconstruction along the five-fold, three-fold, and two-fold axes are shown for the model **(b, d, f)** and for the reconstruction **(c, e, g)**. **(h)** The Fourier shell correlation between the reconstruction and the model, indicating a 3D resolution of approximately 12.4 nm was obtained.

B.3 Conclusions

We demonstrated quantitative 3D imaging of Au/Pd core-shell nanoparticles with elemental specificity using single XFEL pulses. These core-shell structures are representative of a vast library of nanoparticles with varying chemical, catalytic, optical and electronic properties [251–254]. We developed a semi-automated and quantitative routine for analyzing nanostructures, and applied it to 34 isolated nanoparticles. Using the curvature of the Ewald sphere and symmetry intrinsic to the nanoparticle, we reconstructed highly reproducible 3D structures from single-shot diffraction patterns with a 3D resolution of 6.1 nm on 5-6 fs timescales. Furthermore, we implemented a 3D super-resolution CDI technique to extract structural information beyond the diffraction signal. By taking advantage of the quantitative 3D reconstruction, our super-resolution technique precisely determined the size of the Au core and the thickness of the Pd shell to be 65.0 $\pm$ 1.0 nm and 4.0 $\pm$ 0.5 nm, respectively. The quantified electron density of the core and shell structure matches the tabulated scattering factor ratio of Au/Pd within a 3% deviation. The effectiveness of this super-resolution technique was validated by using 34 independently reconstructed nanoparticles. While in this work we demonstrated our super-resolution technique by using core-shell nanoparticles, the high-resolution model fitting procedure could in principle be combined with 3D CDI methods to image other samples with spatial resolution beyond the diffraction signal. Finally, we performed numerical simulations on single-shot 3D imaging of individual virus particles using XFEL pulses. Although single-particle cryo-electron microscopy has been routinely applied to image the 3D structure of the virus particles at near atomic resolution, it requires averaging many identical copies [19]. On the other hand, our single-shot CDI method promises to determine the 3D structure of a single virus, which can potentially be used to distinguish structure variation among the same type of virus particles.

References

[1] R. Xu, C.-C. Chen, L. Wu, M. Scott, W. Theis, C. Ophus, M. Bartels, Y. Yang, H. Ramezani-Dakhel, M. R. Sawaya, *et al.*, "Three-dimensional coordinates of individual atoms in materials revealed by electron tomography," *Nature materials*, vol. 14, no. 11, pp. 1099–1103, 2015.

[2] M. C. Scott, C.-C. Chen, M. Mecklenburg, C. Zhu, R. Xu, P. Ercius, U. Dahmen, B. C. Regan, and J. Miao, "Electron tomography at 2.4-angstrom resolution," *Nature*, vol. 483, pp. 444–447, Mar. 2012.

[3] Y. Yang, C.-C. Chen, M. Scott, C. Ophus, R. Xu, A. Pryor, L. Wu, F. Sun, W. Theis, J. Zhou, *et al.*, "Deciphering chemical order/disorder and material properties at the single-atom level," *Nature*, vol. 542, no. 7639, pp. 75–79, 2017.

[4] A. Bartesaghi, D. Matthies, S. Banerjee, A. Merk, and S. Subramaniam, "Structure of -galactosidase at 3.2-A resolution obtained by cryo-electron microscopy," *Proceedings of the National Academy of Sciences*, vol. 111, pp. 11709–11714, Aug. 2014.

[5] V. Lui, F. Frster, and W. Baumeister, "STRUCTURAL STUDIES BY ELECTRON TOMOGRAPHY: From Cells to Molecules," *Annual Review of Biochemistry*, vol. 74, pp. 833–865, June 2005.

[6] C. M. Oikonomou, Y.-W. Chang, and G. J. Jensen, "A new view into prokaryotic cell biology from electron cryotomography," *Nature Reviews Microbiology*, vol. 14, pp. 205–220, Apr. 2016.

[7] A. Momose, T. Takeda, Y. Itai, and K. Hirano, "Phasecontrast Xray computed tomography for observing biological soft tissues," *Nature Medicine*, vol. 2, pp. 473–475, Apr. 1996.

[8] B. P. Fahimian, Y. Mao, P. Cloetens, and J. Miao, "Low-dose x-ray phase-contrast and absorption CT using equally sloped tomography," *Physics in Medicine and Biology*, vol. 55, pp. 5383–5400, Sept. 2010.

[9] Y. Zhao, E. Brun, P. Coan, Z. Huang, A. Sztrokay, P. C. Diemoz, S. Liebhardt, A. Mittone, S. Gasilov, J. Miao, and A. Bravin, "High-resolution, low-dose phase contrast X-ray tomography for 3D diagnosis of human breast cancers," *Proceedings of the National Academy of Sciences*, vol. 109, pp. 18290–18294, Nov. 2012.

[10] D. Shapiro, P. Thibault, T. Beetz, V. Elser, M. Howells, C. Jacobsen, J. Kirz, E. Lima, H. Miao, A. M. Neiman, and D. Sayre, "Biological imaging by soft x-ray diffraction microscopy," *Proceedings of the National Academy of*

Sciences of the United States of America, vol. 102, pp. 15343–15346, Oct. 2005.

[11] W. Dai, C. Fu, H. A. Khant, S. J. Ludtke, M. F. Schmid, and W. Chiu, "Zernike phase-contrast electron cryotomography applied to marine cyanobacteria infected with cyanophages," *Nature Protocols*, vol. 9, pp. 2630–2642, Oct. 2014.

[12] W. Dai, C. Fu, D. Raytcheva, J. Flanagan, H. A. Khant, X. Liu, R. H. Rochat, C. Haase-Pettingell, J. Piret, S. J. Ludtke, K. Nagayama, M. F. Schmid, J. A. King, and W. Chiu, "Visualizing virus assembly intermediates inside marine cyanobacteria," *Nature*, vol. 502, pp. 707–710, Oct. 2013.

[13] K. Grnewald, P. Desai, D. C. Winkler, J. B. Heymann, D. M. Belnap, W. Baumeister, and A. C. Steven, "Three-Dimensional Structure of Herpes Simplex Virus from Cryo-Electron Tomography," *Science*, vol. 302, pp. 1396–1398, Nov. 2003.

[14] A. Yermukhambetova, C. Tan, S. R. Daemi, Z. Bakenov, J. A. Darr, D. J. L. Brett, and P. R. Shearing, "Exploring 3D microstructural evolution in Li-Sulfur battery electrodes using in-situ X-ray tomography," *Scientific Reports*, vol. 6, Dec. 2016.

[15] D. Schrder, C. L. Bender, T. Arlt, M. Osenberg, A. Hilger, S. Risse, M. Ballauff, I. Manke, and J. Janek, "In operando x-ray tomography for next-generation batteries: a systematic approach to monitor reaction product distribution and transport processes," *Journal of Physics D: Applied Physics*, vol. 49, no. 40, p. 404001, 2016.

[16] A. Averbuch, R. Coifman, D. Donoho, M. Elad, and M. Israeli, "Fast and accurate Polar Fourier transform," *Applied and Computational Harmonic Analysis*, vol. 21, pp. 145–167, Sept. 2006.

[17] J. Miao, F. Frster, and O. Levi, "Equally sloped tomography with oversampling reconstruction," *Physical Review B*, vol. 72, p. 052103, Aug. 2005.

[18] J. Jackson, C. Meyer, D. Nishimura, and A. Macovski, "Selection of a convolution function for Fourier inversion using gridding (computerised tomography application)," *IEEE Transactions on Medical Imaging*, vol. 10, pp. 473–478, Sept. 1991.

[19] J. Frank, *Three-dimensional electron microscopy of macromolecular assemblies*. San Diego: Academic Press, 1996.

[20] E. J. Kirkland, *Advanced Computing in Electron Microscopy*. Springer, 2010.

[21] W. Baumeister, "Electron tomography of molecules and cells," *Trends in Cell Biology*, vol. 9, pp. 81–85, Feb. 1999.

[22] C.-C. Chen, C. Zhu, E. R. White, C.-Y. Chiu, M. C. Scott, B. C. Regan, L. D. Marks, Y. Huang, and J. Miao, "Three-dimensional imaging of dislocations in a nanoparticle at atomic resolution," *Nature*, vol. 496, pp. 74–77, Apr. 2013.

[23] R. Han, L. Wang, Z. Liu, F. Sun, and F. Zhang, "A novel fully automatic scheme for fiducial marker-based alignment in electron tomography," *Journal of Structural Biology*, vol. 192, pp. 403–417, Dec. 2015.

[24] S. H. Scheres, "RELION: Implementation of a Bayesian approach to cryo-EM structure determination," *Journal of Structural Biology*, vol. 180, pp. 519–530, Dec. 2012.

[25] J. L. Rubinstein and M. A. Brubaker, "Alignment of cryo-EM movies of individual particles by optimization of image translations," *Journal of Structural Biology*, vol. 192, pp. 188–195, Nov. 2015.

[26] G. Tang, L. Peng, P. R. Baldwin, D. S. Mann, W. Jiang, I. Rees, and S. J. Ludtke, "EMAN2: An extensible image processing suite for electron microscopy," *Journal of Structural Biology*, vol. 157, pp. 38–46, Jan. 2007.

[27] N. Grigorieff, "Frealign," in *Methods in Enzymology*, vol. 579, pp. 191–226, Elsevier, 2016.

[28] A. Pryor Jr., Y. Yang, A. Rana, M. Gallagher-Jones, J. Zhou, Y. H. Lo, G. Melinte, W. Chiu, J. A. Rodriguez, and J. Miao, "GENFIRE: A generalized Fourier iterative reconstruction algorithm for high-resolution 3D imaging," *Scientific Reports*, vol. 7, Dec. 2017.

[29] J. Miao, P. Ercius, and S. J. L. Billinge, "Atomic electron tomography: 3D structures without crystals," *Science*, vol. 353, pp. aaf2157–aaf2157, Sept. 2016.

[30] P. Ercius, M. Boese, T. Duden, and U. Dahmen, "Operation of TEAM I in a User Environment at NCEM," *Microscopy and Microanalysis*, vol. 18, pp. 676–683, Aug. 2012.

[31] J. R. Kremer, D. N. Mastronarde, and J. McIntosh, "Computer Visualization of Three-Dimensional Image Data Using IMOD," *Journal of Structural Biology*, vol. 116, pp. 71–76, Jan. 1996.

[32] F. Amat, F. Moussavi, L. R. Comolli, G. Elidan, K. H. Downing, and M. Horowitz, "Markov random field based automatic image alignment for electron tomography," *Journal of Structural Biology*, vol. 161, pp. 260–275, Mar. 2008.

[33] N. Jaitly, M. A. Brubaker, J. L. Rubinstein, and R. H. Lilien, "A Bayesian method for 3D macromolecular structure inference using class average images from single particle electron microscopy," *Bioinformatics*, vol. 26, pp. 2406–2415, Oct. 2010.

[34] B. Moths and A. Ourmazd, "Bayesian algorithms for recovering structure from single-particle diffraction snapshots of unknown orientation: a comparison," *Acta Crystallographica Section A Foundations of Crystallography*, vol. 67, pp. 481–486, Sept. 2011.

[35] K. R. Hogstrom, M. D. Mills, and P. R. Almond, "Electron beam dose calculations," *Physics in Medicine and Biology*, vol. 26, no. 3, p. 445, 1981.

[36] K. Kawachi, "Calculation of electron dose distribution for radiotherapy treatment planning," *Physics in Medicine and Biology*, vol. 20, no. 4, p. 571, 1975.

[37] E. Lee, B. P. Fahimian, C. V. Iancu, C. Suloway, G. E. Murphy, E. R. Wright, D. Castao-Dez, G. J. Jensen, and J. Miao, "Radiation dose reduction and image enhancement in biological imaging through equally-sloped tomography," *Journal of structural biology*, vol. 164, no. 2, pp. 221–227, 2008.

[38] J. Nelson, X. Huang, J. Steinbrener, D. Shapiro, J. Kirz, S. Marchesini, A. M. Neiman, J. J. Turner, and C. Jacobsen, "High-resolution x-ray diffraction microscopy of specifically labeled yeast cells," *Proceedings of the National Academy of Sciences of the United States of America*, vol. 107, pp. 7235–7239, Apr. 2010.

[39] M. Howells, T. Beetz, H. Chapman, C. Cui, J. Holton, C. Jacobsen, J. Kirz, E. Lima, S. Marchesini, H. Miao, D. Sayre, D. Shapiro, J. Spence, and D. Starodub, "An assessment of the resolution limitation due to radiation-damage in X-ray diffraction microscopy," *Journal of Electron Spectroscopy and Related Phenomena*, vol. 170, pp. 4–12, Mar. 2009.

[40] R. Neutze, R. Wouts, D. van der Spoel, E. Weckert, and J. Hajdu, "Potential for biomolecular imaging with femtosecond X-ray pulses," *Nature*, vol. 406, pp. 752–757, Aug. 2000.

[41] P. Riley, "Free Radicals in Biology: Oxidative Stress and the Effects of Ionizing Radiation," *International Journal of Radiation Biology*, vol. 65, pp. 27–33, Jan. 1994.

[42] R. Henderson, "Cryo-Protection of Protein Crystals against Radiation Damage in Electron and X-Ray Diffraction," *Proceedings of the Royal Society B: Biological Sciences*, vol. 241, pp. 6–8, July 1990.

[43] D. J. Brenner, R. Doll, D. T. Goodhead, E. J. Hall, C. E. Land, J. B. Little, J. H. Lubin, D. L. Preston, R. J. Preston, J. S. Puskin, E. Ron, R. K. Sachs, J. M. Samet, R. B. Setlow, and M. Zaider, "Cancer risks attributable to low doses of ionizing radiation: Assessing what we really know," *Proceedings of the National Academy of Sciences*, vol. 100, pp. 13761–13766, Nov. 2003.

[44] L. Lomb, T. R. M. Barends, S. Kassemeyer, A. Aquila, S. W. Epp, B. Erk, L. Foucar, R. Hartmann, B. Rudek, D. Rolles, A. Rudenko, R. L. Shoeman, J. Andreasson, S. Bajt, M. Barthelmess, A. Barty, M. J. Bogan, C. Bostedt, J. D. Bozek, C. Caleman, R. Coffee, N. Coppola, D. P. DePonte, R. B. Doak, T. Ekeberg, H. Fleckenstein, P. Fromme, M. Gebhardt, H. Graafsma, L. Gumprecht, C. Y. Hampton, A. Hartmann, G. Hauser, H. Hirsemann, P. Holl, J. M. Holton, M. S. Hunter, W. Kabsch, N. Kimmel, R. A. Kirian, M. Liang, F. R. N. C. Maia, A. Meinhart, S. Marchesini, A. V. Martin, K. Nass, C. Reich, J. Schulz, M. M. Seibert, R. Sierra, H. Soltau, J. C. H. Spence, J. Steinbrener, F. Stellato, S. Stern, N. Timneanu, X. Wang, G. Weidenspointner, U. Weierstall, T. A. White, C. Wunderer, H. N. Chapman, J. Ullrich, L. Strder, and I. Schlichting, "Radiation damage in protein serial femtosecond crystallography using an x-ray free-electron laser," *Physical Review B*, vol. 84, Dec. 2011.

[45] R. Henderson, "Avoiding the pitfalls of single particle cryo-electron microscopy: Einstein from noise," *Proceedings of the National Academy of Sciences*, vol. 110, pp. 18037–18041, Nov. 2013.

[46] P. B. Rosenthal and R. Henderson, "Optimal Determination of Particle Orientation, Absolute Hand, and Contrast Loss in Single-particle Electron Cryomicroscopy," *Journal of Molecular Biology*, vol. 333, pp. 721–745, Oct. 2003.

[47] X. Li, P. Mooney, S. Zheng, C. R. Booth, M. B. Braunfeld, S. Gubbens, D. A. Agard, and Y. Cheng, "Electron counting and beam-induced motion correction enable near-atomic-resolution single-particle cryo-EM," *Nature Methods*, vol. 10, pp. 584–590, June 2013.

[48] T. Ekeberg, M. Svenda, C. Abergel, F. R. N. C. Maia, V. Seltzer, J.-M. Claverie, M. Hantke, O. Jönsson, C. Nettelblad, G. van der Schot, M. Liang, D. P. DePonte, A. Barty, M. M. Seibert, B. Iwan, I. Andersson, N. D. Loh, A. V. Martin, H. Chapman, C. Bostedt, J. D. Bozek, K. R. Ferguson, J. Krzywinski, S. W. Epp, D. Rolles, A. Rudenko, R. Hartmann, N. Kimmel, and J. Hajdu, "Three-dimensional reconstruction of the giant mimivirus particle with an x-ray free-electron laser," *Phys. Rev. Lett.*, vol. 114, p. 098102, Mar 2015.

[49] H. N. Chapman, P. Fromme, A. Barty, T. A. White, R. A. Kirian, A. Aquila, M. S. Hunter, J. Schulz, D. P. DePonte, U. Weierstall, R. B. Doak, F. R.

N. C. Maia, A. V. Martin, I. Schlichting, L. Lomb, N. Coppola, R. L. Shoeman, S. W. Epp, R. Hartmann, D. Rolles, A. Rudenko, L. Foucar, N. Kimmel, G. Weidenspointner, P. Holl, M. Liang, M. Barthelmess, C. Caleman, S. Boutet, M. J. Bogan, J. Krzywinski, C. Bostedt, S. Bajt, L. Gumprecht, B. Rudek, B. Erk, C. Schmidt, A. Hmke, C. Reich, D. Pietschner, L. Strder, G. Hauser, H. Gorke, J. Ullrich, S. Herrmann, G. Schaller, F. Schopper, H. Soltau, K.-U. Khnel, M. Messerschmidt, J. D. Bozek, S. P. Hau-Riege, M. Frank, C. Y. Hampton, R. G. Sierra, D. Starodub, G. J. Williams, J. Hajdu, N. Timneanu, M. M. Seibert, J. Andreasson, A. Rocker, O. Jnsson, M. Svenda, S. Stern, K. Nass, R. Andritschke, C.-D. Schrter, F. Krasniqi, M. Bott, K. E. Schmidt, X. Wang, I. Grotjohann, J. M. Holton, T. R. M. Barends, R. Neutze, S. Marchesini, R. Fromme, S. Schorb, D. Rupp, M. Adolph, T. Gorkhover, I. Andersson, H. Hirsemann, G. Potdevin, H. Graafsma, B. Nilsson, and J. C. H. Spence, "Femtosecond X-ray protein nanocrystallography," *Nature*, vol. 470, pp. 73–77, Feb. 2011.

[50] A. T. Brnger, "Free R value: cross-validation in crystallography," *Methods in Enzymology*, vol. 277, pp. 366–396, 1997.

[51] A. C. Kak and M. Slaney, *Principles of Computerized Tomographic Imaging*. Society for Industrial and Applied Mathematics, Jan. 2001.

[52] G. T. Herman and G. T. Herman, *Fundamentals of computerized tomography: image reconstruction from projections*. Advances in pattern recognition, Dordrecht ; New York: Springer, 2nd ed ed., 2009. OCLC: ocn435423235.

[53] A. Momose, T. Takeda, Y. Itai, and K. Hirano, "Phase-contrast X-ray computed tomography for observing biological soft tissues," *Nature Medicine*, vol. 2, pp. 473–475, Apr. 1996.

[54] F. Pfeiffer, T. Weitkamp, O. Bunk, and C. David, "Phase retrieval and differential phase-contrast imaging with low-brilliance X-ray sources," *Nature Physics*, vol. 2, pp. 258–261, Apr. 2006.

[55] R. Fernandez-Leiro and S. H. W. Scheres, "Unravelling biological macromolecules with cryo-electron microscopy," *Nature*, vol. 537, pp. 339–346, Sept. 2016.

[56] B. Goris, J. De Beenhouwer, A. De Backer, D. Zanaga, K. J. Batenburg, A. Snchez-Iglesias, L. M. Liz-Marzn, S. Van Aert, S. Bals, J. Sijbers, and G. Van Tendeloo, "Measuring Lattice Strain in Three Dimensions through Electron Microscopy," *Nano Letters*, vol. 15, pp. 6996–7001, Oct. 2015.

[57] G. Haberfehlner, P. Thaler, D. Knez, A. Volk, F. Hofer, W. E. Ernst, and G. Kothleitner, "Formation of bimetallic clusters in superfluid helium nan-

odroplets analysed by atomic resolution electron tomography," *Nature Communications*, vol. 6, Dec. 2015.

[58] Y. Cheng, "Single-Particle Cryo-EM at Crystallographic Resolution," *Cell*, vol. 161, pp. 450–457, Apr. 2015.

[59] E. Nogales, "The development of cryo-EM into a mainstream structural biology technique," *Nature methods*, vol. 13, pp. 24–27, Jan. 2016.

[60] C. A. Larabell and K. A. Nugent, "Imaging cellular architecture with X-rays," *Current Opinion in Structural Biology*, vol. 20, pp. 623–631, Oct. 2010.

[61] J. W. Gibbs, K. A. Mohan, E. B. Gulsoy, A. J. Shahani, X. Xiao, C. A. Bouman, M. De Graef, and P. W. Voorhees, "The Three-Dimensional Morphology of Growing Dendrites," *Scientific Reports*, vol. 5, Dec. 2015.

[62] F. Meirer, J. Cabana, Y. Liu, A. Mehta, J. C. Andrews, and P. Pianetta, "Three-dimensional imaging of chemical phase transformations at the nanoscale with full-field transmission X-ray microscopy," *Journal of Synchrotron Radiation*, vol. 18, pp. 773–781, Sept. 2011.

[63] M. Krenkel, A. Markus, M. Bartels, C. Dullin, F. Alves, and T. Salditt, "Phase-contrast zoom tomography reveals precise locations of macrophages in mouse lungs," *Scientific Reports*, vol. 5, Sept. 2015.

[64] J. Miao, P. Charalambous, J. Kirz, and D. Sayre, "Extending the methodology of X-ray crystallography to allow imaging of micrometre-sized non-crystalline specimens," *Nature*, vol. 400, pp. 342–344, July 1999.

[65] J. Miao, C.-C. Chen, C. Song, Y. Nishino, Y. Kohmura, T. Ishikawa, D. Ramunno-Johnson, T.-K. Lee, and S. H. Risbud, "Three-Dimensional GaN Ga 2 O 3 Core Shell Structure Revealed by X-Ray Diffraction Microscopy," *Physical Review Letters*, vol. 97, Nov. 2006.

[66] Y. Nishino, Y. Takahashi, N. Imamoto, T. Ishikawa, and K. Maeshima, "Three-Dimensional Visualization of a Human Chromosome Using Coherent X-Ray Diffraction," *Physical Review Letters*, vol. 102, Jan. 2009.

[67] H. Jiang, C. Song, C.-C. Chen, R. Xu, K. S. Raines, B. P. Fahimian, C.-H. Lu, T.-K. Lee, A. Nakashima, J. Urano, T. Ishikawa, F. Tamanoi, and J. Miao, "Quantitative 3D imaging of whole, unstained cells by using X-ray diffraction microscopy," *Proceedings of the National Academy of Sciences*, vol. 107, pp. 11234–11239, June 2010.

[68] M. Dierolf, A. Menzel, P. Thibault, P. Schneider, C. M. Kewish, R. Wepf, O. Bunk, and F. Pfeiffer, "Ptychographic X-ray computed tomography at the nanoscale," *Nature*, vol. 467, pp. 436–439, Sept. 2010.

[69] H. Jiang, R. Xu, C.-C. Chen, W. Yang, J. Fan, X. Tao, C. Song, Y. Kohmura, T. Xiao, Y. Wang, Y. Fei, T. Ishikawa, W. L. Mao, and J. Miao, "Three-Dimensional Coherent X-Ray Diffraction Imaging of Molten Iron in Mantle Olivine at Nanoscale Resolution," *Physical Review Letters*, vol. 110, May 2013.

[70] J. Miao, T. Ishikawa, I. K. Robinson, and M. M. Murnane, "Beyond crystallography: Diffractive imaging using coherent x-ray light sources," *Science*, vol. 348, pp. 530–535, May 2015.

[71] M. Holler, M. Guizar-Sicairos, E. H. R. Tsai, R. Dinapoli, E. Mller, O. Bunk, J. Raabe, and G. Aeppli, "High-resolution non-destructive three-dimensional imaging of integrated circuits," *Nature*, vol. 543, pp. 402–406, Mar. 2017.

[72] R. Gordon, R. Bender, and G. T. Herman, "Algebraic Reconstruction Techniques (ART) for three-dimensional electron microscopy and X-ray photography," *Journal of Theoretical Biology*, vol. 29, pp. 471–481, Dec. 1970.

[73] A. H. Andersen and A. C. Kak, "Simultaneous algebraic reconstruction technique (SART): a superior implementation of the art algorithm," *Ultrasonic Imaging*, vol. 6, pp. 81–94, Jan. 1984.

[74] P. Gilbert, "Iterative methods for the three-dimensional reconstruction of an object from projections," *Journal of Theoretical Biology*, vol. 36, pp. 105–117, July 1972.

[75] Yingying Zhang and J. Fessler, "Fourier-based forward and back-projectors in iterative fan-beam tomographic image reconstruction," vol. 2, pp. 364–367, IEEE, 2004.

[76] J. Miao, D. Sayre, and H. N. Chapman, "Phase retrieval from the magnitude of the Fourier transforms of nonperiodic objects," *Journal of the Optical Society of America A*, vol. 15, p. 1662, June 1998.

[77] n. Miao and n. Sayre, "On possible extensions of X-ray crystallography through diffraction-pattern oversampling," *Acta Crystallographica. Section A, Foundations of Crystallography*, vol. 56 (Pt 6), pp. 596–605, Nov. 2000.

[78] D. Shepard, "A two-dimensional interpolation function for irregularly-spaced data," pp. 517–524, ACM Press, 1968.

[79] R. Franke, "Scattered data interpolation: tests of some methods," *Mathematics of Computation*, vol. 38, pp. 181–181, Jan. 1982.

[80] M. G. Rossmann, "Ab initio phase determination and phase extension using non-crystallographic symmetry," *Current Opinion in Structural Biology*, vol. 5, pp. 650–655, Oct. 1995.

[81] K. S. Raines, S. Salha, R. L. Sandberg, H. Jiang, J. A. Rodrguez, B. P. Fahimian, H. C. Kapteyn, J. Du, and J. Miao, "Three-dimensional structure determination from a single view," *Nature*, vol. 463, no. 7278, pp. 214–217, 2010.

[82] E. J. Kirkland, *Advanced computing in electron microscopy*. New York: Springer, second edition ed., 2010.

[83] K. Dabov, A. Foi, V. Katkovnik, and K. Egiazarian, "Image Denoising by Sparse 3-D Transform-Domain Collaborative Filtering," *IEEE Transactions on Image Processing*, vol. 16, pp. 2080–2095, Aug. 2007.

[84] D. Q. Huynh, "Metrics for 3D Rotations: Comparison and Analysis," *Journal of Mathematical Imaging and Vision*, vol. 35, pp. 155–164, Oct. 2009.

[85] J. A. Lemberg and R. O. Ritchie, "Mo-Si-B Alloys for Ultrahigh-Temperature Structural Applications," *Advanced Materials*, vol. 24, pp. 3445–3480, July 2012.

[86] F. Rioult, S. Imhoff, R. Sakidja, and J. Perepezko, "Transient oxidation of MoSiB alloys: Effect of the microstructure size scale," *Acta Materialia*, vol. 57, pp. 4600–4613, Sept. 2009.

[87] J.-I. Agulleiro and J.-J. Fernandez, "Tomo3d 2.0 Exploitation of Advanced Vector eXtensions (AVX) for 3D reconstruction," *Journal of Structural Biology*, vol. 189, pp. 147–152, Feb. 2015.

[88] L. Giannuzzi and F. Stevie, "A review of focused ion beam milling techniques for TEM specimen preparation," *Micron*, vol. 30, pp. 197–204, June 1999.

[89] M. Marko, C. Hsieh, R. Schalek, J. Frank, and C. Mannella, "Focused-ion-beam thinning of frozen-hydrated biological specimens for cryo-electron microscopy," *Nature Methods*, vol. 4, pp. 215–217, Mar. 2007.

[90] A. Rigort, F. J. B. Bauerlein, E. Villa, M. Eibauer, T. Laugks, W. Baumeister, and J. M. Plitzko, "Focused ion beam micromachining of eukaryotic cells for cryoelectron tomography," *Proceedings of the National Academy of Sciences*, vol. 109, pp. 4449–4454, Mar. 2012.

[91] D. C. Youla and H. Webb, "Image Restoration by the Method of Convex Projections: Part 1Theory," *IEEE Transactions on Medical Imaging*, vol. 1, pp. 81–94, Oct. 1982.

[92] M. Sezan, "An overview of convex projections theory and its application to image recovery problems," *Ultramicroscopy*, vol. 40, pp. 55–67, Jan. 1992.

[93] E. Candes, J. Romberg, and T. Tao, "Robust uncertainty principles: exact signal reconstruction from highly incomplete frequency information," *IEEE Transactions on Information Theory*, vol. 52, pp. 489–509, Feb. 2006.

[94] D. Donoho, "Compressed sensing," *IEEE Transactions on Information Theory*, vol. 52, pp. 1289–1306, Apr. 2006.

[95] L. I. Rudin, S. Osher, and E. Fatemi, "Nonlinear total variation based noise removal algorithms," *Physica D: Nonlinear Phenomena*, vol. 60, pp. 259–268, Nov. 1992.

[96] R. Leary, Z. Saghi, P. A. Midgley, and D. J. Holland, "Compressed sensing electron tomography," *Ultramicroscopy*, vol. 131, pp. 70–91, Aug. 2013.

[97] W. H. De Jong and P. J. Borm, "Drug delivery and nanoparticles: Applications and hazards," *International Journal of Nanomedicine*, vol. 3, pp. 133–149, June 2008.

[98] A. Z. Wang, R. Langer, and O. C. Farokhzad, "Nanoparticle Delivery of Cancer Drugs," *Annual Review of Medicine*, vol. 63, pp. 185–198, Feb. 2012.

[99] T. R. Pisanic, J. D. Blackwell, V. I. Shubayev, R. R. Fiones, and S. Jin, "Nanotoxicity of iron oxide nanoparticle internalization in growing neurons," *Biomaterials*, vol. 28, pp. 2572–2581, June 2007.

[100] J. J. Conesa, J. Otn, M. Chiappi, J. M. Carazo, E. Pereiro, F. J. Chichn, and J. L. Carrascosa, "Intracellular nanoparticles mass quantification by near-edge absorption soft X-ray nanotomography," *Scientific Reports*, vol. 6, Apr. 2016.

[101] I. K. Robinson, I. A. Vartanyants, G. J. Williams, M. A. Pfeifer, and J. A. Pitney, "Reconstruction of the Shapes of Gold Nanocrystals Using Coherent X-Ray Diffraction," *Physical Review Letters*, vol. 87, Oct. 2001.

[102] J. Miao, K. O. Hodgson, T. Ishikawa, C. A. Larabell, M. A. LeGros, and Y. Nishino, "Imaging whole Escherichia coli bacteria by using single-particle x-ray diffraction," *Proceedings of the National Academy of Sciences*, vol. 100, pp. 110–112, Jan. 2003.

[103] J. Miao, H. N. Chapman, J. Kirz, D. Sayre, and K. O. Hodgson, "Taking X-Ray Diffraction to the Limit: Macromolecular Structures from Femtosecond X-Ray Pulses and Diffraction Microscopy of Cells with Synchrotron Radiation," *Annual Review of Biophysics and Biomolecular Structure*, vol. 33, pp. 157–176, June 2004.

[104] R. L. Sandberg, A. Paul, D. A. Raymondson, S. Hdrich, D. M. Gaudiosi, J. Holtsnider, R. I. Tobey, O. Cohen, M. M. Murnane, H. C. Kapteyn,

C. Song, J. Miao, Y. Liu, and F. Salmassi, "Lensless Diffractive Imaging Using Tabletop Coherent High-Harmonic Soft-X-Ray Beams," *Physical Review Letters*, vol. 99, Aug. 2007.

[105] X. Huang, J. Nelson, J. Kirz, E. Lima, S. Marchesini, H. Miao, A. M. Neiman, D. Shapiro, J. Steinbrener, A. Stewart, J. J. Turner, and C. Jacobsen, "Soft X-ray diffraction microscopy of a frozen hydrated yeast cell," *Physical Review Letters*, vol. 103, p. 198101, Nov. 2009.

[106] E. Lima, Y. Chushkin, P. van der Linden, C. U. Kim, F. Zontone, P. Carpentier, S. M. Gruner, and P. Pernot, "Cryogenic x-ray diffraction microscopy utilizing high-pressure cryopreservation," *Physical Review. E, Statistical, Nonlinear, and Soft Matter Physics*, vol. 90, p. 042713, Oct. 2014.

[107] M. M. Seibert, T. Ekeberg, F. R. N. C. Maia, M. Svenda, J. Andreasson, O. Jnsson, D. Odi, B. Iwan, A. Rocker, D. Westphal, M. Hantke, D. P. DePonte, A. Barty, J. Schulz, L. Gumprecht, N. Coppola, A. Aquila, M. Liang, T. A. White, A. Martin, C. Caleman, S. Stern, C. Abergel, V. Seltzer, J.-M. Claverie, C. Bostedt, J. D. Bozek, S. Boutet, A. A. Miahnahri, M. Messerschmidt, J. Krzywinski, G. Williams, K. O. Hodgson, M. J. Bogan, C. Y. Hampton, R. G. Sierra, D. Starodub, I. Andersson, S. Bajt, M. Barthelmess, J. C. H. Spence, P. Fromme, U. Weierstall, R. Kirian, M. Hunter, R. B. Doak, S. Marchesini, S. P. Hau-Riege, M. Frank, R. L. Shoeman, L. Lomb, S. W. Epp, R. Hartmann, D. Rolles, A. Rudenko, C. Schmidt, L. Foucar, N. Kimmel, P. Holl, B. Rudek, B. Erk, A. Hmke, C. Reich, D. Pietschner, G. Weidenspointner, L. Strder, G. Hauser, H. Gorke, J. Ullrich, I. Schlichting, S. Herrmann, G. Schaller, F. Schopper, H. Soltau, K.-U. Khnel, R. Andritschke, C.-D. Schrter, F. Krasniqi, M. Bott, S. Schorb, D. Rupp, M. Adolph, T. Gorkhover, H. Hirsemann, G. Potdevin, H. Graafsma, B. Nilsson, H. N. Chapman, and J. Hajdu, "Single mimivirus particles intercepted and imaged with an X-ray laser," *Nature*, vol. 470, pp. 78–81, Feb. 2011.

[108] D. Nam, J. Park, M. Gallagher-Jones, S. Kim, S. Kim, Y. Kohmura, H. Naitow, N. Kunishima, T. Yoshida, T. Ishikawa, and C. Song, "Imaging fully hydrated whole cells by coherent x-ray diffraction microscopy," *Physical Review Letters*, vol. 110, p. 098103, Mar. 2013.

[109] C. Song, M. Takagi, J. Park, R. Xu, M. Gallagher-Jones, N. Imamoto, and T. Ishikawa, "Analytic 3D imaging of mammalian nucleus at nanoscale using coherent x-rays and optical fluorescence microscopy," *Biophysical Journal*, vol. 107, pp. 1074–1081, Sept. 2014.

[110] M. F. Hantke, D. Hasse, F. R. N. C. Maia, T. Ekeberg, K. John, M. Svenda, N. D. Loh, A. V. Martin, N. Timneanu, D. S. D. Larsson, G. van der Schot,

G. H. Carlsson, M. Ingelman, J. Andreasson, D. Westphal, M. Liang, F. Stellato, D. P. DePonte, R. Hartmann, N. Kimmel, R. A. Kirian, M. M. Seibert, K. Mhlig, S. Schorb, K. Ferguson, C. Bostedt, S. Carron, J. D. Bozek, D. Rolles, A. Rudenko, S. Epp, H. N. Chapman, A. Barty, J. Hajdu, and I. Andersson, "High-throughput imaging of heterogeneous cell organelles with an X-ray laser," *Nature Photonics*, vol. 8, pp. 943–949, Nov. 2014.

[111] J. A. Rodriguez, R. Xu, C.-C. Chen, Z. Huang, H. Jiang, A. L. Chen, K. S. Raines, A. Pryor Jr, D. Nam, L. Wiegart, C. Song, A. Madsen, Y. Chushkin, F. Zontone, P. J. Bradley, and J. Miao, "Three-dimensional coherent X-ray diffractive imaging of whole frozen-hydrated cells," *IUCrJ*, vol. 2, pp. 575–583, Sept. 2015.

[112] Y. Takayama and K. Yonekura, "Cryogenic coherent X-ray diffraction imaging of biological samples at SACLA: a correlative approach with cryo-electron and light microscopy," *Acta Crystallographica Section A: Foundations and Advances*, vol. 72, no. 2, pp. 179–189, 2016.

[113] M. Gallagher-Jones, J. A. Rodriguez, and J. Miao, "Frontier methods in coherent X-ray diffraction for high-resolution structure determination," *Quarterly Reviews of Biophysics*, vol. 49, 2016.

[114] J. M. Rodenburg, A. C. Hurst, A. G. Cullis, B. R. Dobson, F. Pfeiffer, O. Bunk, C. David, K. Jefimovs, and I. Johnson, "Hard-X-Ray Lensless Imaging of Extended Objects," *Physical Review Letters*, vol. 98, Jan. 2007.

[115] P. Thibault, M. Dierolf, A. Menzel, O. Bunk, C. David, and F. Pfeiffer, "High-Resolution Scanning X-ray Diffraction Microscopy," *Science*, vol. 321, pp. 379–382, July 2008.

[116] F. Berenguer de la Cuesta, M. P. E. Wenger, R. J. Bean, L. Bozec, M. A. Horton, and I. K. Robinson, "Coherent X-ray diffraction from collagenous soft tissues," *Proceedings of the National Academy of Sciences*, vol. 106, pp. 15297–15301, Sept. 2009.

[117] M. Dierolf, P. Thibault, A. Menzel, C. M. Kewish, K. Jefimovs, Ilme Schlichting, K. v. Knig, O. Bunk, and F. Pfeiffer, "Ptychographic coherent diffractive imaging of weakly scattering specimens," *New Journal of Physics*, vol. 12, no. 3, p. 035017, 2010.

[118] A. M. Maiden and J. M. Rodenburg, "An improved ptychographical phase retrieval algorithm for diffractive imaging," *Ultramicroscopy*, vol. 109, pp. 1256–1262, Sept. 2009.

[119] K. Giewekemeyer, P. Thibault, S. Kalbfleisch, A. Beerlink, C. M. Kewish, M. Dierolf, F. Pfeiffer, and T. Salditt, "Quantitative biological imaging

by ptychographic x-ray diffraction microscopy," *Proceedings of the National Academy of Sciences*, vol. 107, pp. 529–534, Jan. 2010.

[120] R. N. Wilke, M. Priebe, M. Bartels, K. Giewekemeyer, A. Diaz, P. Karvinen, and T. Salditt, "Hard X-ray imaging of bacterial cells: nano-diffraction and ptychographic reconstruction," *Optics Express*, vol. 20, pp. 19232–19254, Aug. 2012.

[121] Y. Takahashi, A. Suzuki, S. Furutaku, K. Yamauchi, Y. Kohmura, and T. Ishikawa, "High-resolution and high-sensitivity phase-contrast imaging by focused hard x-ray ptychography with a spatial filter," *Applied Physics Letters*, vol. 102, p. 094102, Mar. 2013.

[122] A. Maiden, G. Morrison, B. Kaulich, A. Gianoncelli, and J. Rodenburg, "Soft X-ray spectromicroscopy using ptychography with randomly phased illumination," *Nature Communications*, vol. 4, p. 1669, Apr. 2013.

[123] M. D. Seaberg, B. Zhang, D. F. Gardner, E. R. Shanblatt, M. M. Murnane, H. C. Kapteyn, and D. E. Adams, "Tabletop nanometer extreme ultraviolet imaging in an extended reflection mode using coherent Fresnel ptychography," *Optica*, vol. 1, p. 39, July 2014.

[124] T. Kimura, Y. Joti, A. Shibuya, C. Song, S. Kim, K. Tono, M. Yabashi, M. Tamakoshi, T. Moriya, T. Oshima, T. Ishikawa, Y. Bessho, and Y. Nishino, "Imaging live cell in micro-liquid enclosure by X-ray laser diffraction," *Nature Communications*, vol. 5, Jan. 2014.

[125] K. Giewekemeyer, C. Hackenberg, A. Aquila, R. Wilke, M. Groves, R. Jordanova, V. Lamzin, G. Borchers, K. Saksl, A. Zozulya, M. Sprung, and A. Mancuso, "Tomography of a Cryo-immobilized Yeast Cell Using Ptychographic Coherent X-Ray Diffractive Imaging," *Biophysical Journal*, vol. 109, pp. 1986–1995, Nov. 2015.

[126] B. Zhang, D. F. Gardner, M. D. Seaberg, E. R. Shanblatt, H. C. Kapteyn, M. M. Murnane, and D. E. Adams, "High contrast 3D imaging of surfaces near the wavelength limit using tabletop EUV ptychography," *Ultramicroscopy*, vol. 158, pp. 98–104, Nov. 2015.

[127] J. Deng, D. J. Vine, S. Chen, Y. S. G. Nashed, Q. Jin, N. W. Phillips, T. Peterka, R. Ross, S. Vogt, and C. J. Jacobsen, "Simultaneous cryo X-ray ptychographic and fluorescence microscopy of green algae," *Proceedings of the National Academy of Sciences of the United States of America*, vol. 112, pp. 2314–2319, Feb. 2015.

[128] A. Diaz, B. Malkova, M. Holler, M. Guizar-Sicairos, E. Lima, V. Panneels, G. Pigino, A. G. Bittermann, L. Wettstein, T. Tomizaki, O. Bunk, G. Schertler, T. Ishikawa, R. Wepf, and A. Menzel, "Three-dimensional mass

density mapping of cellular ultrastructure by ptychographic X-ray nanotomography," *Journal of Structural Biology*, vol. 192, pp. 461–469, Dec. 2015.

[129] I. Zanette, B. Enders, M. Dierolf, P. Thibault, R. Gradl, A. Diaz, M. Guizar-Sicairos, A. Menzel, F. Pfeiffer, and P. Zaslansky, "Ptychographic X-ray nanotomography quantifies mineral distributions in human dentine," *Scientific Reports*, vol. 5, p. 9210, Mar. 2015.

[130] M. W. M. Jones, K. D. Elgass, M. D. Junker, M. D. de Jonge, and G. A. van Riessen, "Molar concentration from sequential 2-D water-window X-ray ptychography and X-ray fluorescence in hydrated cells," *Scientific Reports*, vol. 6, July 2016.

[131] Y. Zhu, W. Cai, R. D. Piner, A. Velamakanni, and R. S. Ruoff, "Transparent self-assembled films of reduced graphene oxide platelets," *Applied Physics Letters*, vol. 95, no. 10, p. 103104, 2009.

[132] R. S. Pantelic, J. C. Meyer, U. Kaiser, W. Baumeister, and J. M. Plitzko, "Graphene oxide: A substrate for optimizing preparations of frozen-hydrated samples," *Journal of Structural Biology*, vol. 170, pp. 152–156, Apr. 2010.

[133] J. Park, H. Park, P. Ercius, A. F. Pegoraro, C. Xu, J. W. Kim, S. H. Han, and D. A. Weitz, "Direct Observation of Wet Biological Samples by Graphene Liquid Cell Transmission Electron Microscopy," *Nano Letters*, vol. 15, pp. 4737–4744, July 2015.

[134] M. Wojcik, M. Hauser, W. Li, S. Moon, and K. Xu, "Graphene-enabled electron microscopy and correlated super-resolution microscopy of wet cells," *Nature Communications*, vol. 6, p. 7384, June 2015.

[135] N. Mohanty, M. Fahrenholtz, A. Nagaraja, D. Boyle, and V. Berry, "Impermeable Graphenic Encasement of Bacteria," *Nano Letters*, vol. 11, pp. 1270–1275, Mar. 2011.

[136] J.-T. Jeong, M.-K. Choi, Y. Sim, J.-T. Lim, G.-S. Kim, M.-J. Seong, J.-H. Hyung, K. S. Kim, A. Umar, and S.-K. Lee, "Effect of graphene oxide ratio on the cell adhesion and growth behavior on a graphene oxide-coated silicon substrate," *Scientific Reports*, vol. 6, Dec. 2016.

[137] M. Kalbacova, A. Broz, J. Kong, and M. Kalbac, "Graphene substrates promote adherence of human osteoblasts and mesenchymal stromal cells," *Carbon*, vol. 48, pp. 4323–4329, Dec. 2010.

[138] W. C. Lee, C. H. Y. X. Lim, H. Shi, L. A. L. Tang, Y. Wang, C. T. Lim, and K. P. Loh, "Origin of Enhanced Stem Cell Growth and Differentiation on Graphene and Graphene Oxide," *ACS Nano*, vol. 5, pp. 7334–7341, Sept. 2011.

[139] E. Garcia-Alegria, M. Iliut, M. Stefanska, C. Silva, S. Heeg, S. J. Kimber, V. Kouskoff, G. Lacaud, A. Vijayaraghavan, and K. Batta, "Graphene Oxide promotes embryonic stem cell differentiation to haematopoietic lineage," *Scientific Reports*, vol. 6, Sept. 2016.

[140] M. Gallagher-Jones, C. S. B. Dias, A. Pryor, K. Bouchmella, L. Zhao, Y. H. Lo, M. B. Cardoso, D. Shapiro, J. Rodriguez, and J. Miao, "Correlative cellular ptychography with functionalized nanoparticles at the Fe L-edge," *Scientific Reports*, vol. 7, Dec. 2017.

[141] D. A. Shapiro, Y.-S. Yu, T. Tyliszczak, J. Cabana, R. Celestre, W. Chao, K. Kaznatcheev, A. L. D. Kilcoyne, F. Maia, S. Marchesini, Y. S. Meng, T. Warwick, L. L. Yang, and H. A. Padmore, "Chemical composition mapping with nanometre resolution by soft X-ray microscopy," *Nature Photonics*, vol. 8, pp. 765–769, Sept. 2014.

[142] P. Denes, D. Doering, H. A. Padmore, J.-P. Walder, and J. Weizeorick, "A fast, direct x-ray detection charge-coupled device," *Review of Scientific Instruments*, vol. 80, p. 083302, Aug. 2009.

[143] S. Marchesini, H. Krishnan, B. J. Daurer, D. A. Shapiro, T. Perciano, J. A. Sethian, and F. R. N. C. Maia, "*SHARP* : a distributed GPU-based ptychographic solver," *Journal of Applied Crystallography*, vol. 49, pp. 1245–1252, Aug. 2016.

[144] M. Guizar-Sicairos, A. Diaz, M. Holler, M. S. Lucas, A. Menzel, R. A. Wepf, and O. Bunk, "Phase tomography from x-ray coherent diffractive imaging projections," *Optics Express*, vol. 19, p. 21345, Oct. 2011.

[145] B. Borm, R. P. Requardt, V. Herzog, and G. Kirfel, "Membrane ruffles in cell migration: indicators of inefficient lamellipodia adhesion and compartments of actin filament reorganization," *Experimental Cell Research*, vol. 302, pp. 83–95, Jan. 2005.

[146] J. Albuschies and V. Vogel, "The role of filopodia in the recognition of nanotopographies," *Scientific Reports*, vol. 3, p. 1658, Apr. 2013.

[147] R. M. Cornell and U. Schwertmann, *The Iron Oxides*. Weinheim, FRG: Wiley-VCH Verlag GmbH & Co. KGaA, July 2003.

[148] J. Frank, "Chapter 5 - Three-Dimensional Reconstruction," in *Three-Dimensional Electron Microscopy of Macromolecular Assemblies*, pp. 182–246, Burlington: Academic Press, 1996.

[149] H. N. Chapman, A. Barty, S. Marchesini, A. Noy, S. P. Hau-Riege, C. Cui, M. R. Howells, R. Rosen, H. He, J. C. H. Spence, U. Weierstall, T. Beetz, C. Jacobsen, and D. Shapiro, "High-resolution ab initio three-dimensional

x-ray diffraction microscopy," *Journal of the Optical Society of America A*, vol. 23, p. 1179, May 2006.

[150] W. W. Yu, J. C. Falkner, C. T. Yavuz, and V. L. Colvin, "Synthesis of monodisperse iron oxide nanocrystals by thermal decomposition of iron carboxylate salts," *Chemical Communications*, pp. 2306–2307, Oct. 2004.

[151] J. Kim, H. Kim, N. Lee, T. Kim, H. Kim, T. Yu, I. Song, W. Moon, and T. Hyeon, "Multifunctional Uniform Nanoparticles Composed of a Magnetite Nanocrystal Core and a Mesoporous Silica Shell for Magnetic Resonance and Fluorescence Imaging and for Drug Delivery," *Angewandte Chemie International Edition*, vol. 47, pp. 8438–8441, Oct. 2008.

[152] C. Song, K. Tono, J. Park, T. Ebisu, S. Kim, H. Shimada, S. Kim, M. Gallagher-Jones, D. Nam, T. Sato, T. Togashi, K. Ogawa, Y. Joti, T. Kameshima, S. Ono, T. Hatsui, S. Iwata, M. Yabashi, and T. Ishikawa, "Multiple application X-ray imaging chamber for single-shot diffraction experiments with femtosecond X-ray laser pulses," *Journal of Applied Crystallography*, vol. 47, pp. 188–197, Feb. 2014.

[153] S. K. Natarajan and S. Selvaraj, "Mesoporous silica nanoparticles: importance of surface modifications and its role in drug delivery," *RSC Advances*, vol. 4, pp. 14328–14334, Mar. 2014.

[154] A. A. Hwang, J. Lu, F. Tamanoi, and J. I. Zink, "Functional Nanovalves on Protein-Coated Nanoparticles for In vitro and In vivo Controlled Drug Delivery," *Small*, vol. 11, pp. 319–328, Jan. 2015.

[155] E. Betzig, G. H. Patterson, R. Sougrat, O. W. Lindwasser, S. Olenych, J. S. Bonifacino, M. W. Davidson, J. Lippincott-Schwartz, and H. F. Hess, "Imaging Intracellular Fluorescent Proteins at Nanometer Resolution," *Science*, vol. 313, pp. 1642–1645, Sept. 2006.

[156] B. Huang, M. Bates, and X. Zhuang, "Super-Resolution Fluorescence Microscopy," *Annual Review of Biochemistry*, vol. 78, pp. 993–1016, June 2009.

[157] V. Lui, A. Rigort, and W. Baumeister, "Cryo-electron tomography: the challenge of doing structural biology in situ," *The Journal of Cell Biology*, vol. 202, pp. 407–419, Aug. 2013.

[158] J. Miao, T. Ishikawa, E. H. Anderson, and K. O. Hodgson, "Phase retrieval of diffraction patterns from noncrystalline samples using the oversampling method," *Physical Review B*, vol. 67, May 2003.

[159] C. Song, H. Jiang, A. Mancuso, B. Amirbekian, L. Peng, R. Sun, S. S. Shah, Z. H. Zhou, T. Ishikawa, and J. Miao, "Quantitative Imaging of Single, Unstained Viruses with Coherent X Rays," *Physical Review Letters*, vol. 101, Oct. 2008.

[160] J. Deng, D. J. Vine, S. Chen, Q. Jin, Y. S. G. Nashed, T. Peterka, S. Vogt, and C. Jacobsen, "X-ray ptychographic and fluorescence microscopy of frozen-hydrated cells using continuous scanning," *Scientific Reports*, vol. 7, Dec. 2017.

[161] R. L. Sandberg, C. Song, P. W. Wachulak, D. A. Raymondson, A. Paul, B. Amirbekian, E. Lee, A. E. Sakdinawat, C. La-O-Vorakiat, M. C. Marconi, C. S. Menoni, M. M. Murnane, J. J. Rocca, H. C. Kapteyn, and J. Miao, "High numerical aperture tabletop soft x-ray diffraction microscopy with 70-nm resolution," *Proceedings of the National Academy of Sciences of the United States of America*, vol. 105, pp. 24–27, Jan. 2008.

[162] A. Ravasio, D. Gauthier, F. R. N. C. Maia, M. Billon, J.-P. Caumes, D. Garzella, M. Gloc, O. Gobert, J.-F. Hergott, A.-M. Pena, H. Perez, B. Carr, E. Bourhis, J. Gierak, A. Madouri, D. Mailly, B. Schiedt, M. Fajardo, J. Gautier, P. Zeitoun, P. H. Bucksbaum, J. Hajdu, and H. Merdji, "Single-Shot Diffractive Imaging with a Table-Top Femtosecond Soft X-Ray Laser-Harmonics Source," *Physical Review Letters*, vol. 103, July 2009.

[163] M. Gallagher-Jones, Y. Bessho, S. Kim, J. Park, S. Kim, D. Nam, C. Kim, Y. Kim, D. Y. Noh, O. Miyashita, F. Tama, Y. Joti, T. Kameshima, T. Hatsui, K. Tono, Y. Kohmura, M. Yabashi, S. S. Hasnain, T. Ishikawa, and C. Song, "Macromolecular structures probed by combining single-shot free-electron laser diffraction with synchrotron coherent X-ray imaging," *Nature Communications*, vol. 5, May 2014.

[164] M. Bergh, G. Huldt, N. Tmneanu, F. R. N. C. Maia, and J. Hajdu, "Feasibility of imaging living cells at subnanometer resolutions by ultrafast X-ray diffraction," *Quarterly Reviews of Biophysics*, vol. 41, p. 181, Nov. 2008.

[165] I. Schlichting and J. Miao, "Emerging opportunities in structural biology with X-ray free-electron lasers," *Current Opinion in Structural Biology*, vol. 22, pp. 613–626, Oct. 2012.

[166] J. R. Fienup, "Phase retrieval algorithms: a comparison," *Applied Optics*, vol. 21, p. 2758, Aug. 1982.

[167] J. A. Rodriguez, R. Xu, C.-C. Chen, Y. Zou, and J. Miao, "Oversampling smoothness: an effective algorithm for phase retrieval of noisy diffraction intensities," *Journal of Applied Crystallography*, vol. 46, pp. 312–318, Apr. 2013.

[168] T. Paunesku, S. Vogt, J. Maser, B. Lai, and G. Woloschak, "X-ray fluorescence microprobe imaging in biology and medicine," *Journal of Cellular Biochemistry*, vol. 99, pp. 1489–1502, Dec. 2006.

[169] C. J. Fahrni, "Biological applications of X-ray fluorescence microscopy: exploring the subcellular topography and speciation of transition metals," *Current Opinion in Chemical Biology*, vol. 11, pp. 121–127, Apr. 2007.

[170] S. Majumdar, J. R. Peralta-Videa, H. Castillo-Michel, J. Hong, C. M. Rico, and J. L. Gardea-Torresdey, "Applications of synchrotron -XRF to study the distribution of biologically important elements in different environmental matrices: A review," *Analytica Chimica Acta*, vol. 755, pp. 1–16, Nov. 2012.

[171] J. Deng, Y. H. Lo, M. Gallagher-Jones, S. Chen, A. Pryor Jr., Q. Jin, Y. P. Hong, S. Vogt, J. Miao, and C. Jacobsen, "Correlative 3D X-ray fluorescence and ptychographic tomography of un-labeled frozen hydrated green algae." 218.

[172] F. A. Ruiz, N. Marchesini, M. Seufferheld, Govindjee, and R. Docampo, "The Polyphosphate Bodies of *Chlamydomonas reinhardtii* Possess a Proton-pumping Pyrophosphatase and Are Similar to Acidocalcisomes," *Journal of Biological Chemistry*, vol. 276, pp. 46196–46203, Dec. 2001.

[173] S. Chen, J. Deng, Y. Yuan, C. Flachenecker, R. Mak, B. Hornberger, Q. Jin, D. Shu, B. Lai, J. Maser, C. Roehrig, T. Paunesku, S. C. Gleber, D. J. Vine, L. Finney, J. VonOsinski, M. Bolbat, I. Spink, Z. Chen, J. Steele, D. Trapp, J. Irwin, M. Feser, E. Snyder, K. Brister, C. Jacobsen, G. Woloschak, and S. Vogt, "The Bionanoprobe: hard X-ray fluorescence nanoprobe with cryogenic capabilities," *Journal of Synchrotron Radiation*, vol. 21, pp. 66–75, Jan. 2014.

[174] J. Deng, Y. S. G. Nashed, S. Chen, N. W. Phillips, T. Peterka, R. Ross, S. Vogt, C. Jacobsen, and D. J. Vine, "Continuous motion scan ptychography: characterization for increased speed in coherent x-ray imaging," *Optics Express*, vol. 23, p. 5438, Mar. 2015.

[175] Y. S. G. Nashed, D. J. Vine, T. Peterka, J. Deng, R. Ross, and C. Jacobsen, "Parallel ptychographic reconstruction," *Optics Express*, vol. 22, p. 32082, Dec. 2014.

[176] D. Hull and D. J. Bacon, *Introduction to dislocations*. Amsterdam: Elsevier/Butterworth-Heinemann, 5. ed ed., 2011. OCLC: 704891549.

[177] A. Kelly and K. M. Knowles, *Crystallography and Crystal Defects: Kelly/Crystallography and Crystal Defects*. Chichester, UK: John Wiley & Sons, Ltd, Jan. 2012.

[178] M. K. Miller, T. F. Kelly, K. Rajan, and S. P. Ringer, "The future of atom probe tomography," *Materials Today*, vol. 15, pp. 158–165, Apr. 2012.

[179] P. A. Midgley and R. E. Dunin-Borkowski, "Electron tomography and holography in materials science," *Nature Materials*, vol. 8, pp. 271–280, Apr. 2009.

[180] D. A. Muller, "Structure and bonding at the atomic scale by scanning transmission electron microscopy," *Nature Materials*, vol. 8, pp. 263–270, Apr. 2009.

[181] O. L. Krivanek, M. F. Chisholm, V. Nicolosi, T. J. Pennycook, G. J. Corbin, N. Dellby, M. F. Murfitt, C. S. Own, Z. S. Szilagyi, M. P. Oxley, S. T. Pantelides, and S. J. Pennycook, "Atom-by-atom structural and chemical analysis by annular dark-field electron microscopy," *Nature*, vol. 464, pp. 571–574, Mar. 2010.

[182] S. J. Pennycook and P. D. Nellist, eds., *Scanning transmission electron microscopy: imaging and analysis*. New York, NY: Springer, 2011. OCLC: 722808665.

[183] S. Van Aert, K. J. Batenburg, M. D. Rossell, R. Erni, and G. Van Tendeloo, "Three-dimensional atomic imaging of crystalline nanoparticles," *Nature*, vol. 470, pp. 374–377, Feb. 2011.

[184] S. Bals, M. Casavola, M. A. van Huis, S. Van Aert, K. J. Batenburg, G. Van Tendeloo, and D. Vanmaekelbergh, "Three-Dimensional Atomic Imaging of Colloidal CoreShell Nanocrystals," *Nano Letters*, vol. 11, pp. 3420–3424, Aug. 2011.

[185] B. Goris, A. De Backer, S. Van Aert, S. Gmez-Graa, L. M. Liz-Marzn, G. Van Tendeloo, and S. Bals, "Three-Dimensional Elemental Mapping at the Atomic Scale in Bimetallic Nanocrystals," *Nano Letters*, vol. 13, pp. 4236–4241, Sept. 2013.

[186] H. Yang, J. G. Lozano, T. J. Pennycook, L. Jones, P. B. Hirsch, and P. D. Nellist, "Imaging screw dislocations at atomic resolution by aberration-corrected electron optical sectioning," *Nature Communications*, vol. 6, Dec. 2015.

[187] J. Park, H. Elmlund, P. Ercius, J. M. Yuk, D. T. Limmer, Q. Chen, K. Kim, S. H. Han, D. A. Weitz, A. Zettl, and A. P. Alivisatos, "3d structure of individual nanocrystals in solution by electron microscopy," *Science*, vol. 349, pp. 290–295, July 2015.

[188] R. G. Parr and W. Yang, *Density-functional theory of atoms and molecules*. No. 16 in International series of monographs on chemistry, New York, NY: Oxford Univ. Press [u.a.], 1. iss. as ... paperback ed., 1994. OCLC: 832732716.

[189] R. Jones, "Density functional theory: Its origins, rise to prominence, and future," *Reviews of Modern Physics*, vol. 87, pp. 897–923, Aug. 2015.

[190] B. D. Cullity and C. D. Graham, *Introduction to magnetic materials*. Hoboken, N.J: IEEE/Wiley, 2nd ed ed., 2009.

[191] G. Ju, Y. Peng, E. K. C. Chang, Y. Ding, A. Q. Wu, X. Zhu, Y. Kubota, T. J. Klemmer, H. Amini, L. Gao, Z. Fan, T. Rausch, P. Subedi, M. Ma, S. Kalarickal, C. J. Rea, D. V. Dimitrov, P.-W. Huang, K. Wang, X. Chen, C. Peng, W. Chen, J. W. Dykes, M. A. Seigler, E. C. Gage, R. Chantrell, and J.-U. Thiele, "High Density Heat-Assisted Magnetic Recording Media and Advanced CharacterizationProgress and Challenges," *IEEE Transactions on Magnetics*, vol. 51, pp. 1–9, Nov. 2015.

[192] T. R. Albrecht, H. Arora, V. Ayanoor-Vitikkate, J.-M. Beaujour, D. Bedau, D. Berman, A. L. Bogdanov, Y.-A. Chapuis, J. Cushen, E. E. Dobisz, G. Doerk, He Gao, M. Grobis, B. Gurney, W. Hanson, O. Hellwig, T. Hirano, P.-O. Jubert, D. Kercher, J. Lille, Zuwei Liu, C. M. Mate, Y. Obukhov, K. C. Patel, K. Rubin, R. Ruiz, M. Schabes, Lei Wan, D. Weller, Tsai-Wei Wu, and En Yang, "Bit-Patterned Magnetic Recording: Theory, Media Fabrication, and Recording Performance," *IEEE Transactions on Magnetics*, vol. 51, pp. 1–42, May 2015.

[193] C. Antoniak, M. E. Gruner, M. Spasova, A. V. Trunova, F. M. Rmer, A. Warland, B. Krumme, K. Fauth, S. Sun, P. Entel, M. Farle, and H. Wende, "A guideline for atomistic design and understanding of ultrahard nanomagnets," *Nature Communications*, vol. 2, p. 528, Nov. 2011.

[194] S. Sun, "Monodisperse FePt Nanoparticles and Ferromagnetic FePt Nanocrystal Superlattices," *Science*, vol. 287, pp. 1989–1992, Mar. 2000.

[195] M. E. Gruner, G. Rollmann, P. Entel, and M. Farle, "Multiply Twinned Morphologies of FePt and CoPt Nanoparticles," *Physical Review Letters*, vol. 100, Feb. 2008.

[196] M. E. Gruner and P. Entel, "Competition between ordering, twinning, and segregation in binary magnetic 3d-5d nanoparticles: A supercomputing perspective," *International Journal of Quantum Chemistry*, vol. 112, pp. 277–288, Jan. 2012.

[197] C. Antoniak, J. Lindner, M. Spasova, D. Sudfeld, M. Acet, M. Farle, K. Fauth, U. Wiedwald, H.-G. Boyen, P. Ziemann, F. Wilhelm, A. Rogalev, and S. Sun, "Enhanced Orbital Magnetism in Fe 50 Pt 50 Nanoparticles," *Physical Review Letters*, vol. 97, Sept. 2006.

[198] O. Dmitrieva, M. Spasova, C. Antoniak, M. Acet, G. Dumpich, J. Kstner, M. Farle, K. Fauth, U. Wiedwald, H.-G. Boyen, and P. Ziemann, "Magnetic

moment of Fe in oxide-free FePt nanoparticles," *Physical Review B*, vol. 76, Aug. 2007.

[199] C. Xu, Z. Yuan, N. Kohler, J. Kim, M. A. Chung, and S. Sun, "FePt Nanoparticles as an Fe Reservoir for Controlled Fe Release and Tumor Inhibition," *Journal of the American Chemical Society*, vol. 131, pp. 15346–15351, Oct. 2009.

[200] K. G. Larkin, M. A. Oldfield, and H. Klemm, "Fast Fourier method for the accurate rotation of sampled images," *Optics Communications*, vol. 139, pp. 99–106, June 1997.

[201] M. Makitalo and A. Foi, "A Closed-Form Approximation of the Exact Unbiased Inverse of the Anscombe Variance-Stabilizing Transformation," *IEEE Transactions on Image Processing*, vol. 20, pp. 2697–2698, Sept. 2011.

[202] A. Pryor, C. Ophus, and J. Miao, "A streaming multi-GPU implementation of image simulation algorithms for scanning transmission electron microscopy," *Advanced Structural and Chemical Imaging*, vol. 3, Dec. 2017.

[203] A. V. Crewe, "Scanning transmission electron microscopy," *Journal of microscopy*, vol. 100, no. 3, pp. 247–259, 1974.

[204] P. D. Nellist, "Scanning transmission electron microscopy," in *Science of microscopy*, pp. 65–132, Springer, 2007.

[205] P. Batson, N. Dellby, and O. Krivanek, "Sub-ångstrom resolution using aberration corrected electron optics," *Nature*, vol. 418, no. 6898, pp. 617–620, 2002.

[206] D. A. Muller, "Structure and bonding at the atomic scale by scanning transmission electron microscopy," *Nature materials*, vol. 8, no. 4, pp. 263–270, 2009.

[207] S. J. Pennycook, "The impact of stem aberration correction on materials science," *Ultramicroscopy*, 2017.

[208] P. M. Pelz, W. X. Qiu, R. Bücker, G. Kassier, and R. Miller, "Low-dose cryo electron ptychography via non-convex bayesian optimization," *arXiv preprint arXiv:1702.05732*, 2017.

[209] W. Van den Broek and C. T. Koch, "Method for retrieval of the three-dimensional object potential by inversion of dynamical electron scattering," *Physical review letters*, vol. 109, no. 24, p. 245502, 2012.

[210] A. B. Yankovich, B. Berkels, W. Dahmen, P. Binev, S. I. Sanchez, S. A. Bradley, A. Li, I. Szlufarska, and P. M. Voyles, "Picometre-precision analysis

of scanning transmission electron microscopy images of platinum nanocatalysts," *Nature Communications*, vol. 5, 2014.

[211] N. Mevenkamp, P. Binev, W. Dahmen, P. M. Voyles, A. B. Yankovich, and B. Berkels, "Poisson noise removal from high-resolution stem images based on periodic block matching," *Advanced Structural and Chemical Imaging*, vol. 1, no. 1, p. 3, 2015.

[212] C. Ophus, J. Ciston, J. Pierce, T. R. Harvey, J. Chess, B. J. McMorran, C. Czarnik, H. H. Rose, and P. Ercius, "Efficient linear phase contrast in scanning transmission electron microscopy with matched illumination and detector interferometry," *Nature communications*, vol. 7, 2016.

[213] K. H. van den Bos, A. De Backer, G. T. Martinez, N. Winckelmans, S. Bals, P. D. Nellist, and S. Van Aert, "Unscrambling mixed elements using high angle annular dark field scanning transmission electron microscopy," *Physical Review Letters*, vol. 116, no. 24, p. 246101, 2016.

[214] J. M. Cowley and A. F. Moodie, "The scattering of electrons by atoms and crystals. i. a new theoretical approach," *Acta Crystallographica*, vol. 10, no. 10, pp. 609–619, 1957.

[215] E. J. Kirkland, R. F. Loane, and J. Silcox, "Simulation of annular dark field stem images using a modified multislice method," *Ultramicroscopy*, vol. 23, no. 1, pp. 77–96, 1987.

[216] K. Ishizuka and N. Uyeda, "A new theoretical and practical approach to the multislice method," *Acta Crystallographica Section A: Crystal Physics, Diffraction, Theoretical and General Crystallography*, vol. 33, no. 5, pp. 740–749, 1977.

[217] K. Ishizuka, "A practical approach for stem image simulation based on the fft multislice method," *Ultramicroscopy*, vol. 90, no. 2, pp. 71–83, 2002.

[218] P. Stadelmann, "Ems-a software package for electron diffraction analysis and hrem image simulation in materials science," *Ultramicroscopy*, vol. 21, no. 2, pp. 131–145, 1987.

[219] P. Stadelmann, "Image analysis and simulation software in transmission electron microscopy," *Microscopy and Microanalysis*, vol. 9, no. S03, pp. 60–61, 2003.

[220] R. Kilaas, "Mactempas: a program for simulating high resolution tem images and diffraction patterns."

[221] C. T. Koch, *Determination of core structure periodicity and point defect density along dislocations*. 2002.

[222] M. De Graef, *Introduction to conventional transmission electron microscopy*. Cambridge University Press, 2003.

[223] J. Zuo and J. Mabon, "Web-based electron microscopy application software: Web-emaps," *Microscopy and Microanalysis*, vol. 10, no. S02, p. 1000, 2004.

[224] E. Carlino, V. Grillo, and P. Palazzari, "Accurate and fast multislice simulations of haadf image contrast by parallel computing," *Microscopy of Semiconducting Materials 2007*, pp. 177–180, 2008.

[225] V. Grillo and E. Rotunno, "STEM_CELL: A software tool for electron microscopy: Part Isimulations," *Ultramicroscopy*, vol. 125, pp. 97–111, 2013.

[226] A. Rosenauer and M. Schowalter, "Stemsima new software tool for simulation of stem haadf z-contrast imaging," *Microscopy of Semiconducting Materials 2007*, pp. 170–172, 2008.

[227] S. K. Walton, K. Zeissler, W. R. Branford, and S. Felton, "Malts: A tool to simulate lorentz transmission electron microscopy from micromagnetic simulations," *IEEE Transactions on Magnetics*, vol. 49, no. 8, pp. 4795–4800, 2013.

[228] M. Bar-Sadan, J. Barthel, H. Shtrikman, and L. Houben, "Direct imaging of single au atoms within gaas nanowires," *Nano letters*, vol. 12, no. 5, pp. 2352–2356, 2012.

[229] W. Van den Broek, X. Jiang, and C. Koch, "FDES, a GPU-based multislice algorithm with increased efficiency of the computation of the projected potential," *Ultramicroscopy*, vol. 158, pp. 89–97, 2015.

[230] E. Cosgriff, A. DAlfonso, L. Allen, S. Findlay, A. Kirkland, and P. Nellist, "Three-dimensional imaging in double aberration-corrected scanning confocal electron microscopy, part i:: Elastic scattering," *Ultramicroscopy*, vol. 108, no. 12, pp. 1558–1566, 2008.

[231] B. Forbes, A. Martin, S. Findlay, A. Dalfonso, and L. Allen, "Quantum mechanical model for phonon excitation in electron diffraction and imaging using a born-oppenheimer approximation," *Physical Review B*, vol. 82, no. 10, p. 104103, 2010.

[232] J. O. Oelerich, L. Duschek, J. Belz, A. Beyer, S. D. Baranovskii, and K. Volz, "Stemsalabim: A high-performance computing cluster friendly code for scanning transmission electron microscopy image simulations of thin specimens," *Ultramicroscopy*, vol. 177, pp. 91–96, 2017.

[233] C. Ophus, "A fast image simulation algorithm for scanning transmission electron microscopy," *Advanced Structural and Chemical Imaging*, vol. 3, no. 1, p. 13, 2017.

[234] Y. Yao, B. Ge, X. Shen, Y. Wang, and R. Yu, "Stem image simulation with hybrid cpu/gpu programming," *Ultramicroscopy*, vol. 166, pp. 1–8, 2016.

[235] M. Frigo and S. G. Johnson, "The design and implementation of FFTW3," *Proceedings of the IEEE*, vol. 93, no. 2, pp. 216–231, 2005.

[236] NVIDIA, "cufft."

[237] V. Volkov and J. W. Demmel, "Benchmarking gpus to tune dense linear algebra," in *High Performance Computing, Networking, Storage and Analysis, 2008. SC 2008. International Conference for*, pp. 1–11, IEEE, 2008.

[238] H. Yang, R. Rutte, L. Jones, M. Simson, R. Sagawa, H. Ryll, M. Huth, T. Pennycook, M. Green, H. Soltau, *et al.*, "Simultaneous atomic-resolution electron ptychography and z-contrast imaging of light and heavy elements in complex nanostructures," *Nature Communications*, vol. 7, p. 12532, 2016.

[239] K. Martin and B. Hoffman, *Mastering CMake: a cross-platform build system*. Kitware, 2010.

[240] NVIDIA, "Cuda c programming guide."

[241] M. Harris, ""optimizing parallel reduction in cuda"." Presentation included in the CUDA Toolkit released by NVIDIA, 2007.

[242] Intel, "e5-4669v4."

[243] N. Sakran, M. Yuffe, M. Mehalel, J. Doweck, E. Knoll, and A. Kovacs, "The implementation of the 65nm dual-core 64b merom processor," in *Solid-State Circuits Conference, 2007. ISSCC 2007. Digest of Technical Papers. IEEE International*, pp. 106–590, IEEE, 2007.

[244] J. Jeffers and J. Reinders, *Intel Xeon Phi Coprocessor High Performance Programming*. San Francisco, CA, USA: Morgan Kaufmann Publishers Inc., 1st ed., 2013.

[245] G. Stone, C. Ophus, T. Birol, J. Ciston, C.-H. Lee, K. Wang, C. J. Fennie, D. G. Schlom, N. Alem, and V. Gopalan, "Atomic scale imaging of competing polar states in a ruddlesden-popper layered oxide," *Nature communications*, vol. 7, 2016.

[246] D. A. Muller, N. Nakagawa, A. Ohtomo, J. L. Grazul, and H. Y. Hwang, "Atomic-scale imaging of nanoengineered oxygen vacancy profiles in srtio3," *Nature*, vol. 430, no. 7000, pp. 657–661, 2004.

[247] J. M. LeBeau, S. D. Findlay, L. J. Allen, and S. Stemmer, "Quantitative atomic resolution scanning transmission electron microscopy," *Physical Review Letters*, vol. 100, no. 20, p. 206101, 2008.

[248] S. Findlay, N. Shibata, H. Sawada, E. Okunishi, Y. Kondo, and Y. Ikuhara, "Dynamics of annular bright field imaging in scanning transmission electron microscopy," *Ultramicroscopy*, vol. 110, no. 7, pp. 903–923, 2010.

[249] L. F. Kourkoutis, M. Parker, V. Vaithyanathan, D. Schlom, and D. Muller, "Direct measurement of electron channeling in a crystal using scanning transmission electron microscopy," *Physical Review B*, vol. 84, no. 7, p. 075485, 2011.

[250] J. Cui, Y. Yao, Y. Wang, X. Shen, and R. Yu, "The origin of atomic displacements in haadf images of the tilted specimen," *arXiv preprint arXiv:1704.07524*, 2017.

[251] B. O. Dabbousi, J. Rodriguez-Viejo, F. V. Mikulec, J. R. Heine, H. Mattoussi, R. Ober, K. F. Jensen, and M. G. Bawendi, "(CdSe)ZnS CoreShell Quantum Dots: Synthesis and Characterization of a Size Series of Highly Luminescent Nanocrystallites," *The Journal of Physical Chemistry B*, vol. 101, pp. 9463–9475, Nov. 1997.

[252] S. Alayoglu, A. U. Nilekar, M. Mavrikakis, and B. Eichhorn, "RuPt coreshell nanoparticles for preferential oxidation of carbon monoxide in hydrogen," *Nature Materials*, vol. 7, pp. 333–338, Apr. 2008.

[253] F. Tao, M. E. Grass, Y. Zhang, D. R. Butcher, J. R. Renzas, Z. Liu, J. Y. Chung, B. S. Mun, M. Salmeron, and G. A. Somorjai, "Reaction-Driven Restructuring of Rh-Pd and Pt-Pd Core-Shell Nanoparticles," *Science*, vol. 322, pp. 932–934, Nov. 2008.

[254] R. Ghosh Chaudhuri and S. Paria, "Core/Shell Nanoparticles: Classes, Properties, Synthesis Mechanisms, Characterization, and Applications," *Chemical Reviews*, vol. 112, pp. 2373–2433, Apr. 2012.

[255] I. Robinson and R. Harder, "Coherent X-ray diffraction imaging of strain at the nanoscale," *Nature Materials*, vol. 8, pp. 291–298, Apr. 2009.

[256] J. Miao, T. Ishikawa, B. Johnson, E. H. Anderson, B. Lai, and K. O. Hodgson, "High Resolution 3D X-Ray Diffraction Microscopy," *Physical Review Letters*, vol. 89, Aug. 2002.

[257] M. A. Pfeifer, G. J. Williams, I. A. Vartanyants, R. Harder, and I. K. Robinson, "Three-dimensional mapping of a deformation field inside a nanocrystal," *Nature*, vol. 442, pp. 63–66, July 2006.

[258] A. Greenbaum, W. Luo, T.-W. Su, Z. Grcs, L. Xue, S. O. Isikman, A. F. Coskun, O. Mudanyali, and A. Ozcan, "Imaging without lenses: achievements and remaining challenges of wide-field on-chip microscopy," *Nature Methods*, vol. 9, pp. 889–895, Aug. 2012.

[259] A. Szameit, Y. Shechtman, E. Osherovich, E. Bullkich, P. Sidorenko, H. Dana, S. Steiner, E. B. Kley, S. Gazit, T. Cohen-Hyams, S. Shoham, M. Zibulevsky, I. Yavneh, Y. C. Eldar, O. Cohen, and M. Segev, "Sparsity-based single-shot subwavelength coherent diffractive imaging," *Nature Materials*, vol. 11, pp. 455–459, Apr. 2012.

[260] J. N. Clark, L. Beitra, G. Xiong, A. Higginbotham, D. M. Fritz, H. T. Lemke, D. Zhu, M. Chollet, G. J. Williams, M. Messerschmidt, B. Abbey, R. J. Harder, A. M. Korsunsky, J. S. Wark, and I. K. Robinson, "Ultrafast Three-Dimensional Imaging of Lattice Dynamics in Individual Gold Nanocrystals," *Science*, vol. 341, pp. 56–59, July 2013.

[261] D. F. Gardner, M. Tanksalvala, E. R. Shanblatt, X. Zhang, B. R. Galloway, C. L. Porter, R. Karl Jr, C. Bevis, D. E. Adams, H. C. Kapteyn, M. M. Murnane, and G. F. Mancini, "Subwavelength coherent imaging of periodic samples using a 13.5 nm tabletop high-harmonic light source," *Nature Photonics*, vol. 11, pp. 259–263, Mar. 2017.

[262] P. Emma, R. Akre, J. Arthur, R. Bionta, C. Bostedt, J. Bozek, A. Brachmann, P. Bucksbaum, R. Coffee, F.-J. Decker, Y. Ding, D. Dowell, S. Edstrom, A. Fisher, J. Frisch, S. Gilevich, J. Hastings, G. Hays, P. Hering, Z. Huang, R. Iverson, H. Loos, M. Messerschmidt, A. Miahnahri, S. Moeller, H.-D. Nuhn, G. Pile, D. Ratner, J. Rzepiela, D. Schultz, T. Smith, P. Stefan, H. Tompkins, J. Turner, J. Welch, W. White, J. Wu, G. Yocky, and J. Galayda, "First lasing and operation of an ngstrom-wavelength free-electron laser," *Nature Photonics*, vol. 4, pp. 641–647, Sept. 2010.

[263] T. Ishikawa, H. Aoyagi, T. Asaka, Y. Asano, N. Azumi, T. Bizen, H. Ego, K. Fukami, T. Fukui, Y. Furukawa, S. Goto, H. Hanaki, T. Hara, T. Hasegawa, T. Hatsui, A. Higashiya, T. Hirono, N. Hosoda, M. Ishii, T. Inagaki, Y. Inubushi, T. Itoga, Y. Joti, M. Kago, T. Kameshima, H. Kimura, Y. Kirihara, A. Kiyomichi, T. Kobayashi, C. Kondo, T. Kudo, H. Maesaka, X. M. Marchal, T. Masuda, S. Matsubara, T. Matsumoto, T. Matsushita, S. Matsui, M. Nagasono, N. Nariyama, H. Ohashi, T. Ohata, T. Ohshima, S. Ono, Y. Otake, C. Saji, T. Sakurai, T. Sato, K. Sawada, T. Seike, K. Shirasawa, T. Sugimoto, S. Suzuki, S. Takahashi, H. Takebe, K. Takeshita, K. Tamasaku, H. Tanaka, R. Tanaka, T. Tanaka, T. Togashi, K. Togawa, A. Tokuhisa, H. Tomizawa, K. Tono, S. Wu, M. Yabashi, M. Yamaga, A. Yamashita, K. Yanagida, C. Zhang, T. Shintake, H. Kitamura, and N. Kumagai, "A compact X-ray free-electron laser emitting in the sub-ngstrm region," *Nature Photonics*, vol. 6, pp. 540–544, June 2012.

[264] H. N. Chapman, A. Barty, M. J. Bogan, S. Boutet, M. Frank, S. P. Hau-Riege, S. Marchesini, B. W. Woods, S. Bajt, W. H. Benner, R. A. London, E. Plnjes, M. Kuhlmann, R. Treusch, S. Dsterer, T. Tschentscher, J. R.

Schneider, E. Spiller, T. Mller, C. Bostedt, M. Hoener, D. A. Shapiro, K. O. Hodgson, D. van der Spoel, F. Burmeister, M. Bergh, C. Caleman, G. Huldt, M. M. Seibert, F. R. N. C. Maia, R. W. Lee, A. Szke, N. Timneanu, and J. Hajdu, "Femtosecond diffractive imaging with a soft-X-ray free-electron laser," *Nature Physics*, vol. 2, pp. 839–843, Dec. 2006.

[265] C.-C. Chen, H. Jiang, L. Rong, S. Salha, R. Xu, T. G. Mason, and J. Miao, "Three-dimensional imaging of a phase object from a single sample orientation using an optical laser," *Physical Review B*, vol. 84, Dec. 2011.

[266] D. Van Dyck and F.-R. Chen, "Big Bang tomography as a new route to atomic-resolution electron tomography," *Nature*, vol. 486, pp. 243–246, June 2012.

[267] M. Mutzafi, Y. Shechtman, Y. C. Eldar, O. Cohen, and M. Segev, "Sparsity-based Ankylography for Recovering 3D molecular structures from single-shot 2d scattered light intensity," *Nature Communications*, vol. 6, p. 7950, Aug. 2015.

[268] R. Xu, H. Jiang, C. Song, J. A. Rodriguez, Z. Huang, C.-C. Chen, D. Nam, J. Park, M. Gallagher-Jones, S. Kim, S. Kim, A. Suzuki, Y. Takayama, T. Oroguchi, Y. Takahashi, J. Fan, Y. Zou, T. Hatsui, Y. Inubushi, T. Kameshima, K. Yonekura, K. Tono, T. Togashi, T. Sato, M. Yamamoto, M. Nakasako, M. Yabashi, T. Ishikawa, and J. Miao, "Single-shot three-dimensional structure determination of nanocrystals with femtosecond X-ray free-electron laser pulses," *Nature Communications*, vol. 5, June 2014.

[269] S. O. Hruszkewycz, M. Allain, M. V. Holt, C. E. Murray, J. R. Holt, P. H. Fuoss, and V. Chamard, "High-resolution three-dimensional structural microscopy by single-angle Bragg ptychography," *Nature Materials*, vol. 16, pp. 244–251, Nov. 2016.

[270] A. Pryor Jr, A. Rana, R. Xu, J. A. Rodriguez, Y. Yang, M. Gallagher-Jones, H. Jiang, J. Park, S. Kim, S. Kim, D. Nam, Y. Yue, J. Fan, Z. Sun, B. Zhang, D. Gardner, C. Dias, Y. Joti, T. Hatsui, T. Kameshima, Y. Inubushi, K. Tono, J. Lee, M. Yabashi, C. Song, T. Ishikawa, H. Kapteyn, M. Murnane, and J. Miao, "Single-shot 3D diffractive imaging of core-shell nanoparticles with elemental specificity," *arXiv preprint arXiv:1702.06600*, 2017.

[271] Y. Yu, Q. Zhang, B. Liu, and J. Y. Lee, "Synthesis of Nanocrystals with Variable High-Index Pd Facets through the Controlled Heteroepitaxial Growth of Trisoctahedral Au Templates," *Journal of the American Chemical Society*, vol. 132, pp. 18258–18265, Dec. 2010.

[272] T. Kameshima, S. Ono, T. Kudo, K. Ozaki, Y. Kirihara, K. Kobayashi, Y. Inubushi, M. Yabashi, T. Horigome, A. Holland, K. Holland, D. Burt, H. Murao, and T. Hatsui, "Development of an X-ray pixel detector with multi-port charge-coupled device for X-ray free-electron laser experiments," *Review of Scientific Instruments*, vol. 85, p. 033110, Mar. 2014.

[273] C. Song, D. Ramunno-Johnson, Y. Nishino, Y. Kohmura, T. Ishikawa, C.-C. Chen, T.-K. Lee, and J. Miao, "Phase retrieval from exactly oversampled diffraction intensity through deconvolution," *Physical Review B*, vol. 75, Jan. 2007.

[274] B. Henke, E. Gullikson, and J. Davis, "X-Ray Interactions: Photoabsorption, Scattering, Transmission, and Reflection at E = 50-30,000 eV, Z = 1-92," *Atomic Data and Nuclear Data Tables*, vol. 54, pp. 181–342, July 1993.